The Dissertation Committee for Ho Hyun Sun
Certifies that this is the approved version of the following dissertation

Stable High Energy Density Batteries Based on Microstructure Modified Ni-rich Lithium Intercalating Cathodes and a Surface-stabilized Metallic Lithium Anode

APPROVED BY
SUPERVISING COMMITTEE:

Charles Buddie Mullins, Supervisor

Adam Heller

Benjamin K. Ketiz

Gyeong S. Hwang

Graeme Andrew Henkelman

Stable High Energy Density Batteries Based on Microstructure Modified Ni-rich Lithium Intercalating Cathodes and a Surface-stabilized Metallic Lithium Anode

by

Ho Hyun Sun

Dissertation

Presented to the Faculty of the Graduate School of

The University of Texas at Austin

in Partial Fulfillment

of the Requirements

for the Degree of

Doctor of Philosophy

The University of Texas at Austin

August 2020

Dedication

To my father and mother who held me through the hard times.

Acknowledgements

I would like to first and foremost express my deep appreciation and gratitude to my advisors, Professor C. Buddie Mullins and Professor Adam Heller, for their guidance, support, and encouragement all the way from when I was applying to the Ph.D. program in Chemical Engineering through to the completion of my degree. I would also like to thank all my committee members, Professors Bejamin K. Keitz, Gyeong S. Hwang, and Andrew G. Henkelman for their time and role in overseeing my doctoral studies, and the friendly guidance and thought- provoking suggestions. Additionally, I would like to acknowledge the precious support from all the members of Professor Mullins's group. Without their help and support, my research would not have been possible. I would like to thank the McKetta Department of Chemical Engineering, Cockrell School of Engineering, UT Graduate School, and the Welch Foundation for their support in funding my studies and research. Finally, I must thank my father (Yang-Kook Sun), mother (Eunhee Sun), and brother (Hojin Sun) for their continuous love and great support and innumerable sacrifices, without which I never could have completed my Ph.D. research.

Abstract

Stable High Energy Density Batteries Based on Microstructure Modified Ni-rich Lithium Intercalating Cathodes and a Surface-stabilized Metallic Lithium Anode

Ho Hyun Sun, Ph.D.

The University of Texas at Austin, 2020

Supervisor: Charles Buddie Mullins

While lithium-ion batteries (LIBs) are widely used in electric vehicles (EVs), many customers are disinclined to buy EVs because of their limited range. Significant increase in the range requires higher specific capacity electrodes for an equal or higher operating voltage battery, exemplified in this thesis by a metallic lithium anode and a high-Ni content layered oxide cathode. The instability of the lithium metal surface and the particle-fracturing in the high-Ni layered oxides have in the past prevented implementation of the two electrodes in commercially manufactured batteries. This dissertation explores these challenges through stabilization of the lithium metal anode by an inorganic compound rich SEI layer formed by tailoring the electrolyte and its reaction with lithium metal. The formed SEI layer is mechanically robust and highly Li^+ permeable. The Ni-rich layered oxide cathode is stabilized through nano- and micro-structured elongated rod-shaped grains, with the Ni concentration decreasing from their core to their surface. The Ni concentration gradient reduces detrimental reactions at the cathode surface and the rod-like grains maintain particle coherency for extended cycling. The tailored high-Ni cathodes

were also tested and found to be similarly efficient in batteries with metallic sodium anodes.

Table of Contents

List of Tables

List of Figures

Chapter 1: Introduction

1.1. Lithium-ion Battery Market and Energy Density

Lithium-ion batteries (LIBs) are widely used in portable electronic devices and in vehicular batteries. Their impact has been recognized by the award of the 2020 Nobel Prize in Chemistry to John Goodenough, Stanley Whittingham, and Akira Yoshino.[1–3] LIB sales have grown from ~ 20 GWh ($7.24 billion) in 2010 to ~ 120 GWh ($26.73 billion) in 2017.[4,5] A significant market segment is in electric vehicles (EVs), which is on track to grow globally from 4 million EVs on the road in 2018 to between 50 million and 225 million EVs by 2030.[4] The growth is, in part, a result of environmental policies aimed at reducing urban air pollution. Several countries have already banned the purchase of combustion engine vehicles and others are planning to do so. Consequently, most automobile manufacturers have expanded their EV research, development, and engineering effort and are annually introducing improved hybrid and EV models.

While the LIB market has grown rapidly, battery energy densities have increased by only 7 – 8 % per year to the present 200 Wh kg^{-1} and 600 Wh L^{-1}.[6] The limited LIB energy density translates to a restricted driving range for EVs. For example, of the 420 mile driving range of the plug-in hybrid electric vehicle (PHEV) Chevy Volt, only 53 miles are delivered electrically. The 53 electrical miles suffice only for urban commuters, but not for other customers. In 2012 the Department of Energy (DOE) estimated that to guarantee the success of future EVs, an electrical driving range of at least 300 miles is needed. That range translates to a battery pack with an energy density of about 500 Wh kg^{-1}.[7]

1.2. Lithium-ion Battery Operation

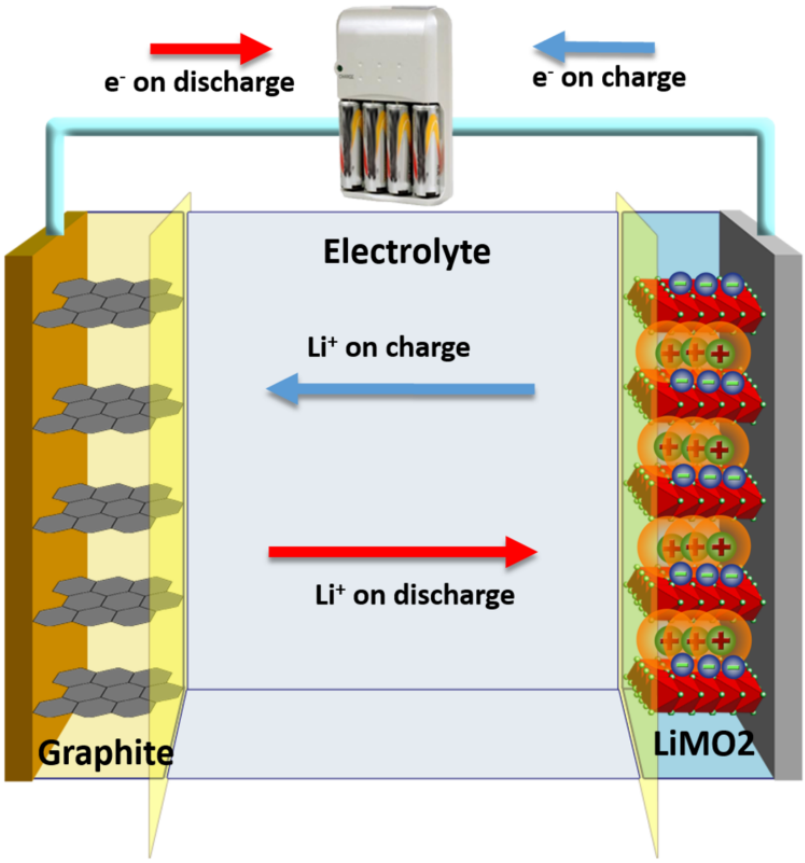

Figure 1.1. A schematic of a Li-ion battery components and its operation.

The lithium-ion battery is an array of electrically connected multiple lithium-ion cells in a protective casing. Each individual cell is comprised of a cathode, an anode, a separator, and electrolyte. It operates by shuttling Li^+ and electrons between the electrodes as shown in **Figure 1.1** in which the cathode displayed here is a layered lithium transition metal oxide ($LiMO_2$) and the anode is graphite. During charge, an external power supply drives the Li^+ from the cathode to the anode while charge neutrality is maintained by electrons flowing through the external circuit. The half-cell reaction of the cathode is represented by equation 1

$$LiMO_2 \leftrightarrow Li_{1-x}MO_x + xLi^+ + xe^- \quad (1)$$

During discharge, the potential difference between the electrodes drives the Li^+ in the reverse direction and the flow of charge neutrality maintaining electrons is also reversed. The half-cell reaction of the anode is:

$$C_n + xLi^+ + xe^- \leftrightarrow C_nLi_x \ (n = 6x) \quad (2)$$

The resulting overall cell-reaction within the cell is written as:

$$LiMO_2 + C_n \leftrightarrow Li_{1-x}MO_2 + C_nLi_x \ (n = 6x) \quad (3)$$

Other electrodes undergo different reactions, but the directions of the Li^+ and electron fluxes upon charging and discharging are the same.

1.3. Commercialized Lithium-ion Battery Cathodes

Decades of lithium-ion battery research, in which a massive number of cathodes has been considered, have yielded very few for actual use. Only the spinel lithium manganese oxide ($LiMn_2O_4$), the olivine lithium iron phosphate ($LiFePO_4$), and the layered lithium transition metal oxide ($LiMO_2$, M = Ni, Co, Mn, Al) cathodes have been commercialized. The $LiMn_2O_4$ cathode is of low cost, is environmentally friendly, and has an advantageously high potential of 4 V vs. Li/Li^+. It was first reported in 1983, was commercialized in 1996, and is used in the Nissan Leaf EV.[8–10] It has a spinel-type structure with the $Fd\bar{3}m$ space group, where Li occupies the tetrahedral 8a sites, Mn occupies the

octahedral 16d sites, and oxygen occupies the 32e sites in a cubic close-packed (CCP) array. The Mn maintains an octahedral coordination with the oxygen to form an edge sharing MnO_6 octahedra that hosts the Li^+ within. Li^+ diffuses in and out of the spinel structure through the vacant tetrahedral and octahedral interstitial sites. On the downside, $LiMn_2O_4$ has a low specific capacity of only 100 mAh g^{-1} and relatively poor cycling, due to dissolution from the surfaces of the grains leading to tetragonal $Li_2Mn_2O_4$ formation.[8–12] To address these drawbacks Ni has been incorporated into the lattice resulting in the $LiNi_{0.5}Mn_{.15}O_4$ cathode. It has a capacity of 130 mAh g^{-1} and an advantageously higher voltage of ~ 4.7 V. However, all organic electrolytic solutions are oxidized at this potential, and no high-voltage practical battery has resulted.

Olivine $LiFePO_4$ cathodes, developed by Padhi et al. in Goodenough's research group in 1996 have also been commercialized, with greater success than $LiMn_2O_4$. They are used in the DeWalt power tools and also power electric buses. $LiFePO_4$ has the olivine structure of the *Pnma* orthorhombic space group, where the Li and Fe occupy the octahedral sites whilst P occupies the tetrahedral sites in a hexagonal close-packed oxygen array.[11] Like the spinel $LiMn_2O_4$, the material has good thermal stability, is of low cost, has a higher capacity of 150 mAh g^{-1} and retains its capacity better upon cycling, especially at higher temperatures, due to the strong bonding between the phosphate and oxygen ions. $LiFePO_4$ is hampered in its employment by its poor electrical and ionic conductivities, its low discharge voltage and its low tap density.[10,11]

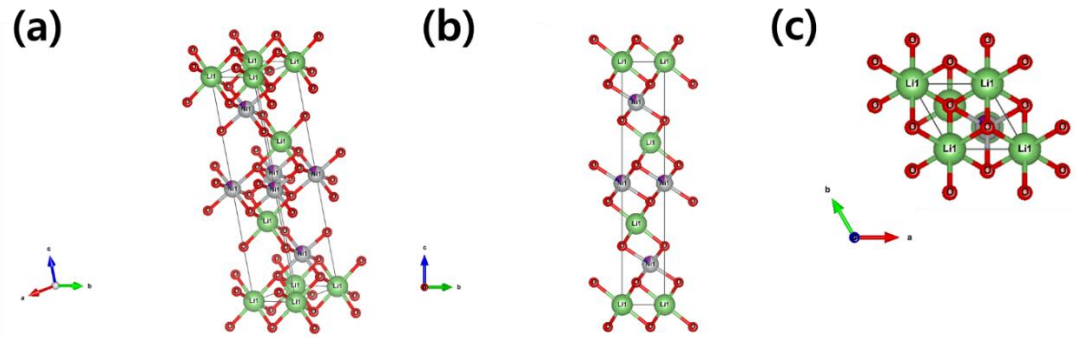

Figure 1.2. (a) Crystal structure of the O3-type layered $LiMO_2$ cathode. (b) Side view and (c) top-down view of the structure. The green, gray, and red balls correspond to Li, transition metal, and oxygen atoms, respectively.

Historically, but not in the context of EVs, the most successful cathode material has been $LiCoO_2$ (LCO), introduced by Goodenough in 1978 and commercialized by SONY in 1992. It is still used in many consumer electronic applications.[1,13] The $LiCoO_2$ has a hexagonal space group of $R\bar{3}m$ and a O3-type layered structure with an ABC stacking, where Li and Co occupy octahedral sites in alternating layers (3a and 3b sites) and oxygen occupies the 6c site in a face-centered cubic (FCC) array (Figure 1.2.). LCO is an attractive material because of its high electrical and ionic conductivity, good cycling performance, and fast charge-discharge rates. However, cobalt is expensive and environmentally harmful. Additionally, LCO has poor thermal stability, as it loses oxygen when heated, Its specific capacity is 150 mAh g^{-1}.[14,15]

$LiNiO_2$ (LNO) was developed as an alternative to LCO. Its specific capacity of 240 mAh g^{-1} is much higher and the cost of nickel is lower.[16] However, LNO has not been commercialized, because microcracking of its grains upon cycling leads to rapid loss of capacity.

Disadvantages of LCO and LNO cathodes have been addressed through the $Li[Ni_xCo_yMn_z]O_2$ (NCM) and $Li[Ni_xCo_yAl_z]O_2$ (NCA) cathodes that combine the advantageously high capacity of LNO and the relatively high conductivity of LCO. The present market share of the NCM and NCA cathodes is already 42 % and it is expected to increase to 78 % by 2025 in a rapidly expanding market, with the production of cathode materials projected to increase from 275,000 tons in 2017 to 870,000 tons by 2025.[17] Layered NCM and NCA cathodes have a competitive edge over others because of their higher energy density, lower cost, and, by now, their established reliability.[10] A major part of this dissertation focuses on the development of advanced NCM and NCA cathodes. A summary of the properties of the cathode materials is shown below in Table 1.1.

Table 1.1. Properties of commercialized cathode materials.

Structure	Material	Capacity (mAh/g)	Cycle life	High rate	Safety	Cost
Spinel	$LiMn_2O_4$	100	√	√+	√+	√+
	$LiNi_{0.5}Mn_{1.5}O_4$	150	√-	√	√	√
Olivine	$LiFePO_4$	150	√+	√	√+	√+
Layered	$LiCoO_2$	150	√+	√+	√	√−
	$LiNiO_2$	230	√-	√+	√−	√
	$Li[Ni_xCo_yMn_z]O_2$	160 – 200	√+	√+	√	√
	$Li[Ni_xCo_yAl_z]O_2$	180 – 200	√+	√+	√	√

1.4. Layered Ni-rich Cathode and Challenges

The theoretical specific capacities of LNO and LCO are similar, 274 and 275 mAh g^{-1} respectively, but their practical specific capacities of 247 mAh g^{-1} and 156 mAh g^{-1} at 0.1 C and 4.3 V differ [15,16] because of the higher starting discharge voltage and the lesser Li utilization of LCO compared to LNO. LNO is cheaper than LCO, with Ni currently trading at \$14 kg^{-1} and Co at \$31 kg^{-1}. Consequently, the layered $Li[Ni_xCo_yMn_z]O_2$ (NCM) and $Li[Ni_xCo_yAl_z]O_2$ (NCA) cathodes have already replaced the LCO cathode in the LIB EV market.[10,18] The persistent need for still higher energy density at a lower cost has pushed the atom percentage of Ni in the high-capacity NCM and NCA cathodes to above 60 atom %. The inclusion of more Ni is, however, at the cost of lesser cycling and thermal stabilities, as the weaker Ni-O bonds destabilize the lattices and increase their anisotropic volume change upon Li-extraction/insertion, microcracks now propagate through the particles. Additionally, at the more oxidizing redox potential of $Ni^{3+/4+}$, the surface of the particles reacts with and is reduced by the organic electrolytes. The loss of capacity upon cycling and the chemical instability are worsened upon increasing the atom percentage of Ni, especially above 80% Ni. These problems are now addressed in part by restricting the depth-of-discharge (DOD) to 60%, as is done in Panasonic's NCA cathodes, at the cost of limiting the voltage of the battery.

1.5. Commercialized Li-ion Anode

Graphite remains the dominant anode of lithium-ion batteries. Its space group is $P6_3/mmc$ and consists of layers of hexagonal cell graphene being stacked. The graphene

planes are bound by weak Van der Waals bonds and organized in an ABAB stacking sequence, separated by 3.35 Å, and allows Li^+ insertion between the planes.[19] Even though many other anode materials have been developed, graphite's stability upon cycling, its low-cost, and usage without pre-lithiation have prevented its displacement by other anode materials. Its low specific capacity of 372 mAh g^{-1}, however, limits the energy density of lithium batteries[20] to their respective gravimetric and volumetric energy densities of ~ 200 – 250 Wh kg^{-1} and ~ 600 Wh L^{-1}.[22]

1.6. Metallic Lithium Anode and Challenges

The metallic lithium anode, researched for 40 years, is still the most prominent alternative to graphite, because of its exceptionally high specific capacity of 3,860 mAh g^{-1}, its fast kinetics, and its potential of -3.004 V vs. SHE.[23] Just by replacing graphite with metallic lithium, the gravimetric and volumetric energy densities would be respectively increased to 400 – 500 Wh kg^{-1} and 800 Wh L^{-1}, meeting the DoE-targeted EV goal.[24] The increase results in not only a higher theoretical energy density for metallic lithium, but also eliminates the need for a copper foil current collector.

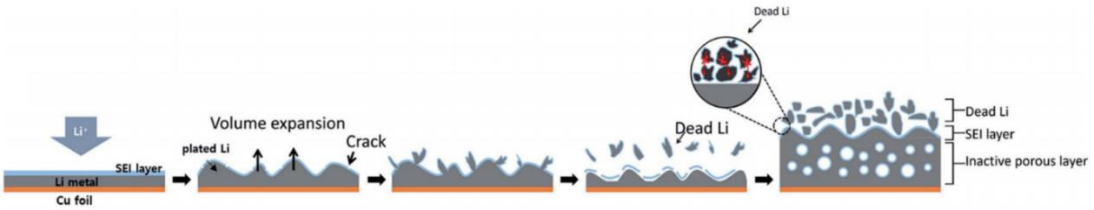

Figure 1.3. Schematic representation of the plating and stripping process of the conventional lithium metal anode.[21]

Realization of a viable lithium metal battery (LMB) is impeded by the cycling instability of metallic lithium and of its parasitic reactions with the electrolyte, resulting in uncontrollable Li dendrite growth, loss of electrolytic solution, and loss of active lithium.[20,25] After stripping and deposition cycles, Li-dendrites contact the cathode, shorting the electrodes.

1.7.1 Thesis Objective

The objective of this dissertation is to establish, through novel stabilization strategies, the basis for and demonstration of an engineering pre-prototype of a stably-cycling, high energy density lithium-ion battery comprised of a layered Ni-rich cathode and a metallic lithium anode (Figure 1.4).

1.7.2 Thesis Chapters

Chapter 2 outlines the strategy underlying the inorganic compound rich SEI layer suppressing dendrite growth and parasitic reactions of the metallic lithium anode.

Chapter 3 discusses strategies for enhancing the cyclability of layered Ni-rich cathodes with advantages over the reported failure-alleviating coatings and dopants.

Chapter 4 explores concentration gradient cathodes, overcoming both the chemical and structural instability of the Ni-rich cathodes, providing cycling stabilty and thermal stability.

Chapter 5 applies the best concentration gradient Ni-rich cathodes to metallic sodium anode batteries (SIBs).

Chapter 7 summarizes the works and provides an outlook for future works.

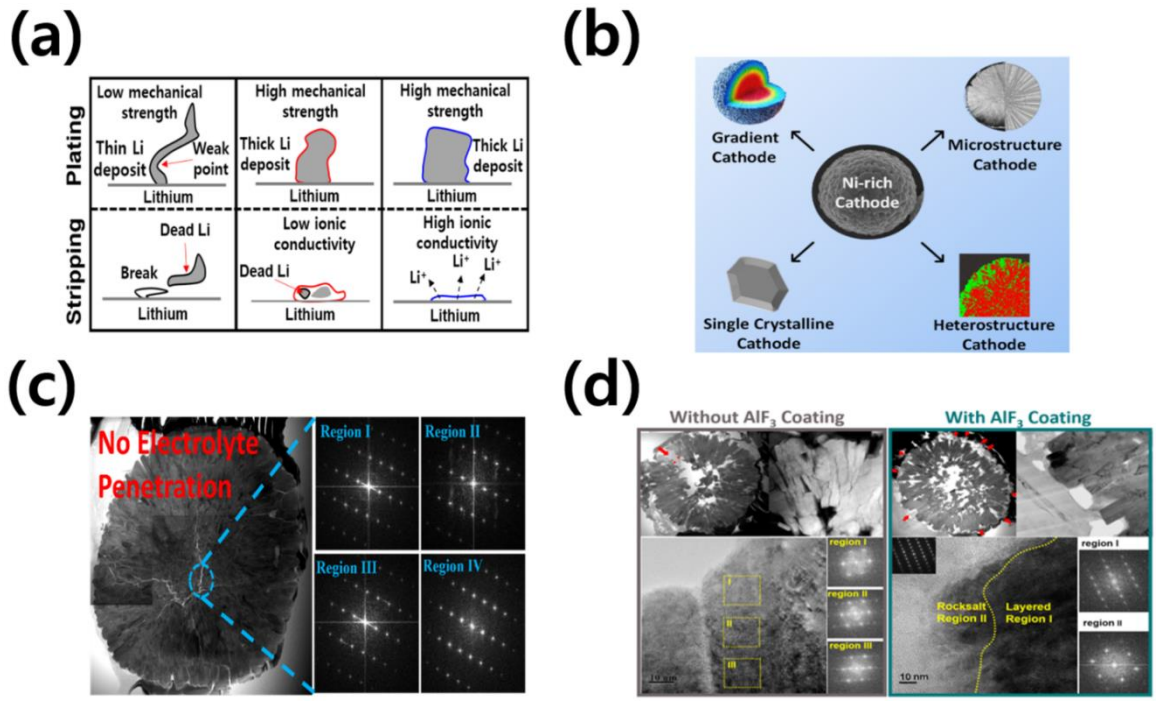

Figure 1.4. Schematics of topics discussed in this dissertation: (a) multicomponent inorganic-rich SEI layer,[26] (b) prospective strategies for stable Ni-rich layered oxide cathodes,[27] (c) nanorod concentration gradient cathode for Li-ion batteries,[28] and (d) nanorod concentration gradient cathode for Na-ion batteries.[29]

Chapter 2. In-situ Formation of a Multicomponent Inorganic-rich SEI Layer Provides a Fast Charging and High Specific Energy Li-metal Battery*

2.1. Introduction

After years of successful use of the 372 mAh g^{-1} specific capacity lithium-ion battery (LIB) graphite anode, the demand for higher energy-density batteries and the LIB capacity limitation imposed by intercalation chemistry[30–32] intensified the long-simmering interest in the 3,860 mAh g^{-1} specific capacity metallic lithium anode. Were it not for its Li^+-flux retarding SEI, the metallic Li could offer fast rate in a highly ionically conductive electrolyte and its low redox potential (-3.004 vs. standard hydrogen electrode) could increase the energy of cells.[33] Despite its promise, metallic Li does not cycle stably as the dendritic growth and the parasitic reaction of Li with the electrolyte causes loss of both electrolyte and of active lithium.[24,34,35]

To overcome these issues, the focus has shifted toward using a combination of electrolyte, salt, and additives to *in-situ* establish a stable solid-electrolyte interphase (SEI) layer as a protective and ionically conductive film on the lithium metal surface.[20,22,36] The SEI is vital to the stable cycling of Li metal and its efficacy depends heavily on its composition. In this regard, numerous electrolyte solutions and resulting SEI layers have

* **Sun, H.-H.**; Dolocan, A.; Weeks, J. A.; Rodriguez, R.; Heller, A.; Mullins, C. B. In-situ Formation of a Multicomponent Inorganic-rich SEI Layer Provides a Fast Charging and High Specific Energy Li-metal Battery. *J. Mater. CHem. A.* **2019**, *7*, 17782 – 17789. Ho-Hyun Sun carried out the experimental work. Prof. Mullins and Prof. Heller supervised the project. All participated in the discussion and preparation of the manuscript.

been reported. In particular, fluorinated electrolyte combinations have been studied to increase the LiF content in the SEI to enhance its protective capability since LiF-rich SEI passivates the lithium metal/electrolyte interface; it is electrochemically stable and has low electrical conductivity.[36–38] Other SEIs, heavy in Li_2CO_3, Li_2O, Li_2S, and Li_3N species, have also been reported to effectively enhance the mechanical stability and ionic conductivity of the SEI.[39–43] However, studies focusing on combinations of multiple SEI-beneficial compounds have been lacking.

Here, we report a SEI layer capable of maintaining the reversibility of lithium for long-term cycling by promoting the formation of SEI-beneficial species. In this endeavor, we employ a fluoroethylene carbonate (FEC)-based electrolyte to form a LiF-rich SEI layer coupled with lithium bis(trifluoromethanesulfonyl)imide (LiTFSI) and lithium difluoro(oxalate)borate (LiDFOB) dual-salts to introduce Li_3N/Li_2S and Li_2CO_3/O-B-O oligomeric and glass borates, respectively, to further reinforce the ionic conductivity and mechanical integrity of the SEI layer. As the extensive X-ray photoelectron spectroscopy (XPS) and time-of-flight secondary-ion mass spectrometry (TOF-SIMS) analysis delineate, the as-formed SEI layer was rich not only in LiF, but also in Li_3N, Li_2S, Li_2CO_3, and O-B-O oligomeric borates. The resulting SEI layer proved to be efficacious in stabilizing the lithium electrode by reducing the amount of electrically disconnected lithium. Reflecting its diversity in SEI-beneficial compounds, the 0.8 M LiTFSI + 0.2 M LiDFOB + 0.05 M $LiPF_6$ in EMC:FEC = 3:1 v/v LMB cell delivered a performance of 75 % capacity retention after 500 cycles (Li vs. $Li[Ni_{0.59}Co_{0.2}Mn_{0.2}Al_{0.01}]O_2$ cathode) with

Coulombic efficiencies exceeding 99.3 % at a current density of 1.8 mA cm^{-2} and discharge capacity of 1.77 mAh g^{-1}.

2.2. Experimental

2.2.1. Electrolytes and Cathode Preparation

Three solutions of 3:1 v/v EMC (99+%, TCI): FEC (99+%,TCI) (termed EF31) were made with (i) *10EF31P*, comprising 1 M LiTFSI (Sigma-Aldrich 99.95 %), 0.05 M $LiPF_6$ (BASF 99.8%); (ii) *82EF31P*, comprising 0.8 M LiTFSI; 0.2 M LiDFOB (Sigma-Aldrich) and 0.05M $LiPF_6$; and (iii) *64EF31P* comprising 0.6 M of LiTFSI; 0.4 M of LiDFOB and 0.05M $LiPF_6$. The lithium salts were vacuum dried, and the solvents were dried over alumina molecular sieve (Sigma-Aldrich). The Li metal foil (Hohsen Corp.) was used as received; the $Li[Ni_{0.59}Co_{0.2}Mn_{0.2}Al_{0.1}]O_2$ (NCM622-Al 1%) cathode material was a gift of the Sun lab at Hanyang University, Korea.

2.2.2. Electrochemical Characterization and Testing

Pairs of 5/8'' diameter Li electrodes were tested in 2032 coin-type cells. 100 μL of electrolyte was added to each cell and the cells were cycled galvanostatically at a current density of 0.9, 1.8, and 3.6 mA cm^{-2} with a deposition/stripping time of 1 hour each. The Li^+ transference number (t_+) was obtained with the symmetrical Li/Li cell by applying a DC voltage of 10 mV and measuring the resulting current. Average Coulombic efficiencies were determined in cells made with a Li metal foil electrode and a bare Cu electrode on which 4 mAh cm^{-2} of Li was deposited and stripped at 0.4 mA cm^{-2} until the voltage reached 1 V. Afterwards, 4 mAh cm^{-2} lithium was deposited/stripped at repeatedly for 15

cycles, then 0.5 mAh cm^{-2} was deposited in the terminal deposition half-cycle. The plated Li on Cu was then fully stripped at 0.4 mA cm^{-2} to 1 V.

Cells, termed LMBs, with 5/8'' diameter lithium foil lithium metal anodes and NCM622 cathodes were built with a Celgard 2400 separator and with the 82EF31P electrolytic solution. The NCM622 cathodes were prepared by mixing with Super-P carbon and polyvinylidene fluoride (PVdF) 90:5.5:4.5 ratio and casting onto an Al foil, resulting in a loading of ~ 10 mg cm^{-2}. The LMBs cells were cycled at 1 C rate (180 mA g^{-1}) between 2.7 V and 4.3 V vs. Li/Li^{+} at 30 °C. For the rate capability test, the LMB cells were cycled from 0.1 C rate to 5.0 C rate. For the electrochemical impedance spectroscopy (EIS), a Gamry Interface 1010E potentiostat was used and the Cu foil was treated with 1 M HCl solution to eliminate surface impurities. The measurements were at the 1 MHz to 1 Hz frequency range at ±10 mV amplitude after formation cycling then after 50 cycles. The Nyquist plots were created using ZView software and electrolyte conductivity was determined using the EIS measurement data and the following equations were used:

$$\delta \text{ (S cm}^{-1}) = \text{K/R}$$

$$K(cm^{-1}) = (l(Distance, cm))/(s(Surface\ area,\ cm2))$$

$$l = 100\mu m,\ s = 0.502cm2$$

where δ is the electrolyte conductivity (S cm^{-1}), K is a constant, R is the resistance (Ω), l is the distance (cm), and s is the surface area (cm^2).

2.2.3. Analytical Techniques

Scanning electron microscopy (SEM, FEI Quanta 650) images were obtained by depositing Li on a Cu foil using a Li/Cu cell configuration in a 2032 coin-type cell and optical deposition images were obtained using an optical cell previously reported before. The chemical composition of the SEI surface was measured utilizing a Kratos Axis Ultra X-ray photoelectron spectroscopy (XPS) to interrogate the Li deposited on the Cu substrate. Data was taken using a monochromatic Al-Kα X-ray source ($h\nu$ = 1486.5 eV) with a spot size of 300 x 700 μm^2. Binding energies were calibrated using the adventitious carbon peak in the C 1s spectra aligned to 284.8 eV. A TOF-SIMS 5 by ION-TOF GmbH, 2010 was used to measure the chemical composition as function of depth (that is, the depth profile) of the SEI and quantify the quantity of dead lithium after 10 cycles of deposition/stripping on the Cu foil. For depth profiling in negative polarity a Cs^+ beam (~ 40 nA at 0.5 keV or ~70 nA at 2 keV) was used to sputter a 300 x 300 μm^2 area and a Bi^+ analysis beam (~4 pA, 30 keV) was raster scanned over a 100 x 100 μm^2 area inside the regressing Cs-sputtered area. The negative polarity detection mode is used to identify most of the SEI composition. To detect the dead lithium, we performed depth profiling in positive polarity. In this mode, we keep all the sputtering conditions unchanged except switching the sputtering beam from Cs^+ to O_2^+ (~500 nA, 2 keV). Non-interlaced mode was used to acquire all depth profiles, that is sputtering, and surface analysis is done sequentially. For high resolution imaging at various depths we set the analysis ion gun in the fast imaging mode with 7 bursts (~200 nm lateral resolution, ~0.04 nA Bi^+ sample

current). Note that SEM, XPS, and TOF-SIMS samples were all kept under inert conditions using a vacuum transfer chamber.

2.3. Results and discussions

2.3.1. SEI layer surface XPS characterization

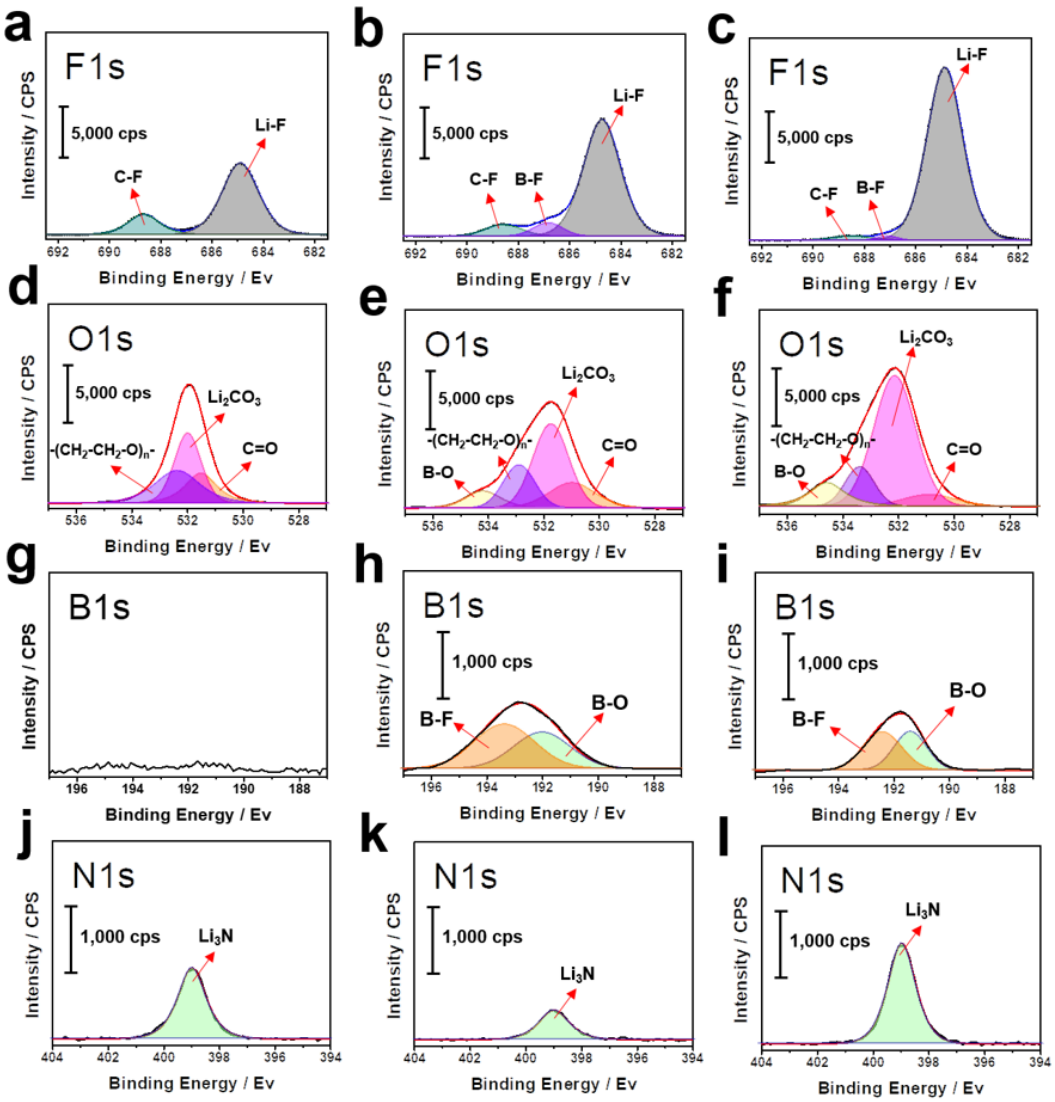

Figure 2.1. XPS spectra of F1s (a, b, c), O1s (d, e, f), B1s (g, h, i) and N1s (j, k, l) of the SEI layer surface after 1st deposition in Li/Cu cells: (a, d, g, j) 10EF31P, (b, e, h, k) 64EF31P, and (c, f, i, l) 82EF31P.

An ideal SEI is one that is permeable to Li^+, is ductile yet strong enough to withstand the mechanical stress associated with its compositional and dimensional changes upon cycling, and is insoluble in the electrolytic solution throughout its cycling-potential range. These qualities of the SEI depend heavily on its chemical composition and will facilitate the stable cycling of the lithium metal anode. We employed a FEC-based electrolyte in order to form a LiF-rich SEI layer. LiTFSI was the main salt of choice as it introduces species that contribute to the important SEI features discussed above and LiDFOB was added to further strengthen the SEI layer. The $LiPF_6$ salt was mixed in as an additive to prevent Al corrosion.[37]

Three electrolyte solutions: i) 1 M of LiTFSI + 0.05 M of $LiPF_6$ in EMC:FEC = 3:1 (referred to as 10EF31P), ii) 0.6 M of LiTFSI + 0.4 M of LiDFOB + 0.05 M of $LiPF_6$ in EMC:FEC = 3:1) (referred to as 64EF31P), and iii) 0.8 M of LiTFSI + 0.2 M of LiDFOB + 0.05M of $LiPF_6$ in EMC:FEC = 3:1 (referred to as 82EF31P) were synthesized and X-ray photoelectron spectroscopy (XPS) was performed on the SEI after the first deposition in Li/Cu cells to ascertain their chemical composition. The F1s, O1s, B1s, and N1s spectra are shown in Figure 2.1. As expected of the electrochemical decomposition from the FEC solvent and fluorine containing anions $TFSI^-$, $DFOB^-$, and PF_6^-, the peak corresponding to Li-F (684.5 eV) was observed in the F1s spectra for all three electrolytes (Figures 2.1a – c) with the 82EF31P SEI exhibiting an especially strong Li-F peak, followed by that of the 64EF31P SEI. Similarly, the Li_2CO_3 peak (531.8 eV) appeared stronger for the 82EF31P SEI compared to the other two SEIs in the O1s spectra (Figures 2.1d – f); LiF is produced

in reactions of metallic Li with FEC and the fluorine containing anions $TFSI^-$, $DFOB^-$, and PF_6^- and Li_2CO_3 is produced when metallic Li reacts with the carbonate solvents. These two peaks are of interest because LiF and Li_2CO_3 are less soluble in solvents and have a high Young's modulus of 64.9 Gpa and 75.0 Gpa,[44] contributing greatly to the physicochemical stability of the Li metal SEI. Yet despite their advantageous property, LiF and Li_2CO_3 are ionic insulators with conductivities of ~ 10^{-12} S cm^{-1} and ~10^{-15} S cm^{-1},[45,46] respectively, and limit the transport of Li^+ during fast charging. Fortunately, the integration of crystalline oligomeric borates like $Li_2B_4O_7$ and lithium borate glasses and Li_3N balances the drawback in ionic conductivity. The former are fast Li^+ conductors with conductivities greater than 10^{-7} S cm^{-1} which derive from the borate oligomer comprising oxygen double-bonded to boron to which Li^+ from proximal anionic oxygens single-bonded to boron can hop[47–50] and the latter has a high conductivity of 10^{-4} S cm^{-1}.[30] Since borates originate from LiDFOB, the borate B-O peak can be seen at 191.7 eV in the B1s spectra and at 534.6 eV in the O1s spectra (Figures 2.1d – i). The peak corresponding to the Li_3N can be seen at 399.1 eV in the N1s spectra (Figures 2.1j – l) and appeared the strongest in the 82EF31P SEI and weakest in the 64EF31P SEI.

Another component to consider is the quantity of organic compounds in the SEI layer. Organic matters are less desirable because they are not as physiochemically stable as inorganic compounds[51] and are prone to SEI damage due to having a low Young's modulus (less than 1 Gpa),[44] leading to dead lithium accumulation during prolonged cycling to hinder Li transport and accelerate dendrite nucleation and growth. Conversely,

inorganic components are less soluble in electrolyte[52] and their high Young's Modulus[53] increases the SEI mechanical strength and their Li^+ conductive nature makes inorganic-rich SEI more suitable during fast charge conditions where the SEI layer is under severe stress. In XPS, organic compounds are represented by the $-(CH_2-CH_2-O)_n-$ and C=O peaks at 533.5 and 530.5 eV in the O1s spectra (Figures 2.1d – f). Interestingly, the intensities of these peaks were opposite to inorganic compound intensities where the inorganic-rich 82EF31P SEI exhibited the weakest $-(CH_2-CH_2-O)_n-$ and C=O signals while inorganic-poor 10EF31P SEI showed the strongest organic signals which is in agreement with a recent report.[54] The inverse relationship suggests that when insoluble and nonporous films of inorganic lithium salts are formed, as is the case in 82EF31P, excessive solvent reduction is prevented.

2.3.2. Deposition morphology and Li/Li electrochemical cycling

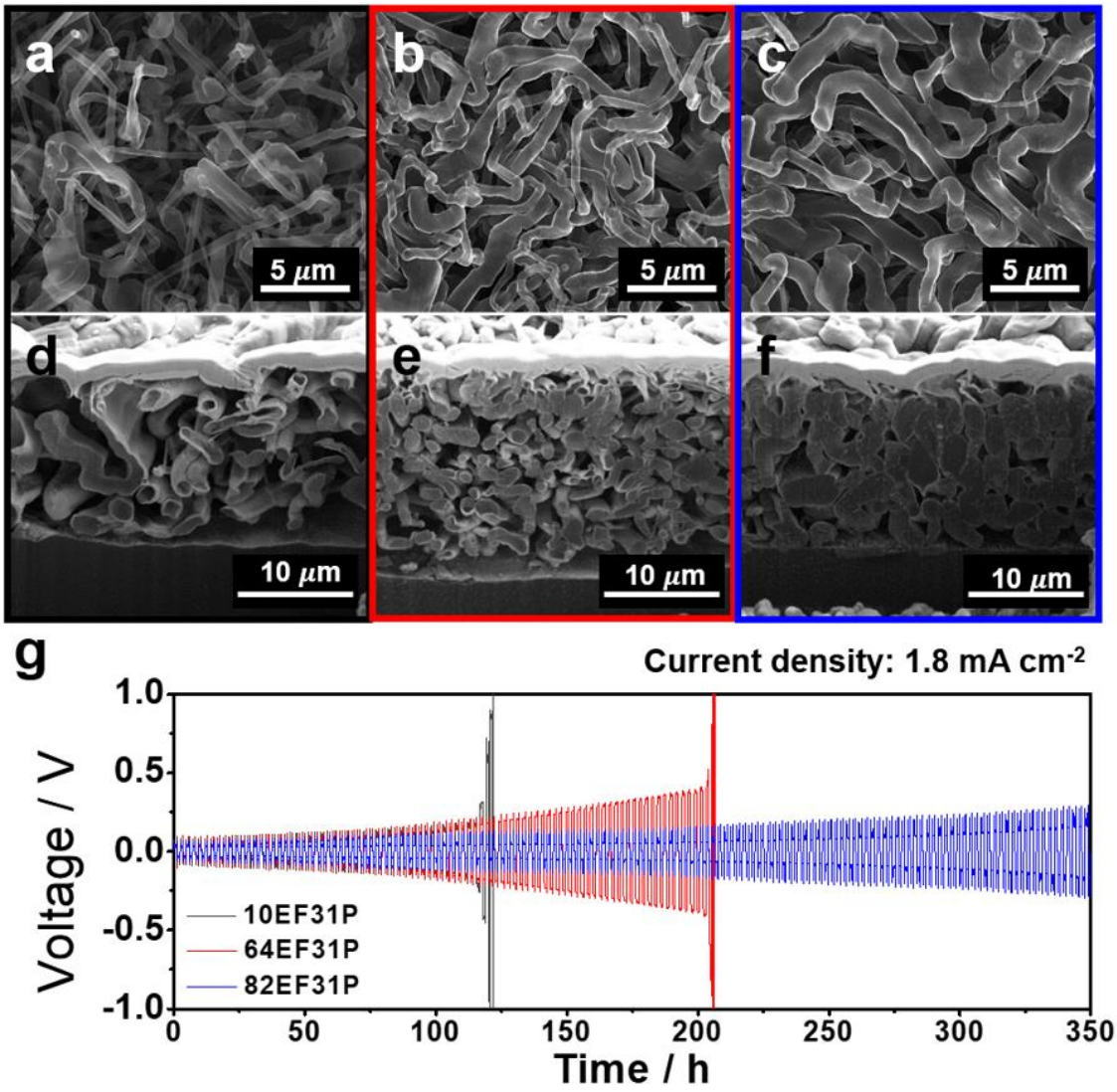

Figure 2.2. Comparison of deposited Li morphologies (top view a-c) and their cross-sectional SEM images (d-f). The Li was deposited on Cu-foil: (a and d) in the 10EF31P electrolyte, (b and e) 64EF31P, and (c and f) 82EF31P. (g) Voltage excursions during the galvanostatic Li deposition/stripping cycles of Li/Li cells at 1.8 mA cm^{-2} with the three different electrolytes.

The composition of the SEI layer profoundly affected the deposition morphology of lithium as seen in the scanning electron microscope (SEM) images of lithium deposited on

Cu foil in 2032-coin cells cycled at a fast charge rate of 1.8 mA cm^{-2} for 1 hour (Figures 2.2a – f).[45,55] As the SEM images present, the 10EF31P deposited lithium appeared as a network of intertwined wires, but the lithium structures were uneven, loosely-packed, and consisted of thin wires of ~ 0.6 μm diameter. The 64EF31P showed a better deposition morphology but its packing density was mediocre and was comprised of a mixture of thin and thick wires, likely due to a lack of ionic conductivity enhancing species. In contrast, the 82EF31P SEI layer, which was rich in SEI-beneficial species, displayed a substantially improved deposition morphology with lithium being deposited densely as ~ 1.2 μm thick microwire structures. At a lower current density of 0.9 mA cm^{-2} (Figure 2.3), a similar trend is observed, albeit more amplified. Moreover, the impact the SEI has on deposition morphology becomes more evident when lithium is deposited freely at 1.8 mA cm^{-2} for 1 hour in a Li/Li optical cell as observed in Figure 2.4. As the optical images reveal, when no pressure is applied, the 10EF31P and 64EF31P deposited lithium in a loose dendritic morphology whereas the 82EF31P deposited lithium in a uniform and compact morphology.

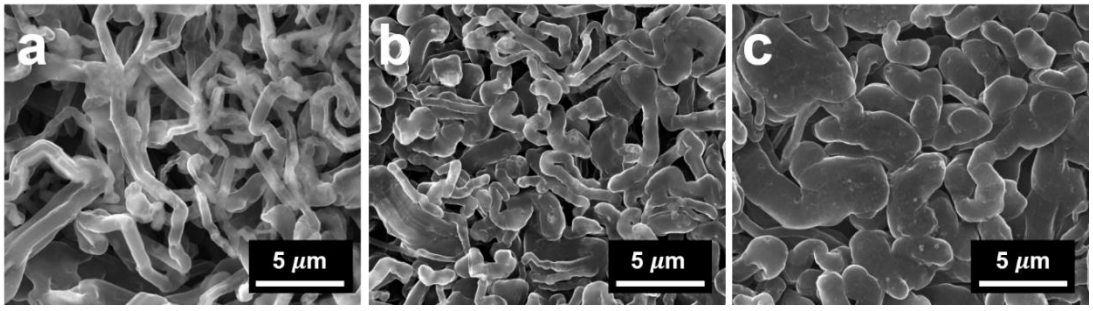

Figure 2.3. Comparison of SEM images of deposited Li morphologies from Li/Cu cell using different electrolyte solutions at 0.9 mA cm^{-2}: (a) 10EF31P, (b) 64EF31P, and (c) 82EF31P.

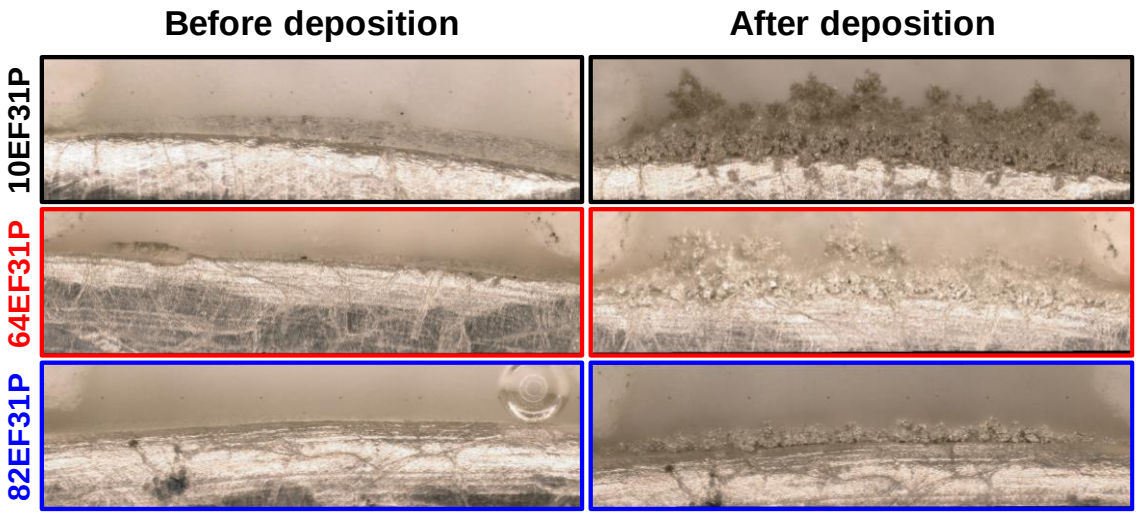

Figure 2.4. Comparison of optical images of deposited Li morphologies from Li/Li optical cell using 10EF31P (black), 64EF31P (red), and 82EF31P (blue) at 1.8 mA cm^{-2} for 1 hour.

Such differences in Li deposition morphologies can be further explained by the dendrite nucleation time, which follows a Sand's time relationship:[56]

$$t_{\text{Sand}} = \pi D_{app} \frac{(z_c c_0 F)^2}{4(J t_a)^2}$$

where t_{Sand} is the time required for dendrites to nucleate, D is the ambipolar diffusion constant, e is the electronic charge, c_0 is the initial concentration, J is the applied current density, and t_a is the anion transference number ($t_a = 1 - t_{\text{Li}^+}$). From the equation, it can be deduced that a higher Li^+ transference number (t_{Li^+}) results in a larger t_{Sand}, meaning that the SEI more effectively suppresses dendrite growth. Li^+ transference numbers were determined through electrochemical impedance spectroscopy (EIS) and chronoamperometry experiments (Figure 2.5) according to the Bruce and Vincent method[57] using Li/Li cells; the corresponding equivalent circuit of the EIS Li/Li cells is

shown in Figure 2.6. The resulting transference numbers of the different SEIs were t_{Li^+} = 0.476 for 10EF31P, t_{Li^+} = 0.493 for 64EF31P and t_{Li^+} = 0.525 for 82EF31P, respectively. Note that the initial current was calculated using Ohm's law: $I_0 = \Delta V\ (R_b + R_{int})$. Additionally, the initial overpotential values of 10EF31P, 64EF31P, and 82EF31P SEI layers, which were -0.0731 V, -0.05438 V, and -0.04842 V, respectively, show that the 82EF31P SEI experienced the least resistance in depositing Li through the SEI. Hence, the 82EF31P SEI layer effectively delays the dendrite nucleation time and facilitates lithium deposition to induce a dense and thick Li deposition morphology.

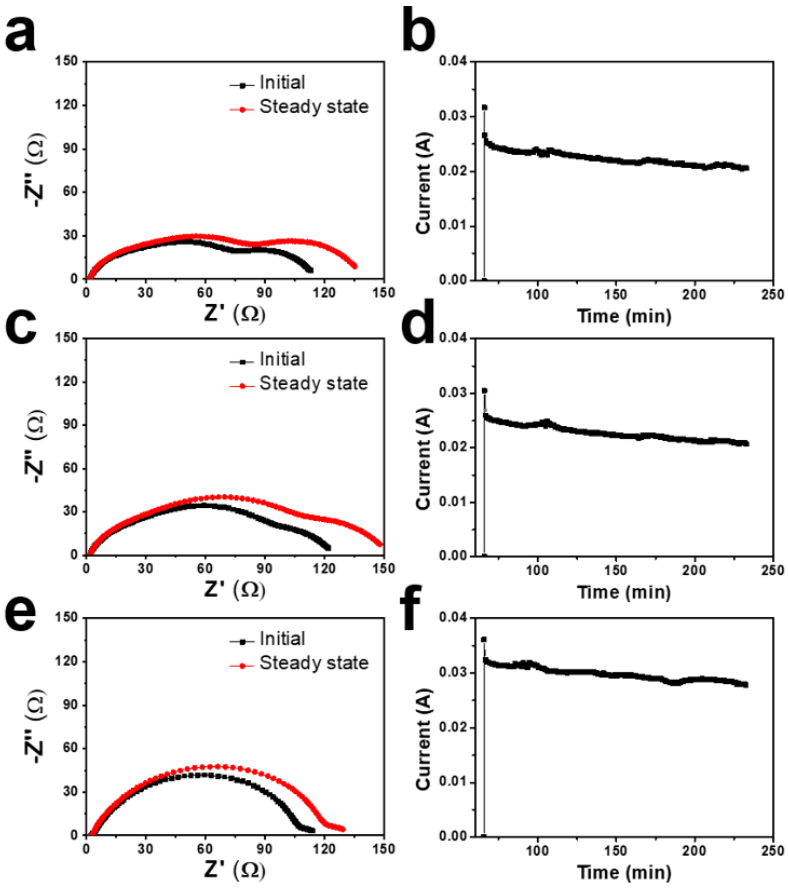

Figure 2.5. Impedance responses and chronoamperometry profiles of the Li/Li cells with (a and b) 10EF31P, (c and d) 64EF31P and (e and f) 82EF31P electrolytes.

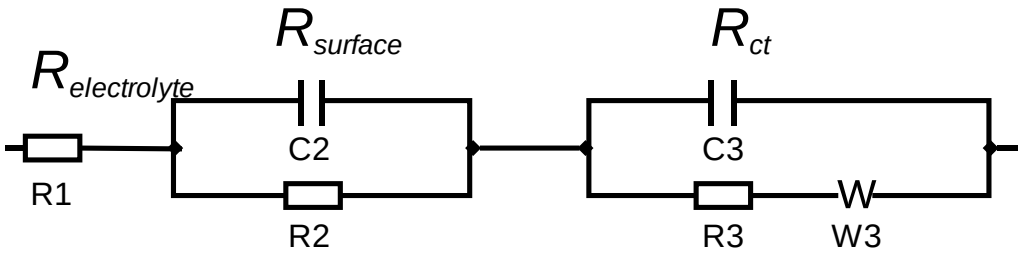

Figure 2.6. Equivalent circuit model of the EIS Li/Li cells of Figure 2.5.

The electrochemical performance of symmetrical Li/Li cells of the different electrolytes cycled galvanostatically at 1.8 mA cm^{-2}, are illustrated in Figure 2.2g. As augured by its poor deposition morphology and unfavorable chemical composition, the 10EF31P Li/Li cell showed progressively increasing overpotential curves and failed prematurely with a sudden voltage polarization at 120 hours, suggesting a heavy dead Li build-up. The 64EF31P cell cycled longer but also failed at 205 hours with an accelerated overpotential increase towards the end of its cycle life. On the other hand, the 82EF31P cell demonstrated a stable deposition/stripping cycling with minimal overpotentials for more than 350 hours which mirrors its favorable chemical composition and deposition structures. Similarly, under strenuous conditions of a very high current density of 3.6 mA cm^{-2}, the 82EF31P cell cycled to over 200 hours with suppressed overpotential while 10EF31P and 64EF31P cells failed at 74 and 82 hours, respectively (Figure 2.7). At a lower current density of 0.9 mA cm^{-2}, no distinguishable changes between the three different electrolyte cells were seen up to 500 hours (Figure 2.8). The ionic conductivities of the 10EF31P, 64 EF31P, and 82EF31P were calculated to be 2.39×10^{-3}, 2.04×10^{-3}, and 2.26×10^{-3} S cm^{-1}, respectively, which matches the trend observed in a previous report[58]

where the addition of LiDFOB to a LiTFSI-based solution lowers the ionic conductivity of the electrolyte; the large $TFSI^-$ anion size reduces interionic interaction and leads to a higher ionic mobility.[59,60] However, it should be noted that Li^+ transport in the cell is affected by other factors such as SEI surface resistance and charge transfer resistance, and the amalgamation of these components enables the improved cycling of the 82EF31P cell.

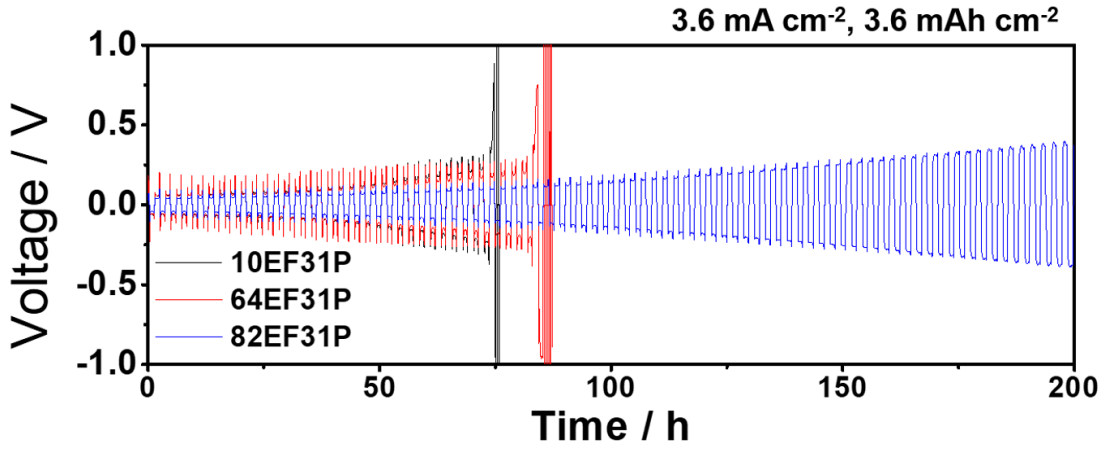

Figure 2.7. Voltage excursions during the galvanostatic Li deposition/stripping cycles of Li/Li cells at 3.6 mA cm^{-2} with the three different electrolytes.

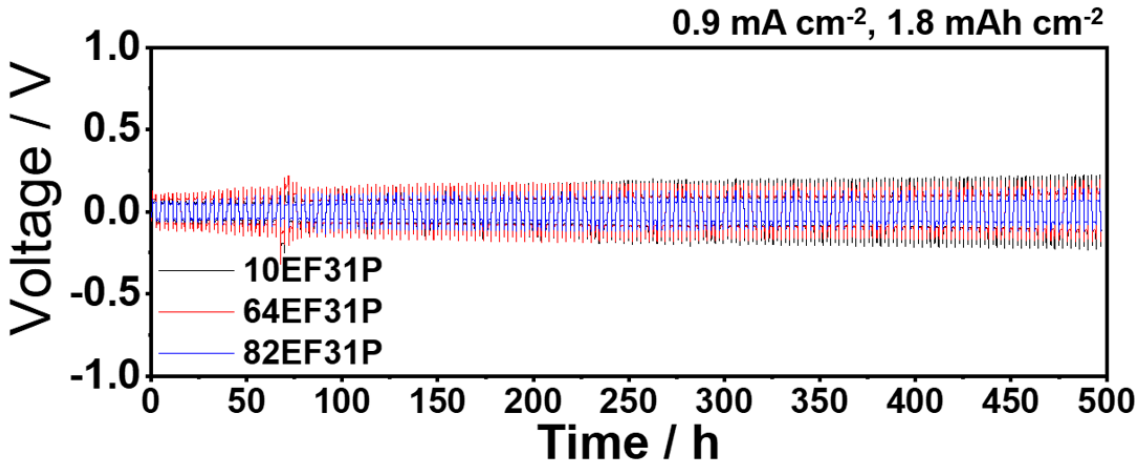

Figure 2.8. Voltage excursions during the galvanostatic Li deposition/stripping cycles of Li/Li cells at 0.9 mA cm^{-2} with the three different electrolytes.

2.3.3. Dead Li Layer

With each cycle, some of the lithium is lost as dead lithium that accumulates in the SEI layer. Figures 2.9a – c reveal the extent of Li loss after 50 deposition/stripping cycles in the Li/Cu cells, reflecting the efficacy of the SEI layer in preventing dead Li formation. The dead Li thicknesses were 124.8 μm, 84.8 μm, and 51.0 μm for 10EF31P, 64EF31P, and 82EF31P. To better quantify the extent of dead Li in the SEI layer, time-of-flight secondary-ion mass spectrometry (TOF-SIMS) depth profiling in positive polarity with a O_2^+ sputtering beam (~ 500 nA, 2 keV) was employed and the three-dimensional (3D) view of the Li_3^+ (representing the dead lithium) and Cu^+ (representing the bulk Cu foil) depth profiles for the 10EF31P, 64EF31P, and 82EF31P samples are presented in Figures 2.9d – f. Given the nature of the TOF-SIMS technique, which is based on fragmentation of the surface compounds, larger clusters consisting of the same element (such as Li_3^+) are usually representative of that element's bulk material (in this case, dead/bulk Li). Clearly, the thicknesses of the dead lithium layer match those seen in the cross-sectional SEM images and the dead lithium accounts for a larger amount in the SEI of 10EF31P. While a similar amount of inactive Li was present on the surface for the three SEI layers, the area under the curve (proportional to the total amount of dead lithium) was much less for 82EF31P SEI at 2868 counts compared to the other two SEI layers with 4833 counts (10EF31P) and 4396 counts (64EF31P). It should also be noted that the Li_3^+ signals of 10EF31P and 64EF31P were likely reduced due to the uneven and porous dead Li structures of 10EF31P and 64EF31P SEI layer that were significantly changing the effective acquisition area. Moreover, the average Coulombic efficiencies (CEs) of 10EF31P, 64EF31P, and 82EF31P

were 97.0 %, 98.3 %, and 98.8 %, respectively, which further lend credence that the maximization of SEI-beneficial compounds suppresses active Li loss. Likewise, the electrochemical impedance spectroscopy (EIS) value for 82EF31P Li/Cu cells experienced the least increase in resistance after 50 cycles (Figure 2.10 and Table 2.1).

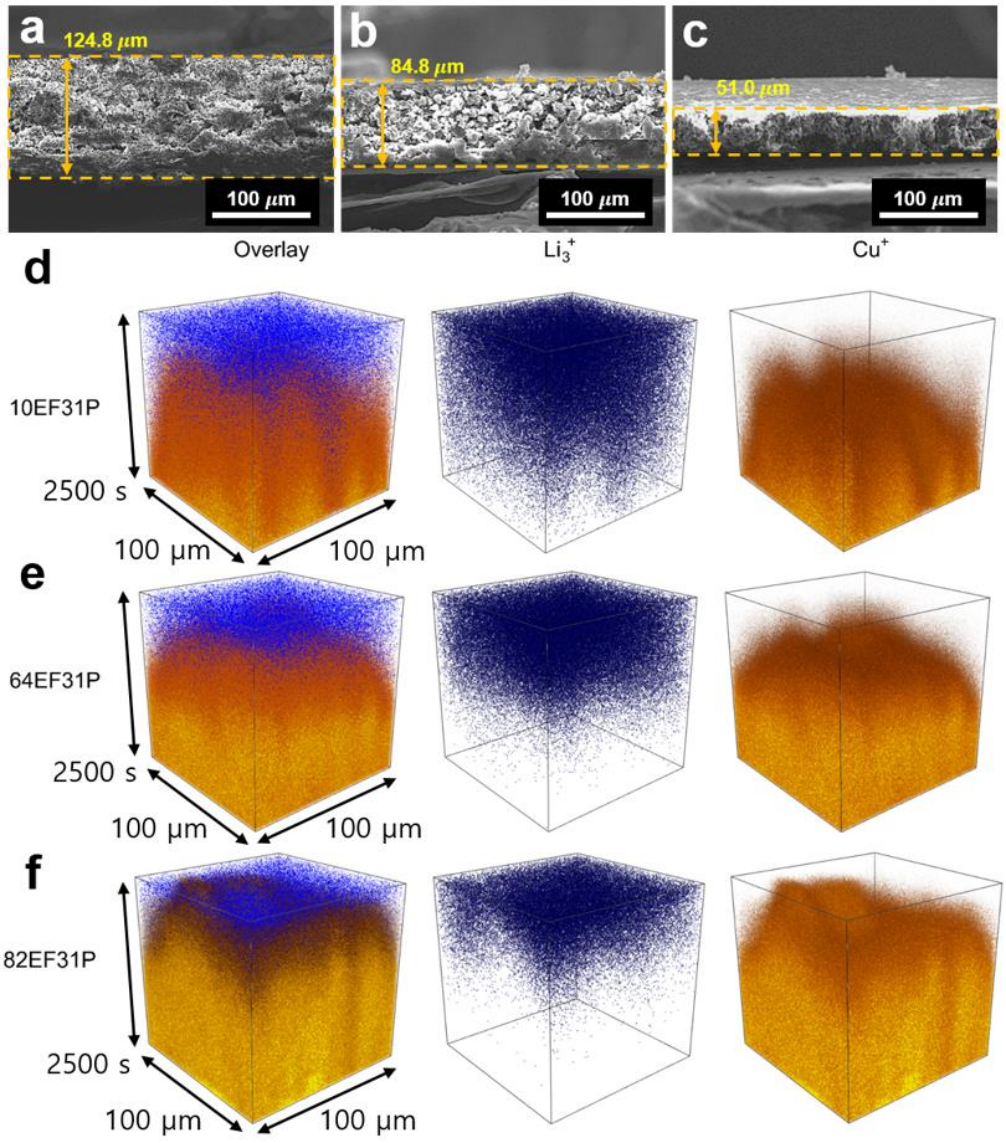

Figure 2.9. Cross-section views of cycled dead lithium layer collected from Li/Cu cells of (a) 10EF31P, (b) 64EF31P, and (c) 82EF31P after 50 deposition/stripping cycles. TOF-

SIMS 3D view of the dead lithium (represented by the Li_3^+ fragment) throughout the SEI in the (d) 10EF31P, (e) 64EF31P, and (f) 82EF31P samples We find the least amount of dead lithium in the 82EF31P SEI layer.

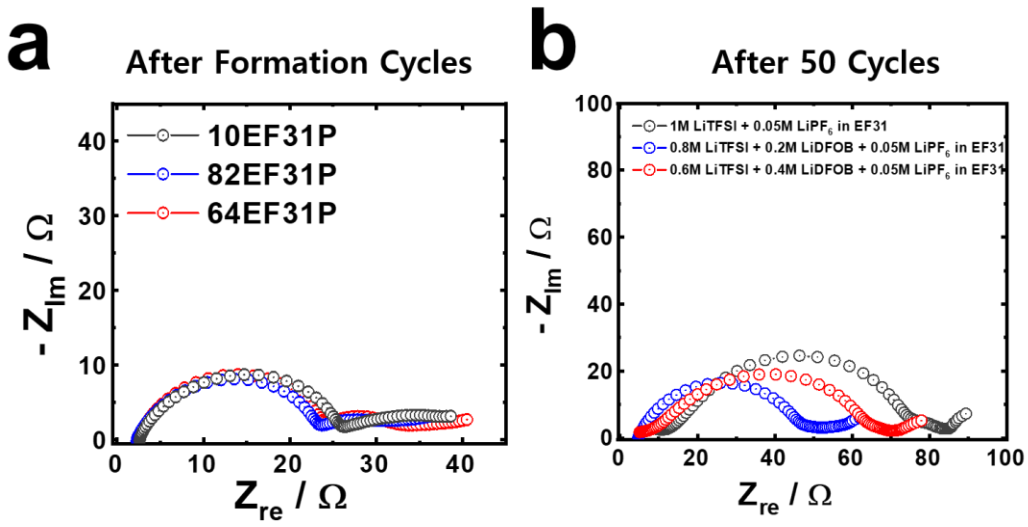

Figure 2.10. Electrochemical impedance spectroscopy of Li/Cu symmetrical cells with different electrolyte solutions measured (a) after formation cycle and (b) after 50 cycles.

Table 2.1. EIS values of 10EF31P, 64EF31P, and 82EF31P measured after formation cycle and after 50 cycles.

Sample	10EF31P	64EF31P	82EF31P
After Formation	22.5 Ω	20.6 Ω	20.1 Ω
After 50 Cycles	65.3 Ω	52.8 Ω	37.7 Ω

2.3.4. Full SEI layer TOF-SIMS chemical reconstruction

Indeed, the deposited lithium morphologies, deposition/stripping cycling performance, and dead Li quantity, all point to the 82EF31P solution providing a superior SEI layer relative to the 10EF31P and 64EF31P solutions. To gain more insight into the 82EF31P SEI layer, TOF-SIMS depth profiling was used to chemically reconstruct the full-depth of the 82EF31P SEI layer (as tested in Li/Cu cells) since the standard XPS depth of

information is surface limited (less than 10 nm).[61,62] Figure 2.11a shows the normalized to maximum depth profiles of various species of interest forming the SEI. Depth profile normalization is used to demonstrate the localization of various layers of the SEI: C_3H^- and $Li_2CO_3^-$ (corresponding to the organic part of the SEI and Li_2CO_3, respectively) reside mostly on the SEI surface; LiS^-, LiF_2^- and BO_2^- (corresponding to Li_2S, LiF, and oligomeric and glass borates, respectively) form the inner part of the SEI, while Cu_2^- corresponds to the bulk Cu foil electrode. The 3D views of these profiles are delineated in Figures 2.11b and c, demonstrating the stratified structure of the SEI. Here, a Cs^+ ion beam (~70 nA, 2 keV) was used for sputtering in order to penetrate completely through the SEI and reach the Cu substrate. An important point to note here is that Li_2S, which was absent in the XPS spectra, appeared remarkably strongly and evenly below the surface. Li_2S is of particular interest because it contributes concurrently to both mechanical robustness (Young's modulus of 82.6 Gpa)[44] and ionic conductivity (~ 10^{-5} S cm^{-1})[63] and is produced during the cycling.

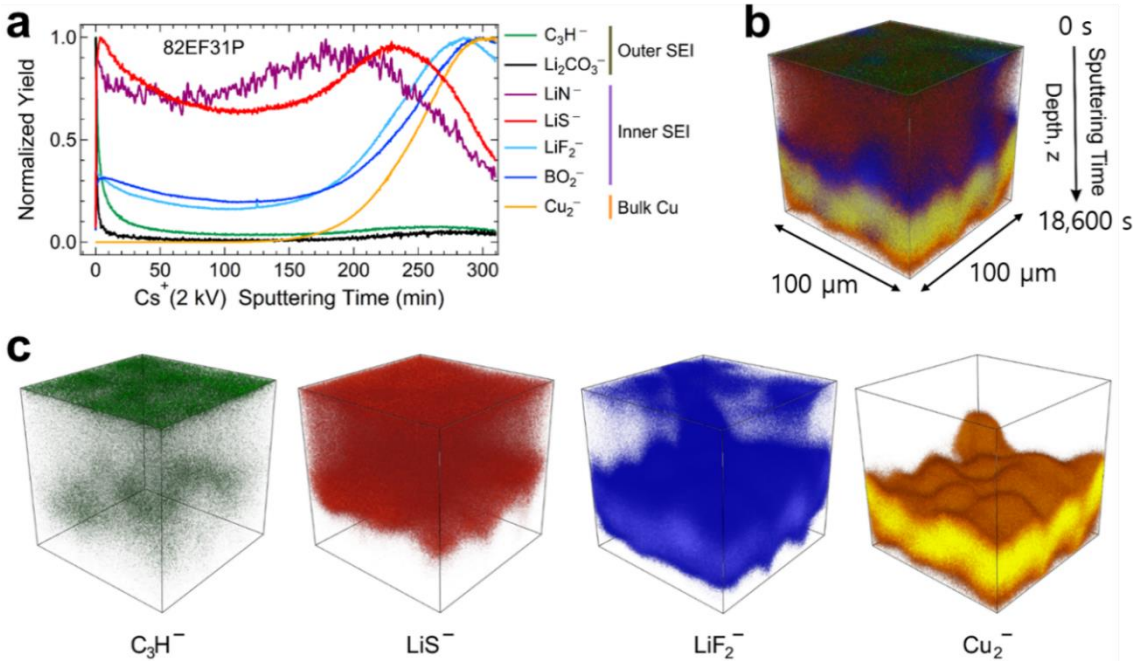

Figure 2.11. (a) TOF-SIMS depth profiles (normalized to maximum) of various species of interest acquired from the 82EF31P sample (in Li/Cu cell) with a Cs^+ at 2 kV ion energy sputtering beam. The chemical composition and depth localization of different layers of the SEI are identified: C_3H^-, $Li_2CO_3^-$, LiS^-, LiF_2^- and BO_2^-. (b, c) 3D view of the depth profiles in (a) showing the spatial localization of various species composing the SEI.

2.3.5. 82EF31P SEI layer mechanism and LMB electrochemical performance

How the chemical composition of the SEI layer influences its potency and subsequent deposition morphology/active lithium retention is illustrated in Figure 2.12a. The 10EF31P SEI is mechanically weak due to the lack of LiF and Li_2CO_3 which results in the deposited lithium breaking off at weak points to leave behind electrically disconnected dead Li. In contrast, the 64EF31P SEI possesses high structural modulus but is low in ionic conductivity due to poor Li_3N content and experiences difficulty with Li^+ transport. Only the 82EF31P SEI layer features both high mechanical strength and ionic conductivity due

to the minimization of organic compounds and ample integration of SEI-beneficial compounds in the SEI.

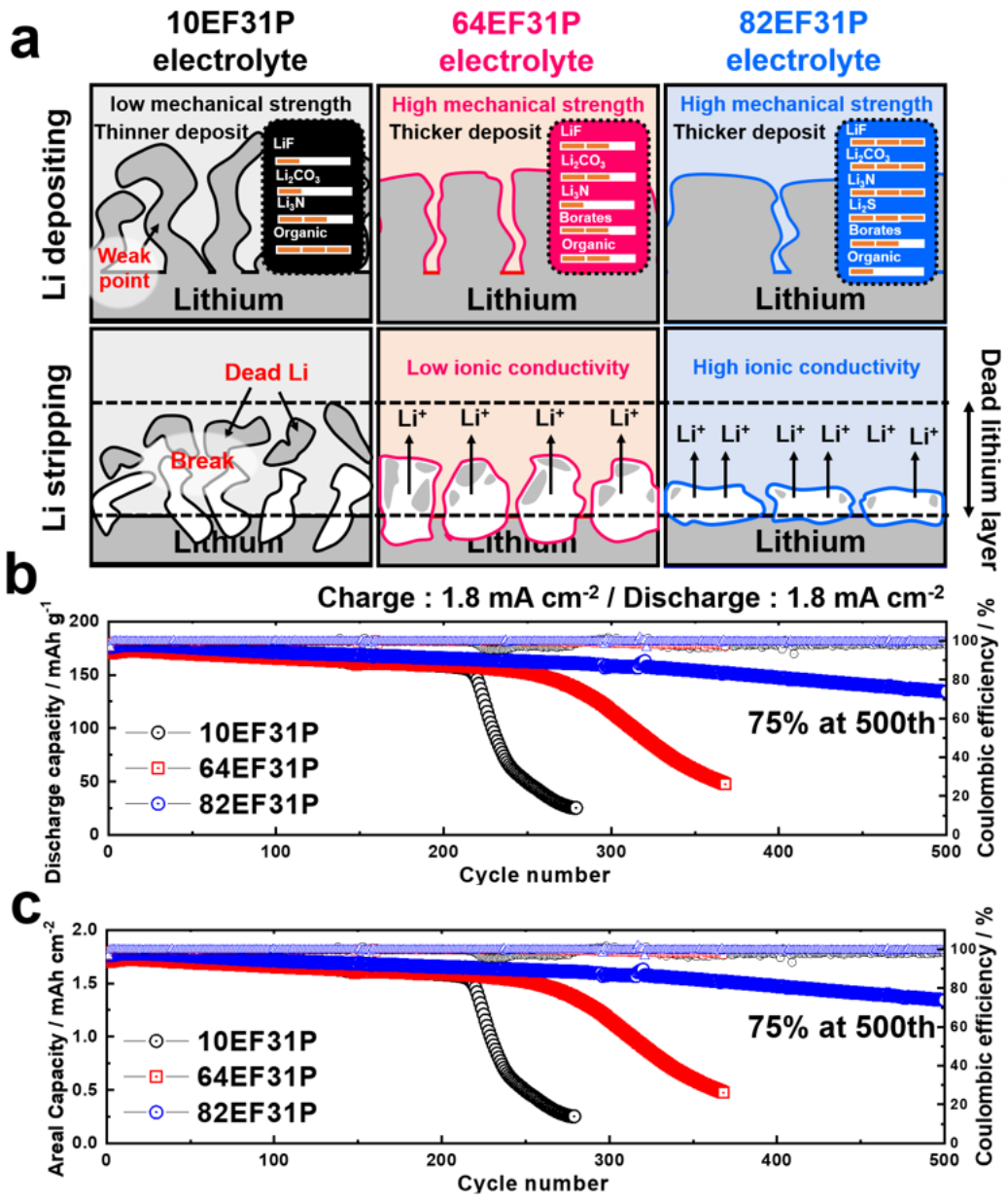

Figure 2.12. (a) Proposed illustration summarizing the multicomponent inorganic-rich SEI layer of 82EF31P (blue) compared to the SEIs of 10EF31P (black) and 64EF31P (red). Long-term cycling performance of a Li/NCM622 cell with 10EF31P, 64EF31P, and

82EF31P electrolyte solutions as a function of (b) discharge capacity (mAh g^{-1}) and (c) areal capacity with a cathode loading of 10 mg cm^{-2} cycled at a high current density of 1.8 mA cm^{-2}.

As a result, when coupled with a cathode in a proto-type lithium-metal anode battery, the 82EF31P dual-salt electrolyte cell displayed a promising electrochemical performance as seen in Figures 2.12b and c where the former is in discharge capacity (mAh g^{-1}) and the latter is Coulombic efficiency. At a rapid charge-discharge rate of 1.8 mA cm^{-2} and a high $Li[Ni_{0.59}Co_{0.2}Mn_{0.2}Al_{0.1}]O_2$ (NCM622-Al 1%) cathode loading of 10 mg cm^{-2}, the 82EF31P cell delivered a specific discharge capacity of 177 mAh g^{-1} and stable cycling with 75 % capacity retention after 500 cycles. In contrast, the 10EF31P and 64EF31P cells failed prematurely similarly to the Li/Li symmetrical cell performance. Note that the $Li[Ni_{0.6}Co_{0.2}Mn_{0.2}]O_2$ cathode was doped with 1 % Al to increase the structural integrity of the cathode particle, minimizing capacity loss due to cathode concerns.[14,64] Moreover, despite having large amounts of Li being passed back and forth in cycling, the 82EF31P electrolyte was able to maintain Coulombic efficiencies higher than 99.3 % throughout its 500 cycles, implying comparatively little loss of active lithium. As a control, we have also tested the Li/Li and Li/NCM cycling performances of 1.05 M LiTFSI and 1.05 M $LiPF_6$ in EMC:FEC = 3:1 electrolytes as shown in Figures 2.13 and 14. The promising performance of the 82EF31P electrolyte-SEI cell is also reflected in its rate capability performance at various C-rates (Figure 2.15) where the 82EF31P cell outperformed the 10EF31P and 64EF31P cells. The performance demonstrated by 82EF31P at higher C-rates can be ascribed to the inorganic compounds being well-distributed throughout the SEI, enabling

the transport of lithium through the SEI. The promising performance shown by the 82EF31P cell is possible because the holistic inclusion of LiF, Li_2CO_3, Li_3N, Li_2S, and oligomeric and glass borates in the SEI layer bolsters its role as a protection layer and ionic conductor, thereby enabling the SEI layer to stabilize the lithium-metal anode for use in a long-term high energy density LMB.

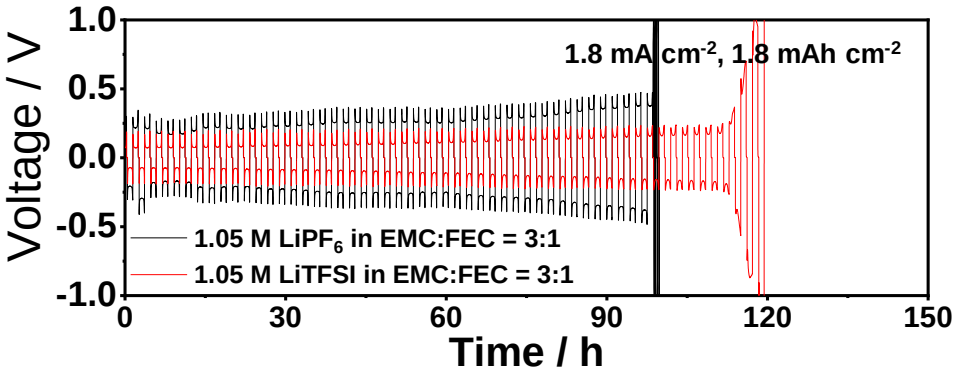

Figure 2.13. Voltage excursions during the galvanostatic Li deposition/stripping cycles of Li/Li cells at 1.8 mA cm^{-2} with the 1.05 M $LiPF_6$ and 1.05 M LiTFSI in EMC:FEC = 3:1 electrolytes.

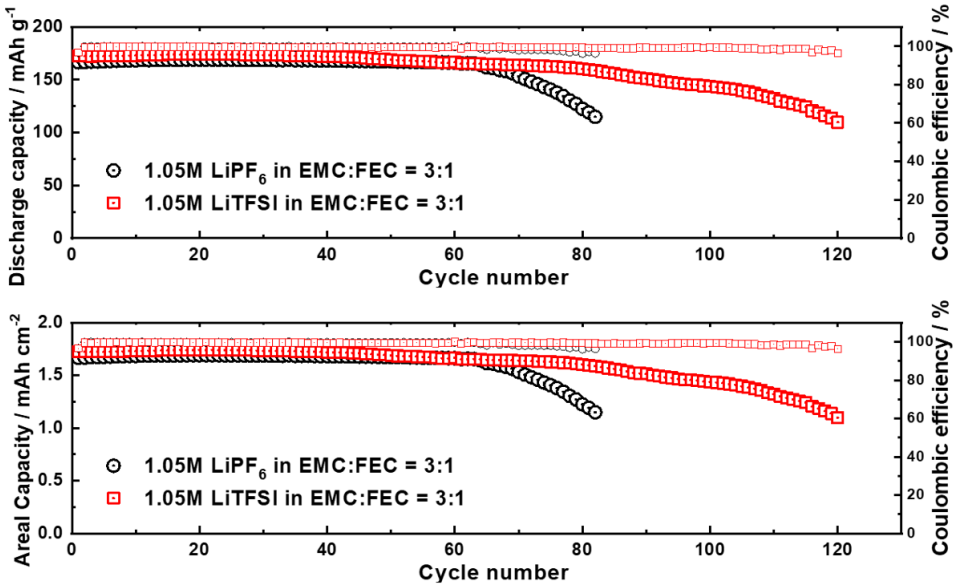

Figure 2.14. Long-term cycling performance of a Li/NCM622 cell with different electrolytes with cathode loading of 10 mg cm^{-2} cycled at a high current density of 1.8 mA

cm^{-2} where the top graph is in discharge capacity (mAh g^{-1}) while the bottom graph is in areal capacity (mAh cm^{-2}).

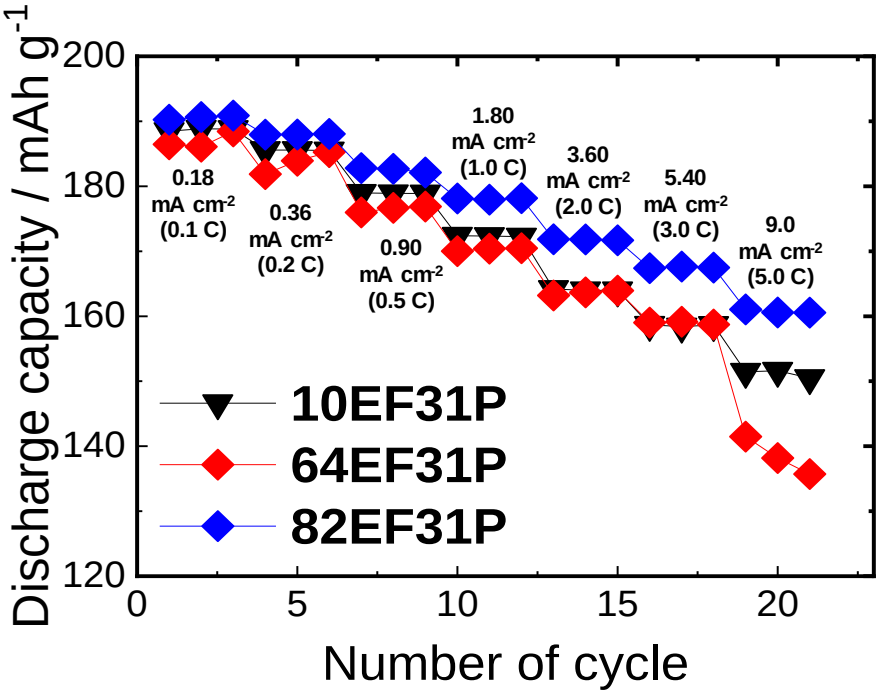

Figure 2.15. Rate capability test and charge/discharge curves from three different electrolyte cells at the same charge/discharge current.

2.4. Summary

In summary, a multicomponent inorganic-rich SEI layer was designed through the combination of LiTFSI and LiDFOB salts dissolved in a FEC-based electrolyte. The 0.8 M LiTFSI + 0.2 M LiDFOB + 0.05 M $LiPF_6$ in EMC:FEC = 3:1 (82EF31P) electrolyte solution introduced a multitude of SEI-beneficial inorganic compounds (LiF, Li_2CO_3, Li_3N, Li_2S, and cross-linked O-B-O oligomeric and glass borates) into the SEI layer while the preferential reduction of salts over carbonate electrolytes significantly lowered the content of organic compounds in the SEI layer. The resulting inorganic-rich composition substantially enhanced the mechanical robustness and ionic conductivity of the SEI layer,

enabling the stabilization and preservation of the active lithium-metal. Consequently, the resulting SEI layer enabled the Li/Li cell to deliver a stable deposition/stripping cycling for more 350 hours and the Li/Li[$Ni_{0.59}Co_{0.2}Mn_{0.2}Al_{0.01}$]$O_2$ lithium-metal battery to deliver an overall 75 % capacity retention at 500 cycles with greater than 99.3 % Coulombic efficiencies at a current density and specific discharge capacity of 1.8 mA cm^{-2} and 177 mAh g^{-1}, respectively. Through this work, we hope to demonstrate that a multi-inorganic SEI layer is more efficacious in its role as a protective and ionically conductive layer than SEI layers concentrated with a single beneficial species. Future efforts to further increase the content of the aforementioned species or add other inorganic compounds through additives could better stabilize and preserve lithium metal for a superior performance lithium-metal battery.

Chapter 3. Beyond Doping and Coating: Prospective Strategies for Stable High-Capacity Layered Ni-rich Cathodes*

3.1. Introduction

Lithium-ion batteries now dominate in energy storage, with their application expanding from portable electrical and electronic devices to transportation. Their societal impact has been recognized by the award of the 2020 Nobel Prize in chemistry to John Goodenough,[1] Stanley Whittingham,[2] and Akira Yoshino.[3] On the business side, their sales have grown tremendously from ~ 20 GWh ($7.24 billion) in 2010 to ~ 120 GWh ($26.73 billion) in 2017.[4,5] A significant portion of this market consists of electrical vehicles (EVs), and this market is on track to explosively grow from the 4 million EVs on the road in 2018 to a lower estimate of 50 million EVs and a higher estimate of 225 million EVs by 2030.[4] This growth, in part, is a result of environmental policies aimed at reducing urban air pollution. Following this, most automobile manufacturers have expanded their EV research, development, and engineering efforts and are annually introducing improved hybrid and EV models.

EVs were invented in the late 19th century, but failed to penetrate the market because of their limited range, high price, and difficulty in charging. Interestingly, the same old challenges persist today. Appropriately, serious concerns regarding the market

* **Sun, H.H.;** Ryu, H. H.; Kim, U. H.; Weeks, J. A.; Heller, A.; Sun, Y. –K.; Mullins, C. B. Beyond Doping and Coating: Prospective Strategies for Stable High-Capacity Layered Ni-rich Cathodes. *ACS Energy Lett.* **2020**, *5*, 1136 – 1146. Ho-Hyun Sun wrote the work. Prof. Mullins and Prof. Heller supervised the project. All participated in the discussion and preparation of the manuscript.

competitiveness of EVs have been raised and a 300-mile driving range in a single charge has been suggested as the threshold for the commercial success of EVs.[7,14] Therefore, a massive amount of ongoing research, development, and engineering efforts have been devoted to the development of higher energy density LIBs at a cheaper cost to alleviate the uncertainties surrounding EVs. Within this effort, the replacement of Co by Ni in the $LiCoO_2$ provides the triple benefit of lower cost, higher voltage, and higher specific capacity.

Theoretically, $LiNiO_2$ (LNO) and $LiCoO_2$ (LCO) have similar specific capacities of 274 and 275 mAh g^{-1}, as they are adjacent to each other in the periodic table of elements. In practice, their actual specific capacities differ greatly (247 mAh g^{-1} and 156 mAh g^{-1} at 0.1 C and 4.3 V, respectively)[15,16] due to the latter having a higher starting discharge voltage and a limited Li utilization as compared to the former. Additionally, the enthalpy of formation of LCO at 298 K is −141 kJ/mol while that of LNO is −55 kJ/mol. The third advantage regards the lower cost of Ni, at a current price of \$14 kg^{-1}, compared to the \$31 kg^{-1} for Co. Consequently, the layered $Li[Ni_xCo_yMn_z]O_2$ (NCM) and $Li[Ni_xCo_yAl_z]O_2$ (NCA) cathodes have already replaced the LCO cathode in the LIB EV market.[10,18] Still, the appeal for even higher energy densities at a lower cost have pushed the Ni fractions in the NCM and NCA cathodes to exceed 60%, resulting in high-capacity Ni-rich NCM and NCA cathodes.

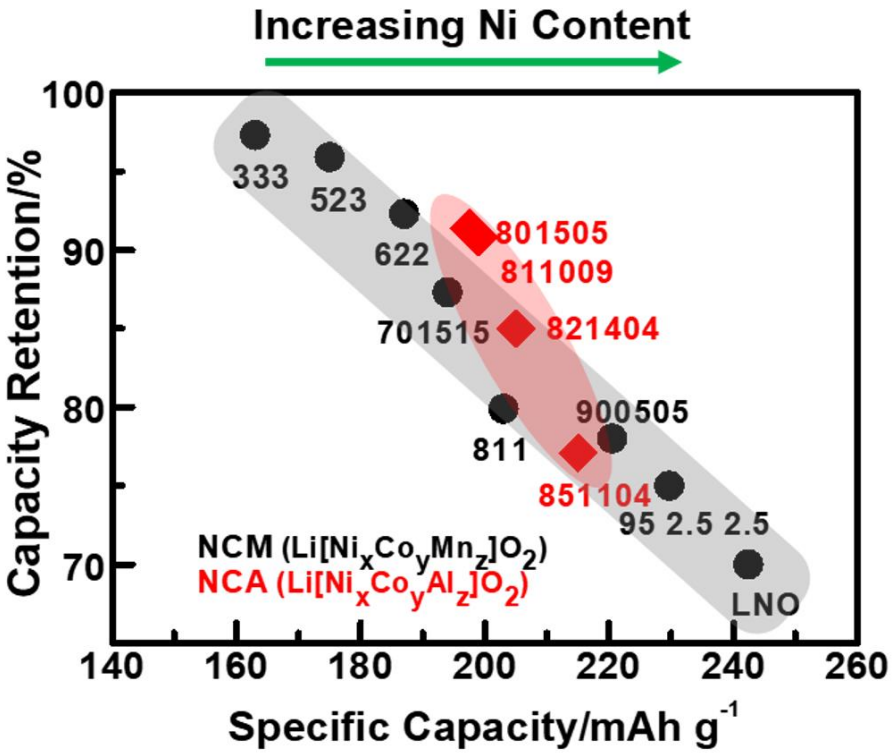

Figure 3.1. Specific capacity (mAh g^{-1}) vs. capacity retention over 100 cycles (%) plot of various layered NCM and NCA cathodes showing the trade-off between stability and capacity at increasing Ni content. Reproduced with permission with permission from reference 65. Copyright 2017, The American Chemical Society.

The inclusion of more Ni in the NCM and NCA cathodes has enabled significant advances in LIB energy densities. This increase is, however, accompanied by sacrifices in cycling and thermal stabilities due to the weaker Ni-O bonds destabilizing the crystal structure and increasing the anisotropic volume change upon Li-extraction/insertion. The surface chemical reactivity is also exacerbated owing to the more oxidizing redox potential of the $Ni^{3+/4+}$. Such a trade-off between capacity and stability is accentuated with increasing Ni fractions (Figure 3.1), especially above 80% Ni, to reflect similar behavior observed in $LiNiO_2$, and decrease the cyclability.[16,66–69] This is attested by the Panasonic NCA

cathodes, wherein the depth-of-discharge (DOD) is limited to 60% during extended cycling to prevent a rapid capacity fade.[70–72]

Here, we consider the current strategies aimed at alleviating the capacity fade of layered Ni-rich NCM and NCA cathodes to achieve both high capacity and cycling stability. We discuss first the processes leading to the degradation of the high-Ni cathodes upon their cycling to discuss the challenges faced by these cathodes. Then we consider the conventional methods of atomic doping and surface coating and outline their limitations to illustrate how these methods only postpone but do not overcome the capacity fade issue. Finally, we focus on prospective approaches of cathode micro- and nano-structural modifications that have gained prominence as they offer counters to the inherent degradation mechanisms associated with layered Ni-rich cathodes and be easily integrated into current cathode manufacturing processes for scale-up production.

3.2. Discussions

3.2.1. Layered Ni-rich NCM and NCA degradation mechanism

The Ni-rich NCM and NCA cathode degradation mechanism has been an important point of discussion in the field of batteries for some time. Studies by Yang et al. suggest that the capacity fade and loss of thermal stability are processes initiated at the surface. At high Ni-content, the surface of the original layered lattice ($R\bar{3}m$) converts upon cycling to the M_3O_4-type disordered spinel ($Fd\bar{3}m$) lattice, which then transforms into the inactive rock-salt ($Fm\bar{3}m$) lattice near the surface.[73,74] This structural distortion is driven by the oxidation of surface-contacting electrolytic solution by the strongly oxidizing $Ni^{3+/4+}$ sites.

The resulting surface-film impedes the transport of Li^+ and Li is irreversibly consumed in its formation. Aurbach et al. showed that this is the prime damaging process, establishing that both cathode material and electrolytic solution are consumed in the formation of the cathode-electrolyte interphase (CEI).[75] The formed CEI layer comprises LiF, other metal fluorides, $ROCO_2Li$, $ROCO_2$-transition metals, and polycarbonates and thickens during cycling to increase electrical and ionic resistance at the surface.

Subsequent studies revealed that the Ni-rich cathodes degrade further via microcrack generation from within the particle. Early studies by Ukyo et al. reported the observation of microcracks in cycled $Li[Ni_{0.8}Co_{0.15}Al_{0.05}]O_2$ particles and hinted that the large resistance increase originates from the morphological and structural change of the fracturing cathode particles.[76] Watanabe et al. substantiated this by showing that electrolyte penetration occurs via microcracks along the grain boundaries into the $Li[Ni_{0.76}Co_{0.014}Al_{0.10}]O_2$ secondary particle.[70–72] The surface exposed upon cracking did not have the layered lattice structure of the bulk, but possessed a high-impedance NiO-like lattice structure. These cracks originate from the large angle differences of the randomly oriented primary particles and lead to mechanical stress accumulation along the grain boundary regions during anisotropic volume changes of structural phase transitions.[77] This process ultimately results in particle fracturing and leads to fresh surface exposure. Ni-rich cathodes undergo multiple phase transitions (as indicated by X-ray diffraction results) during the lithium extraction and insertion process, where the original layered structure (H1) changes to a monoclinic phase (M) and subsequently to two other hexagonal phases (H2 and H3).[78–80] Among these phase transitions, Sun et al. stated that the H2 → H3 phase

transition, occurring at ~ 4.2 V for greater than 80 atomic % Ni cathodes, is considered to be the most strenuous and engenders extensive crack networks throughout the secondary particles.[66,67] The damage is particularly evident when LNO cathodes are cycled to strongly oxidizing potentials: upon their cycling to 4.1 V, 95% of the original capacity is retained and no cracks are observed in the particle; however, when the same cathodes are cycled to 4.3 V, they retain only 75% of their original capacity and extensive particle fracturing is seen after 100 cycles.[16] In order to avoid cracking, Watanabe et al. recommended the restriction of cathode cycling to 60% depth-of-discharge (DOD), regardless of the specific voltage region.[70–72] Nevertheless, a recent study has shown that $Li[Ni_{0.95}Co_{0.04}Al_{0.01}]O_2$ cathodes cycled to the upper 60% DOD, (3.76 – 4.3 V, 65.6% retention) deteriorated faster than those cycled with the lower 60% DOD (2.7 – 4.0 V, 96.1% retention) and a full 100% DOD (2.7 – 4.3 V, 85.5% retention), thus further highlighting the significance of the H2 → H3 phase transition.[81]

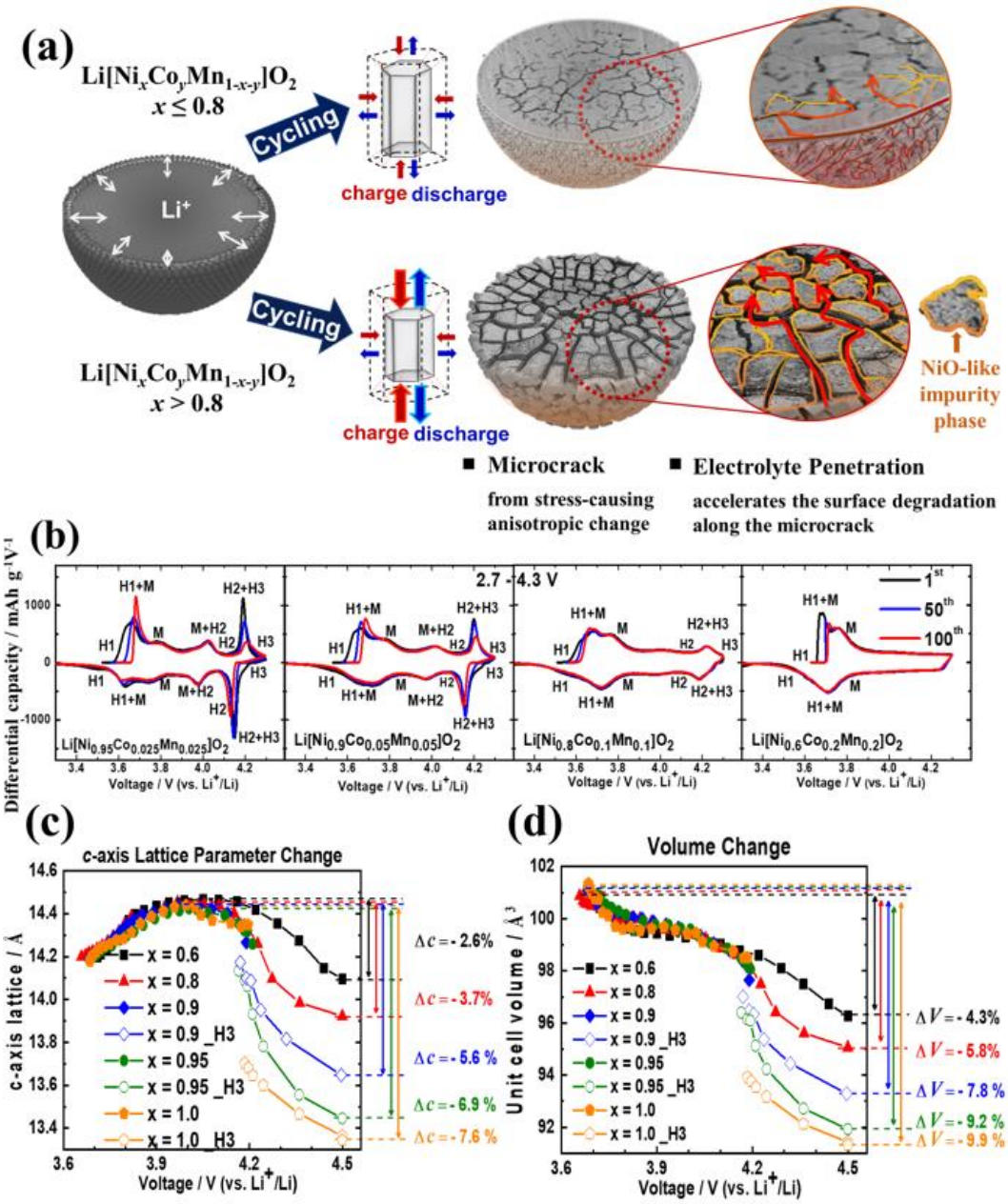

Figure 3.2. (a) Schematic of degradation pathways of Ni-rich cathodes. Those with less than 80% Ni largely degrade from surface deterioration while those with greater than 80% Ni degrade through microcrack generation along grain boundaries and subsequent electrolyte penetration. (b) dQ dV^{-1} profiles of $Li[Ni_xCo_yMn_{1-x-y}]O_2$ (x = 0.95, 0.9, 0.8, and 0.6). (c) c-axis lattice parameter and (d) volume change in the unit cell during charging of

$Li[Ni_xCo_yMn_{1-x-y}]O_2$ (x = 0.6, 0.8, 0.9, 0.95, 1.0). Reproduced with permission from reference 67. Copyright 2018, The American Chemical Society.

These studies suggest that the Ni-rich NCM and NCA cathodes degrade through a mixture of degradations at the surface and particle cracking from the interior. Comprehensive studies have mapped the degradation processes of Ni-rich NCM and NCA cathodes with 60, 80, 90, 95, and 100 atomic% Ni content, as illustrated in Figure 3.2a.[66,67,81] Layered cathodes of less than 80% Ni predominantly lose capacity by surface degradation as the H2 → H3 phase transition is absent, and there are few microcracks. In the $Li[Ni_{0.6}Co_{0.2}Mn_{0.2}]O_2$ cathode, as much as 96.5 % of the capacity is retained over 100 cycles as seen in Figure 3.3 along with the cycling data of Ni = 0.8, 0.9, 0.95, and 1.0.[67] In contrast, as the Ni content exceeds 80%, the magnitude of the H2 → H3 phase transition increases with the Ni-content (Figure 3.2b) to engender extensive crack networks along the grain boundaries, which function as channels for electrolyte infiltration into the interior. Consequently, the capacity fade and impedance increase are accelerated as the infiltrated electrolyte reacts with the exposed and reactive Ni^{4+} to form an insulating NiO-like impurity and other electrolyte oxidation products.[65–67,82,83] The *c*-axis lattice parameter and volume changes during charge for Ni-rich NCM cathodes (60, 80, 90, 95, and 100 atomic% Ni) are depicted in Figure 3.22c and d to better quantify the parameter changes. Note that the *a*-axis lattice parameter does not change much with increasing Ni. While parasitic side reactions still persist at the surfaces of Ni-rich NCM and NCA particles, much more damage is caused by the microcracks (Figure 3.2a).

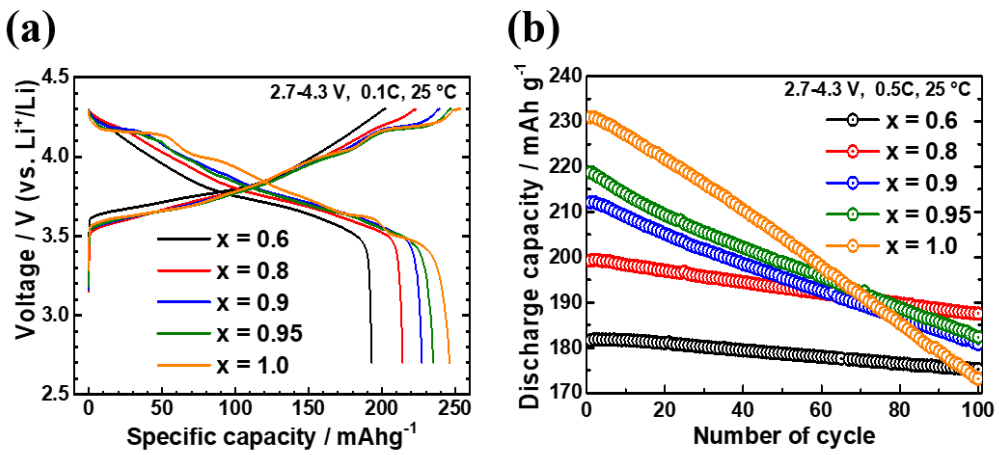

Figure 3.3. Fundamental electrochemical data of $Li[Ni_xCo_yMn_{1-x-y}]O_2$ (x = 0.6, 0.8, 0.9, 0.95, and 1.0) cycled in half-cells. (a) Initial charge and discharge curves at 0.1 C and (b) cycle performance at 0.5 C.

3.2.2. Conventional Strategies: Atomic Doping and Surface Coating

In this regard, numerous strategies have been employed to alleviate failure and achieve both high capacity and stability, with atomic doping being the one of the most prominent and conventional strategies. Atomic doping reinforces the structural integrity of the Ni-rich cathodes through the substitution of atoms in the crystal lattice with stabilizing dopants. The introduction of small amounts of calcium,[84] magnesium,[85] aluminum,[86–88] titanium,[89,90] zirconium,[91] molybdenum,[92] tungsten,[93] niobium,[94] and tellurium[95] in place of Ni, Co, and Mn sites has been effective in mitigating the extent of volume changes during phase transitions to preserve the crystal structure under high delithiation conditions. For example, Guo et al. recently reported that 1% Al doping in $Li[Ni_{0.8}Co_{0.1}Mn_{0.1}]O_2$ improves the storage stability and capacity retention.[88] Moreover, metal dopants have the additional effect of providing charge compensation to balancing electrostatic repulsion and reducing cation mixing, as reported by Luo et al. where Ti^{4+} doping of

$Li[Ni_{0.8}Co_{0.1}Mn_{0.1}]O_2$ halved the amount of Ni^{2+} in Li sites from 6.76% to 3.13% and improved cathode kinetics at 2 C cycling from 136 mAh g^{-1} to 157 mAh g^{-1}.[90] Anionic oxygen can also be substituted with the more electronegative fluorine[85,96] to achieve energetically stronger M-F bonding to enhance the stability of Ni-rich cathodes and provide protection from HF attacks or nitrogen,[96] hence increasing the interslab distance to achieve enhanced rate capability.

A myriad of publications provide evidence regarding the proficiency of atomic doping, yet it merely delays the onset of the cathode degradation process. Although the modification reinforces the coherency of the crystal lattice with stabilizing dopants, it does not rectify the random orientation of the primary crystallites from which the inhomogeneous volume expansion/shrinkage originates. As such, mechanical stress continues to build up at the grain boundaries with large angle differences to eventually entail capacity loss and particle fracturing, albeit delayed. Eventually, the process follows the same degradation pathway as unmodified Ni-rich cathodes. Moreover, the applied dopants are inactive and are sometimes costly materials, and the financial cost of sacrifice in capacity for stability achieved by atomic doping needs to be considered before its implementation.

Surface coating is another widely applied modification method and is intended to reduce the parasitic side reactions with the electrolyte. Thus far, a plethora of coating materials have been applied and though they all act as a barrier to prevent electrolyte contact with the cathode to suppress side reactions, many of the coatings provide additional benefits. Oxide[97–99] coatings act as HF scavengers by sacrificially reacting with HF to

preserve the cathode surface against corrosion, while the more thermodynamically stable fluoride[100–102] and phosphate coatings[103,104] bypass the reaction to form a stable buffer layer during initial cycles. For example, the AlF_3 coating layer has been used to extend the cycle and shelf life of $Li[Ni_{0.8}Co_{0.15}Al_{0.05}]O_2$ cathodes at an elevated temperature of 60 °C.[48]

However, the electrically insulating nature of many of these coatings hinder cell performance at fast charge-discharge rates and electrically conductive carbon and polymer based coatings have been employed as alternative coatings to improve the charge transfer process at the surface of the Ni-rich cathodes. Choi et al. enhanced the kinetics of $Li[Ni_{0.6}Co_{0.1}Mn_{0.3}]O_2$ using a CVD-grown graphene ball coating to result in a 78% capacity retention in a full-cell at 5 C and 60 °C over 500 cycles.[105] Li^+ conducting Li-compounds[106–108] and ionically conductive polymers[109–111] have also been used as surface coating layers, since the transport of Li^+ frequently constitutes the rate limiting step in the cell. Wu et al. combined Li_3PO_4 and PPy as dual-conductive layers to further facilitate Li^+ transport for increased $Li[Ni_{0.8}Co_{0.1}Mn_{0.1}]O_2$ capacity and cycle life.[111] Concurrent doping and coating methods have also been reported as a dual-modification strategy to counter both the bulk microcracking and surface side reactions.[112]

Despite the efficacy of surface coating, the method has several drawbacks.[113,114] Similar to atomic doping, it adds inactive weight and lowers the energy density of NCM and NCA cathodes. More critically, the available coating techniques are inadequate. Dry coating applies a layer of coating material directly via the ball-mill, but this method results in a non-uniform coating. In contrast, wet coating methods employ liquid as a medium to attain a more homogeneous coating, but the surface of Ni-rich cathodes, especially those

with greater than 80% Ni, is altered in the process due to lithium leaching from the crystal lattice and the liquid medium reacting with Ni^{3+} to form impurity compounds. More critically, even though the surface coating strategy effectively protects the cathode surface, it is inadequate in preventing microcrack generation and subsequent electrolyte infiltration observed in cathodes with higher than 80% Ni. Other methods, such as atomic layer deposition (ALD) and chemical vapor deposition (CVD) can successfully produce a coating layer of desired uniformity and thickness, but these energy intensive techniques are not economically viable from a commercial viewpoint.

3.2.3. Concentration Gradient Cathodes

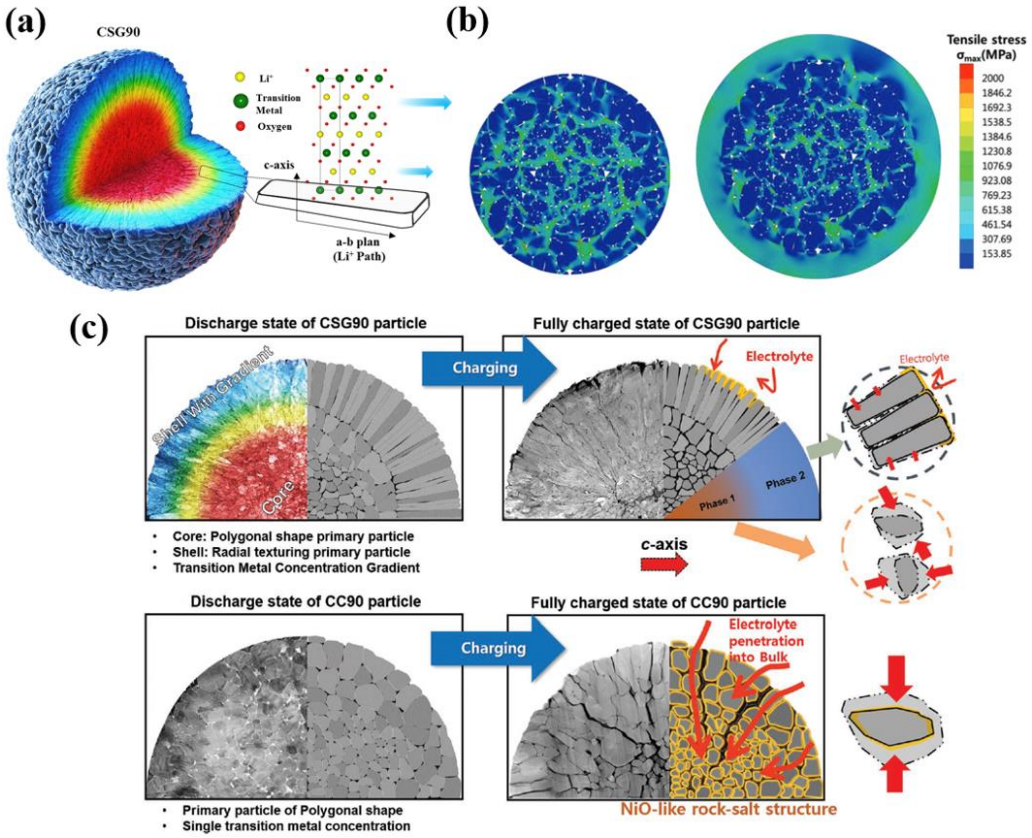

Figure 3.4. (a) Schematic diagram of a concentration gradient cathode. (b) Tensile stress distribution model of primary particles in a typical cathode (left) and a concentration

gradient cathode particle (right). (c) Morphological design of concentration gradient cathode (top) preventing electrolyte penetration, and typical cathode (bottom) failing to prevent electrolyte penetration during charging. Reproduced with permission from reference 115. Copyright 2019, Wiley-VCH.

Nevertheless, many years of research on layered Ni-rich NCM and NCA cathodes have yielded alternative approaches that directly address the failure mechanism of the materials. One such example is the core-shell gradient (CSG)[28,115–118] and full-concentration gradient (FCG)[119–123] cathodes. These materials approach the capacity and stability conundrum from a design perspective by placing the high-capacity, yet unstable and reactive, Ni in the particle core while allocating the low-capacity, but chemically stable, Mn at the particle exterior as illustrated in Figure 3.4a. Thus, the Mn-rich exterior functions similarly to a coating layer, in that it shields the Ni-rich core by minimizing the $Ni^{3+/4+}$-electrolyte parasitic side reactions at the surface. It differs from the coating layer in that all materials are electrochemically active and contribute to the capacity and electrical conductivity. Concurrently, the concentration gradient cathodes are fully compatible with the current cathode manufacturing equipment and processes and enable facile control of the Mn-rich exterior region thickness, avoiding the addition of an extra step in the manufacturing process.[124]

The CSG cathode is as described above, with a transition metal concentration gradient in the shell region to neutralize the crystal lattice mismatch of the core and the shell region. The FCG cathode further extends the gradient throughout the whole particle, from the surface to the center, to substantially enhance its cycling and thermal stability,

especially under high voltage cycling conditions.[119,125] In the wide voltage window of 2.7 – 4.5 V, the FCG cathode delivers a specific capacity of 215.4 mA h g^{-1} with an impressive capacity retention of 88% after 100 cycles. Moreover, the FCG cathode cell exhibits no combustion during the nail penetration test despite being charged to 4.2 V and experienced no substantial temperature increase when overcharged to 250% SOC or 12 V, respectively. The corresponding voltage and temperature vs. time graphs are shown in Figures 3.5 and 3.6. Note that despite continuous charging during the overcharge test, the FCG cell voltage did not fully reach 250% SOC or 12 V and dropped off after reaching 5.5 V. Dual- and triple-slope gradients have also been synthesized to further strengthen surface protection and safety.[126–129] Nevertheless, it is important to recognize that the excessive inclusion of gradients limits the Ni content and a rational design should precede the synthesis to satisfy the requirements of a high energy density concentration gradient cathode.

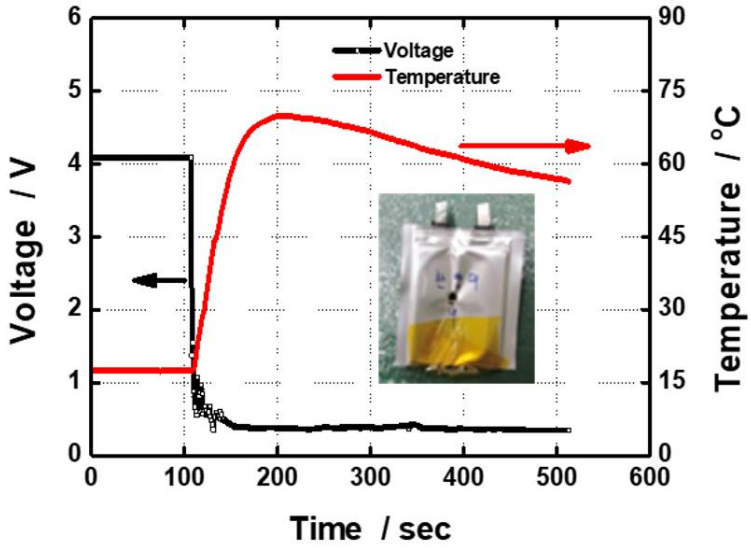

Figure 3.5. Voltage and temperature vs. time graph of FCG65 vs. graphite cell charged to 4.2 V during nail penetration test. The cell temperature does not climb up to combustion temperatures.

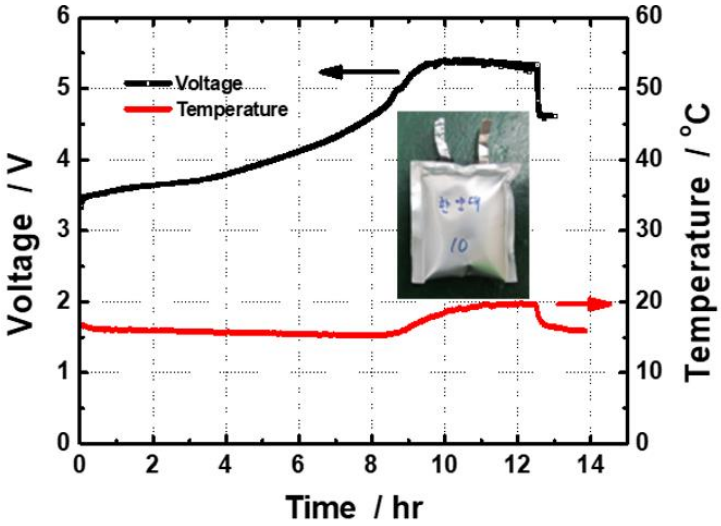

Figure 3.6. Voltage and temperature vs. time graph of FCG65 vs. graphite cell when charged to 250 % SOC or 12 V. The cell voltage lingers ~ 5.5 V but does not fully climb up to 250 % SOC or 12 V.

Another characteristic feature of the concentration gradient cathodes is the radially elongated rod-like primary particles in the exterior region that are aligned perpendicular to the surface (Figure 3.4a).[28,65,115,130,131] These crystals are compactly packed and their Li-containing (003) crystal planes are aligned in parallel, radiating from the particle center to its surface to minimize the tortuosity of the path of inbound or outbound Li^+ ions. More importantly, columnar elongated grains in the shell encase the randomly oriented grains of the Ni-rich core to alleviate the stress associated with the taxing H2 → H3 phase transition. Two-dimensional finite element analysis calculations (Figure 3.4b) show that the highly aligned geometry of the shell induces a homogeneous stress field to dissipate tensile stress in the core such that the microcracking is suppressed and the cracks do not propagate to the surface upon prolonged cycling.[115] As a result, the capacity fading and impedance increase caused by interparticle boundary surface degradation from direct contact with

infiltrated electrolyte is prevented, as illustrated in Figure 3.4c, hence enabling the concentration gradient cathode to continuously deliver high specific discharge capacities during long-term cycling. This also has the added effect of reducing transition metal dissolution as seen in Figure 3.7. The capability of the material is demonstrated by a highly Ni-rich $Li[Ni_{0.9}Co_{0.05}Mn_{0.05}]O_2$ CSG cathode, which cycled with 88% capacity retention at 1 C with no substantial crack development over 1000 cycles.[115]

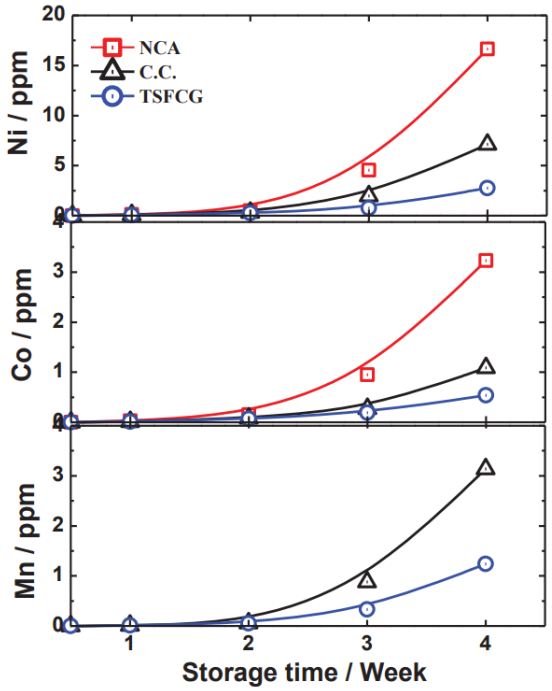

Figure 3.7. Comparison of Ni, Co, and Mn metal dissolution amounts of conventional $Li[Ni_{0.80}Co_{0.15}Al_{0.05}]O_2$ and $Li[Ni_{0.65}Co_{0.13}Mn_{0.22}]O_2$ cathodes and two-slope full concentration gradient (TSFCG) $Li[Ni_{0.65}Co_{0.13}Mn_{0.22}]O_2$ after charging to 4.3 V and storage in fresh electrolyte for 1, 2, 3, and 4 weeks.

3.2.4. Microstructure Modified Cathodes

Microstructure modified cathodes constitute another emergent class of Ni-rich NCM and NCA cathodes. These cathodes are conceived through dopants such as boron,[132]

aluminum,[130,133] and tungsten[134] but differ from the conventional dopants in that the distinct morphology of the primary crystallites preserve the coherency of the secondary particle. Park et al. reported that the boron doping of $Li[Ni_{0.90}Co_{0.05}Mn_{0.05}]O_2$ results in a cathode composed of thin directionally-elongated primary particles, similarly observed in gradient cathodes (Figure 3.8a).[132] Density functional theory (DFT) calculations shows that the boron modifies the surface energies of the NCM lattice, increasing the energy of the (104) plane and lowering the energy of the (003) plane to produce the geometrically correlated microstructure. In the resulting primary particle microstructure, just as with concentration gradient materials, the stress induced by anisotropic volume change is reduced, resulting in a 91% capacity retention with no particle cracking compared to the 76% capacity retention of its unmodified counterpart at 0.5 C and 55 ° C after 100 cycles.[132]

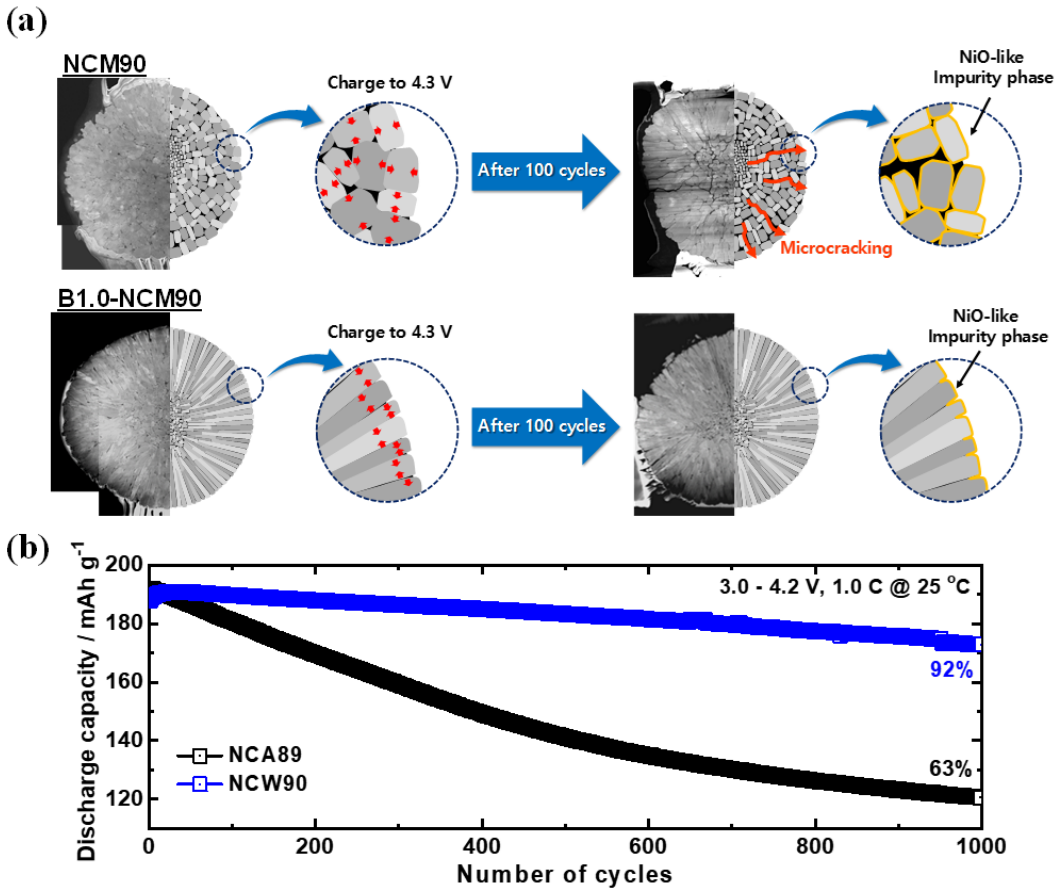

Figure 3.8. (a) Morphological representation of primary particle microstructure influence on cell performance (top: typical cathode, bottom: boron-doped microstructure cathode). Reproduced with permission from reference 82. Copyright 2018, Wiley-VCH. (b) Long-term cycling performance of $Li[Ni_{0.885}Co_{0.1}Al_{0.015}]O_2$ and $Li[Ni_{0.9}Co_{0.09}W_{0.01}]O_2$ cathodes vs. graphite using pouch-type full-cells (graphite anode) at 1 C and 25 ºC within the 3.0 – 4.2 V voltage range. Reproduced with permission from reference 134. Copyright 2019, Wiley-VCH.

Further, the replacement of Al with W in the Ni-rich NCA also results in an advantageous modification of the $Li[Ni_xCo_yW_{1-x-y}]O_2$ (NCW) cathode. Its microstructure comprises thin, nanosized, primary particles.[134] Just as nanosized silicon particles lessen the adverse effect of volume expansion upon lithiation, microcrack formation by

anisotropic volume expansion is suppressed with the nanosized needle-like grains of $Li[Ni_{0.9}Co_{0.09}W_{0.01}]O_2$.[135] Through its tailored microstructure, the NCW cathode also dissipates the internal strain, as interparticle boundaries make the paths of propagating cracks so tortuous that crack propagation is difficult. As a result, the NCW90 cathode displayed an impressive 92% capacity retention after 1000 cycles (vs. 63% of $Li[Ni_{0.885}Co_{0.1}Al_{0.015}]O_2$) at 1 C in a pouch-type full-cell, despite the high abundance of Ni content in the cathode material (Figure 3.8b).[134]

3.2.5. Single Grain Cathodes

Cracking along the grain boundaries is also avoided in cathode-materials made of a single, large, grain. This type of cathode was first introduced in the late 1990s and early 2000s for LCO synthesis and has since steadily gained prominence. Studies by those such as Dahn et al. showed that their single crystalline morphology improves the electrochemical and thermal properties, as the lack of grain boundaries enables resistance to crack formation, as seen in Figure 3.9.[136,137] Still, Ni-rich cathodes are ceramics, which have high tensile strength but are brittle, and the majority of studies reported so far on single crystalline cathodes are of less than 80% Ni, in which the disruptive H2 → H3 phase transition is suppressed, and do not report long-term cycling. Hence, further in-depth studies on single crystalline cathodes are needed to evaluate their morphological robustness and structural integrity at higher than 80% Ni under full-cell testing conditions.

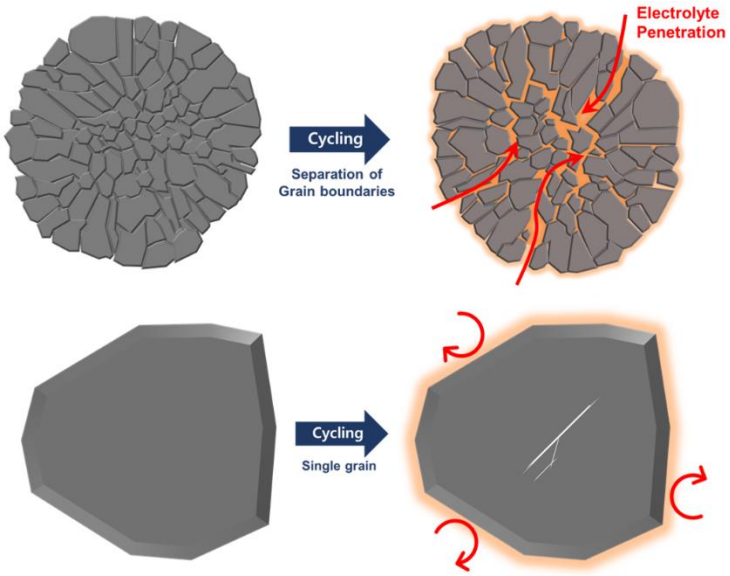

Figure 3.9. Schematic illustration of typical polycrystalline cathode (top) vs. single crystalline cathode (bottom) during cycling.

Additionally, single crystalline cathodes have great potential in being employed as smaller sized cathodes in commercial cathodes. Commercial cathodes employ a bimodal distribution of larger and smaller particles to increase the packing density. Single crystalline particles can be employed as the smaller cathode component to capitalize on its advantage and size, in a similar manner to how smaller silicon anode particles are resistant to volume expansion. However, other challenges such as size and morphology control remain.

3.2.6. Heterostructure Cathode

Heterostructure cathodes have likewise started to garner attention as a new type of modified cathode. These cathodes are structurally partitioned into two structurally disparate core and shell regions, where the former consists of the layered phase while the latter consists of an ordered spinel or rock-salt phase. In the past, spinel or rock-salt phases

were considered to be detrimental degradation products of the layered NCM and NCA phases, observed in damaged or extensively cycled cathodes. Nevertheless, Cho et al. found the thermal stability to improve in a heterostructure $Li[Ni_{0.54}Co_{0.12}Mn_{0.34}]O_2$ cathode with a less than 0.5 μm thick $Li_{1+x}[Ni_xCoMn_{2-x}]_2O_4$ spinel phase.[138] Later studies have shown that the presence of a tailored spinel or rock-salt structure can remarkably improve the stability of the layered cathodes, as in the case in which rock-salt phase regions were introduced at the surfaces of LNO and other Ni-rich cathodes through charge compensation with W^{6+}.[139,140] The rock-salt phase at the surface was confirmed by automatic TEM phase-identification/orientation mapping (ASTAR), as seen in Figure 3.10a. The resulting heterostructure cathodes were stable, cycling over 1000 cycles at full DOD with little electrolyte-infiltration or rise in impedance (Figure 3.10b). The materials exhibited high capacities typical of Ni-rich materials while concurrently overcoming their inherent cycling instability, with the tungsten-stabilized $Li[Ni_{0.8}Co_{0.15}Mn_{0.05}]O_2$ heterostructure cathode cycling notably with close to no drop in the capacity compared to the 25% capacity fade of unmodified $Li[Ni_{0.82}Co_{0.14}Al_{0.04}]O_2$. In a related study, Guo et al. formed a NiO-like phase between $Li[Ni_{0.815}Co_{0.15}Al_{0.035}]O_2$ and its Li_2MoO_4 coating layer by balancing the charge with Mo^{6+} to form a protective pillaring layer, thereby improving cathode stability.[53]

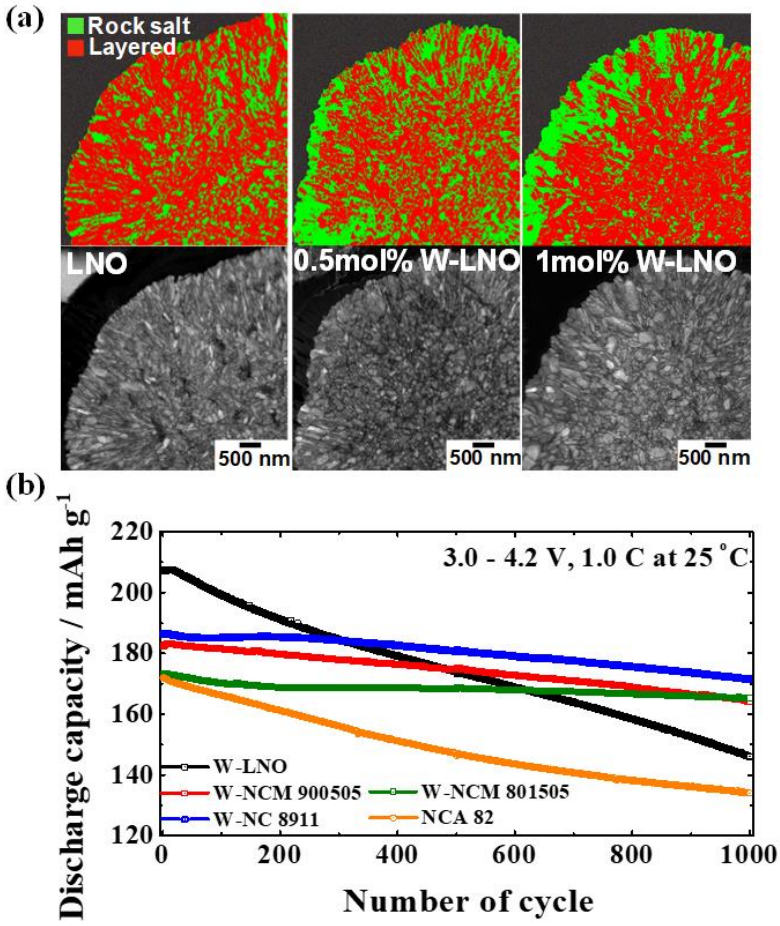

Figure 3.10. (a) Automatic TEM phase-identification/orientation mapping technique (ASTAR) analysis differentiating rock-salt and layered phases and corresponding bright field images of tungsten doped LNO. (b) Long-term cycling performance of various Ni-rich cathodes vs. graphite using pouch-type full-cells (graphite anode) at 1 C and 25 ºC in the 3.0 – 4.2 V voltage range. Reproduced with permission from reference 139. Copyright 2018, The Royal Society of Chemistry.

Thus far, the method by which the integration of the Li/Ni cations facilitates the ordering of the heterostructures at the surface to stabilize the cathode has not been extensively explored. We suspect that the stability and minor volume changes of the rock-salt phase mitigate the detrimental impact of the surface chemical attacks and microcrack

generation, especially in highly delithiated states. DFT calculations and HR-TEM showed that the Li/Ni ordered heterostructures are energetically favorable and cause the energy threshold for Li extraction to decrease to lower the stress on the host materials.[130,141] Further investigation on the effects of heterostructure incorporation would be necessary before it can be successfully utilized for application in Ni-rich cathodes.

3.3. Summary

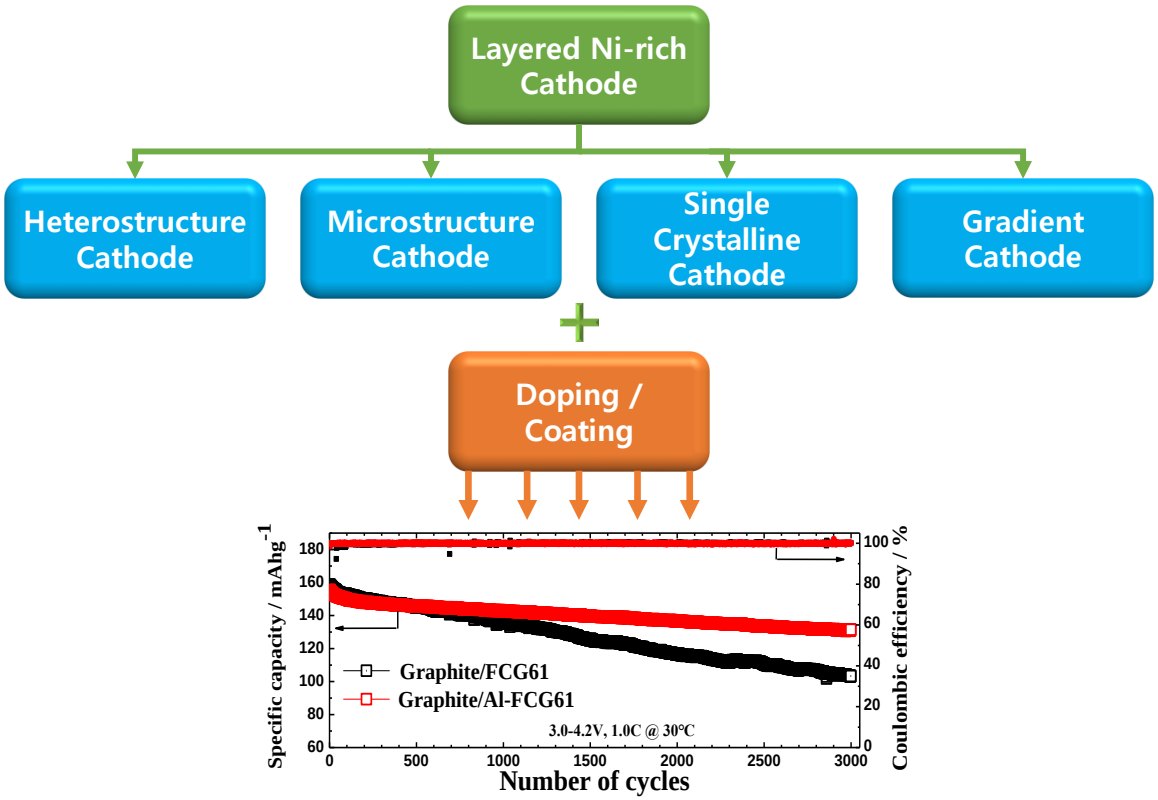

Figure 3.11. Chart outlining the strategies for achieving both stability and high-capacity for layered Ni-rich cathodes which highlight the importance of coupling doping and coating with the discussed prospective strategies. Reproduced with permission from reference 122. Copyright 2016, Wiley-VCH.

In conclusion, the degradation of layered Ni-rich NCM and NCA cathodes is being effectively addressed. Deepened understanding of the materials science of the layered Ni-

rich cathodes provided effective strategies for countering the damage by cracking and electrolyte penetration. Several of these strategies are simple to integrate, at little or no cost, into existing product lines. The tailored cathode materials are already enhancing the competitiveness of EVs by raising the Ni content, without sacrificing cathode stability. In the future, their coupling with doping and surface modifications will further improve their performance (Figure 3.11) as in the case of Al-doped FCG61 ($Li[Ni_{0.6}Co_{0.121}Mn_{0.272}Al_{0.007}]O_2$), which already maintains as much as 84.5 % of its initial capacity after 3000 cycles at 1.0 C cycling, thus meeting the requirement for a daily charge/discharge cycle for 10 years of service.[122] Fine tuning of the compositional gradients, of the microstructures, and of heterostructures along with computation, modeling, and machine learning on these topics and will further improve their performance.

Chapter 4. Nanorod Gradient Cathode: Preventing Electrolyte Penetration into Cathode Particles*

4.1. Introduction

More than two and a half decades have passed since the introduction of $LiCoO_2$ as the first commercial Li-ion battery cathode.[1] Since then, Li-ion batteries (LIBs) have made great progress and become an essential energy storage device in our society. Recently, they have started to be employed as main energy providers in larger applications such as electric vehicles (EVs) and energy storage systems (ESSs) which require higher energy density and longer cycle life. To suit the needs of these complex systems, numerous cathode[1,12,79,142,143] and anode[144–146] materials have been explored. But due to the lower capacity and cycling performance of cathodes compared to anodes, cathodes have been the bottleneck for battery performance.

Amongst the cathode materials, layered transition metal oxides ($LiTMO_2$, TM = transition metals) are seen as strong contenders due to their high gravimetric and volumetric energy densities; $Li[Ni_xCo_yMn_z]O_2$ (NCM)[14,147,148] and $Li[Ni_xCo_yAl_z]O_2$ (NCA)[14,71,149] are already being used in the Chevy Volt, Nissan Leaf, and Tesla Model S and X. Nonetheless, growing demand for higher energy densities calls for even higher practical capacities and the U.S. Department of Energy (DOE) has estimated that to guarantee the success of EVs, a driving range of at least 300 miles,[7] translating to 350 Wh

* **Sun, H.-H.**; Weeks, J. A.; Heller, A.; Mullins, C. B. Nanorod Gradient Cathode: Preventing Electrolyte Penetration into Cathode Particles. *ACS Appl. Energy Mater.* **2019**, *2*, 6002 – 6011. Ho-Hyun Sun carried out the experimental work. Prof. Mullins and Prof. Heller supervised the project. All participated in the discussion and preparation of the manuscript.

kg^{-1} at the cell level and 800 Wh kg^{-1} (216 mAh g^{-1} at 3.7 V) at the cathode active material level, is required. This can be achieved by increasing the Ni concentration in NCM and NCA but is accompanied by a loss in structural and chemical stabilities, especially above 80% Ni content[67,68] as Ni-rich NCM suffers from surface deterioration from the Ni redox reaction to Ni^{2+} [91,113,129,150] and bulk degradation from crack generation caused by the repeated stress during the H2 – H3 phase transition.[16,77,151,152]

Numerous attempts have been made to realize both high capacity and stability of NCM materials through mitigation of the impact of such degradation mechanisms. Transition metal compositions have been varied to identify the most optimal performance composition.[67,68,148] Structural integrity has been improved by doping the particle bulk with Fe, Mg, Al, Zn, Ti, B, Zr, and W.[91,132,139,153–156] Surface chemical stability has been improved by coating with a layer of Al_2O_3, AlF_3, $Al(OH)_3$, ZrO_2, and C nano-layers.[157–161] However, composition variations are inherently limited by the capacity *versus* stability trade-off and both doping and coating processes add inactive materials into the electrode, thereby lowering the energy density. In a different approach, Sun *et al*.[65,86,116,119,122,126] created materials with a concentration gradient in which the Mn-rich surface shields the Ni-rich bulk, to allow both high capacity and stable cycling. More practically, it also uses the same conventional cathode material synthesis process and can readily be integrated into existing cathode manufacturing process. Nevertheless, the Mn-rich shell lowers the total Ni content in the cathode and further necessitates a highly Ni-rich bulk to balance the Ni decrease in the shell. Unfortunately, the increased Ni content bulk acts similarly to

$LiNiO_2$[16,65,91,151] and the intensified H2 → H3 phase transition strains the overall cathode structure.

Recently, the same group has proposed a new degradation mechanism[67] in which i) electrolyte penetrates cathode particles *via* interparticle crack networks reaching the surface and ii) the subsequent formation of a rocksalt impurity phase (NiO) along the cracks greatly increases electrical resistance. These factors are cited as the main source of capacity fade for conventional Ni-rich NCMs. In this paper, we investigate whether the same degradation mechanism holds true for a radially columnar concentration graded nano-rod cathode. Through a systematic comparison of the nano-rod gradient $Li[Ni_{0.81}Co_{0.06}Mn_{.0.13}]O_2$ (hereafter denoted as NRG81) to the prominent constant composition $Li[Ni_{0.82}Co_{0.14}Al_{0.04}]O_2$ (hereafter as CC82) under strenuous conditions of substantially increased total Ni content in both the bulk and nano-rods and raised cut-off voltage of 4.4 V, we explore the factors that distinguish the nano-rod material from conventional cathodes in pouch-type full-cells cycled up to 1000 cycles in its electrochemical performance and electrolyte penetration prevention. A combination of *in-situ* and time-resolved (TR)-XRD, particle cross-section SEM images, and high-resolution TEM (HR-TEM) analysis is used to examine the micro- and nano-structure of the cycled cathodes and their effect on electrolyte penetration prevention into the Ni-rich core. Based on these analyses, we address the need for a stable high-energy ($\geq$ 800 Wh kg^{-1}) density cathode through the nano-rod gradient design from both a micro- and nano-structure perspective.

4.2. Experimental

4.2.1. Synthesis of Nano-rod Gradient $Li[Ni_{0.81}Co_{0.06}Mn_{0.13}]O_2$ Cathode

The nano-rod gradient $Li[Ni_{0.81}Co_{0.06}Mn_{0.13}]O_2$ cathode was synthesized by a hydroxide co-precipitation method as reported in the literature.[116,147] $NiSO_4 \cdot 6H_2O$, $CoSO_4 \cdot 7H_2O$, and $MnSO_4 \cdot 5H_2O$ (95:2:3 molar ratio) was initially fed into a 14 L stirred tank reactor to create a highly Ni-rich core $[Ni_{0.95}Co_{0.02}Mn_{0.03}](OH)_2$. A less Ni-rich solution (Ni:Co:Mn = 0.72:0.08:0.20) was simultaneously pumped into the highly Ni-rich solution tank after a certain period of time to achieve the gradient between the bulk and shell. The resulting hydroxide particles were filtered, washed, and vacuum dried at 110 ºC. Afterwards, the dried hydroxides were mixed with LiOH in a 1:1 molar ratio and calcined at 770 ºC for 10 h under a high-purity oxygen atmosphere. The $Li[Ni_{0.82}Co_{0.14}Al_{0.04}]O_2$ was purchased from EcoPro (Seoul, Republic of Korea).[162]

4.2.2. Cathodes and Electrochemical Testing

The synthesized bulk-shell rod-gradient $Li[Ni_{0.81}Co_{0.06}Mn_{0.13}]O_2$ and EcoPro constant concentration $Li[Ni_{0.82}Co_{0.14}Al_{0.04}]O_2$ powders were mixed with carbon black and polyvinylidene fluoride (PVDF) in a 90:5.5:4.5 wt % ratio in N-methyl-2-pyrrolidone (NMP) and cast onto Al foil. Afterwards, the cast electrodes were vacuum dried at 110 ºC and roll-pressed to result in an active material loading of ~ 6 mg cm^{-2}. Electrodes were punched out and assembled in 2032 coin-type half-cells with Li metal as an anode and 1.2 M $LiPF_6$ in ethylene carbonate (EC):ethyl methyl carbonate (EMC) = 3:7 vol % with 2 wt % vinylene carbonate (VC) as electrolyte. Pouch-type full-cells were assembled for long-term cycling with the bulk-shell rod-gradient $Li[Ni_{0.81}Co_{0.06}Mn_{0.13}]O_2$ and EcoPro

constant concentration $Li[Ni_{0.82}Co_{0.14}Al_{0.04}]O_2$ as cathodes and graphite as an anode. The half-cells were cycled between 2.8 – 4.4 V at 0.5C and 30 ºC and full-cells were cycled between 2.8 – 4.3 V at 1.0 C and 25 ºC.

4.2.3. Instruments and Software

Inductively coupled plasma atomic emission spectroscopy (ICP-AES) (OPIMA8300, PerkinElmer) was used to determine the chemical compositions of the synthesized powders. Powder X-ray diffraction (XRD) (Rint-2000, Rigaku) was employed to measure the crystalline structure of the powders and measured with Cu Kα radiation from $2\theta = 10^o$ – 110^o with a step size of 0.02^o and lattice parameters were obtained by Rietveld refinement employing the Fullprof software package. Particle morphologies were observed using scanning electron microscopy (SEM) (JSM-6340F, JEOL) and cross-sections of the particles were obtained using a focused-ion beam (FIB) (NOVA 200/FEI). *In-situ* XRD (Malvern Panalytical Empyrean, Rigaku) was performed with a modified pouch-type half-cell with a beryllium covered 5.0 mm diameter hole at its center for the X-ray beam path. *In-situ* XRD data was taken every 3.5 min. while the cell was being cycled with a constant current of 18 mA g^{-1}. Time-resolved XRD (TR-XRD) (R-AXIS IV++, Rigaku) was used to analyze the thermal properties of the cathodes using pouch-type half-cells fabricated with bulk-shell rod-gradient $Li[Ni_{0.81}Co_{0.06}Mn_{0.13}]O_2$ and EcoPro constant concentration $Li[Ni_{0.82}Co_{0.14}Al_{0.04}]O_2$ as cathodes and lithium metal as theanode. The half-cells were charged at a C/10 rate to a level corresponding to a composition of $Li_{0.16}[Ni_{0.81}Co_{0.06}Mn_{0.13}]O_2$ and $Li_{0.16}[Ni_{0.82}Co_{0.14}Al_{0.04}]O_2$, under the assumption that all the current passed through was used to extract lithium. The electrically delithiated cathodes

were scraped from the aluminum current collector and sealed completely and mounted on the thermal stage of the TR-XRD system. Confirmation of the transition metal concentrations were confirmed *via* an electron probe microanalyzer (EPMA) (JXA-8100, JEOL). Transmission electron microscopy (TEM) (JEM2010, JEOL) was used to observe the structure damage of the recovered after-cycled electrodes.

4.3. Results and Discussions

4.3.1. Cathode Chemical Composition and Crystal Chemistry

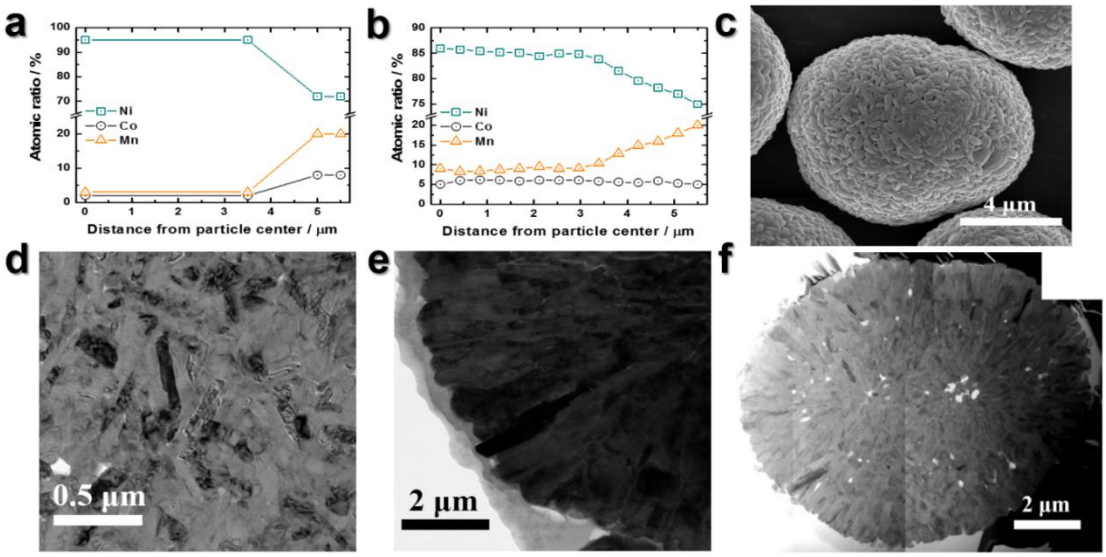

Figure 4.1. NRG81 $Li[Ni_{0.81}Co_{0.06}Mn_{0.13}]O_2$ oxide Ni, Co, and Mn (a) design concentrations, (b) lithiated oxide concentrations, and (c) SEM image of NRG81 cathode particle. TEM image of cross-sectioned NRG81 particle (d) bulk region, (e) graded nano-rod shell region, and (f) whole particle.

Our NRG81 particles were designed (Figure 4.1a) to have an almost pure Ni core (~ 95 % Ni, 2 % Co, 3 % Mn) for high capacity and a Mn-rich surface (~72 % Ni, 8 % Co, 20 % Mn) for cycling stability with a concentration gradient in-between to alleviate anisotropic lattice expansion variations arising from composition differences.[163] The co-

precipitated hydroxide precursor to the NRG81 particles was spherical and had identical transition metal concentrations as originally designed (Figure 4.2a and b). However, under high-temperature calcination conditions, the metal concentrations changed slightly due to atomic inter-diffusion to result in a highly Ni-rich core (~ 86 % Ni, 5.0% Co, 9 % Mn) which graded to a Mn-rich shell (~75 % Ni, 5.0 % Co, 20 % Mn) (Figure 4.1b) to achieve an overall chemical composition of $Li[Ni_{0.81}Co_{0.06}Mn_{0.13}]O_2$ determined by inductively coupled plasma atomic emission spectroscopy (ICP-AES). The constant concentration $Li[Ni_{0.82}Co_{0.14}Al_{0.04}]O_2$ (CC82) was purchased from EcoPro.[162] Both NRG81 and CC82 were spherical with a size of ~ 10 μm and comprised of smaller bulky primary particles (Figure 4.1c and 4.2c). However, unlike the constant concentration CC82, which is comprised of randomly oriented polygonal primary particles as shown previously in the literature,[67] NRG81 is comprised of two distinct regions: the graded nano-rod outer shell and constant concentration core. Like the CC82, the bulk was formed from arbitrarily oriented primary particles (Figure 4.1d), but the graded nano-rod shell region was composed of radially elongated rods (Figure 4.1e). Rietveld refinement of the as-prepared XRD patterns, seen in Figure 4.2d and e, showed that the oxides possessed distinct O3 type α-$NaFeO_2$ layered crystal structures in the $R\bar{3}m$ space group with crystal lattices of a = 2.876(1) Å and c = 14.214(2) Å (R_{wp} = 9.76) for NRG81 and a = 2.865(1) Å and c = 14.181(2) Å (R_{wp} = 8.36) for CC82, matching those of previously reported results.[67] Cation mixing of Li^+/Ni^{2+} for the NRG81 and CC82 were 3.212 % and 2.740 %, respectively.

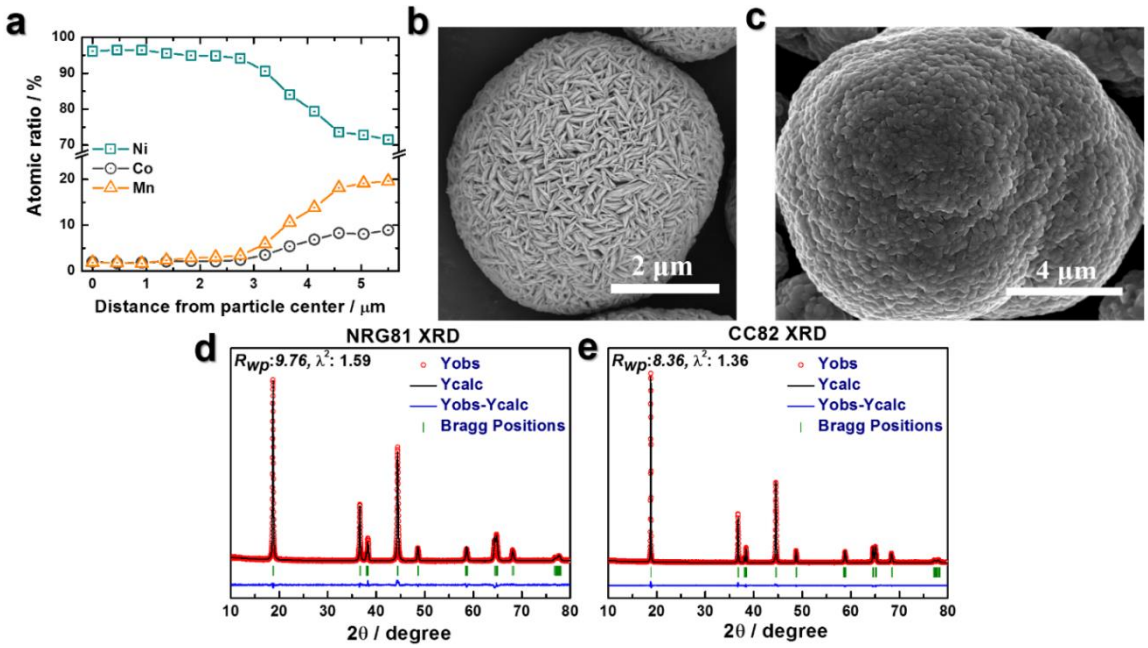

Figure 4.2. Nano-rod gradient $[Ni_{0.81}Co_{0.06}Mn_{0.13}](OH)_2$ hydroxide precursor (a) Ni, Co, and Mn concentrations and (b) particle SEM image. (c) Constant concentration $Li[Ni_{0.82}Co_{0.14}Al_{0.04}]O_2$ SEM image. Rietveld refined XRD patterns of (d) NRG81 oxide and (e) CC82.

4.3.2. Fundamental Electrochemical Performance

Figure 4.3 shows the fundamental electrochemical performance of NRG81 and CC82 half-cells cycled between 2.8 and 4.4 V at 0.5 C (90 mA g^{-1}). During the 1st cycle, NRG81 and CC82 discharged up to 225 mAh g^{-1} and 210 mAh g^{-1} with Coulombic efficiencies of 95.7 % and 92.4 % at 0.1 C, respectively (Figure 4.3a). The NRG81 cathode retained 91 % of its discharge capacity following 100 cycles while the CC82 cathode retained only 79 %. Interestingly, despite having similar nickel compositions and less than half the amount of cobalt, NRG82 exhibited higher discharge capacities at all C-rates, even at the faster rates of 3 C and 5 C (Figure 4.3c). The high capacity is attributed to the the rod-like primary particles in the shell region being radially aligned parallel to Li-containing crystal planes,

which enhances the transport of Li^+.[65,86,122,129] As such, the NRG81 outperforms its constant concentration counterpart and is composed of lower cost materials.

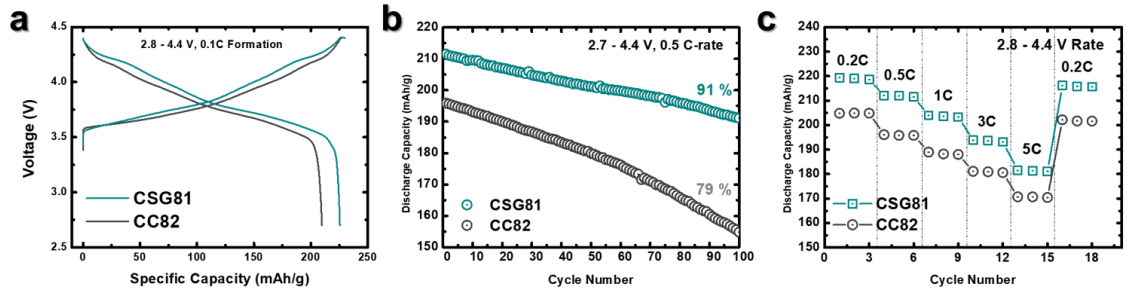

Figure 4.3. Fundamental electrochemical performance of NRG81 vs. CC82 in half-cells: (a) 0.1C first charge-discharge profiles, (b) cycle performance, and (c) rate capability.

4.3.3. Long-term Full-cell Performance

The difference in electrochemical performance of NRG81 and CC82 is further amplified in pouch-type full-cells (cathodes: NRG81 and CC82, anode: graphite) cycled for 1000 cycles as seen in Figure 4.4. As in the case of half-cells, NRG81 delivered a higher first discharge capacity of 195 mAh g^{-1} compared to 188 mAh g^{-1} for CC82 at 1.0 C and 2.8 – 4.3 V. Up to 1000 cycles, NRG81 exhibited stable consecutive discharge capacities to result in a capacity retention of 88.3 %. In contrast, the CC82 discharge capacity started to deteriorate beginning with its 300th cycle to the final 55.9 % retention rate, losing almost half of its original discharge capacity. Correspondingly, the NRG81 full-cell better retained its charge-discharge curves than the CC82 full-cell which suffered from both severe capacity and voltage fade with progressive cycles (Figure 4.4b and c). The significantly higher long-term capacity retention of NRG81 is corroborated by SEM images of cathode particles recovered from the post-mortem full-cells (Figure 4.4d and e) which reveal that NRG81 particles maintain their original morphology and remained intact, whereas CC82

particles completely disintegrate to their individual primary particles. However, just the outward superficial appearance does not fully explain the superior cycling performance of NRG81.

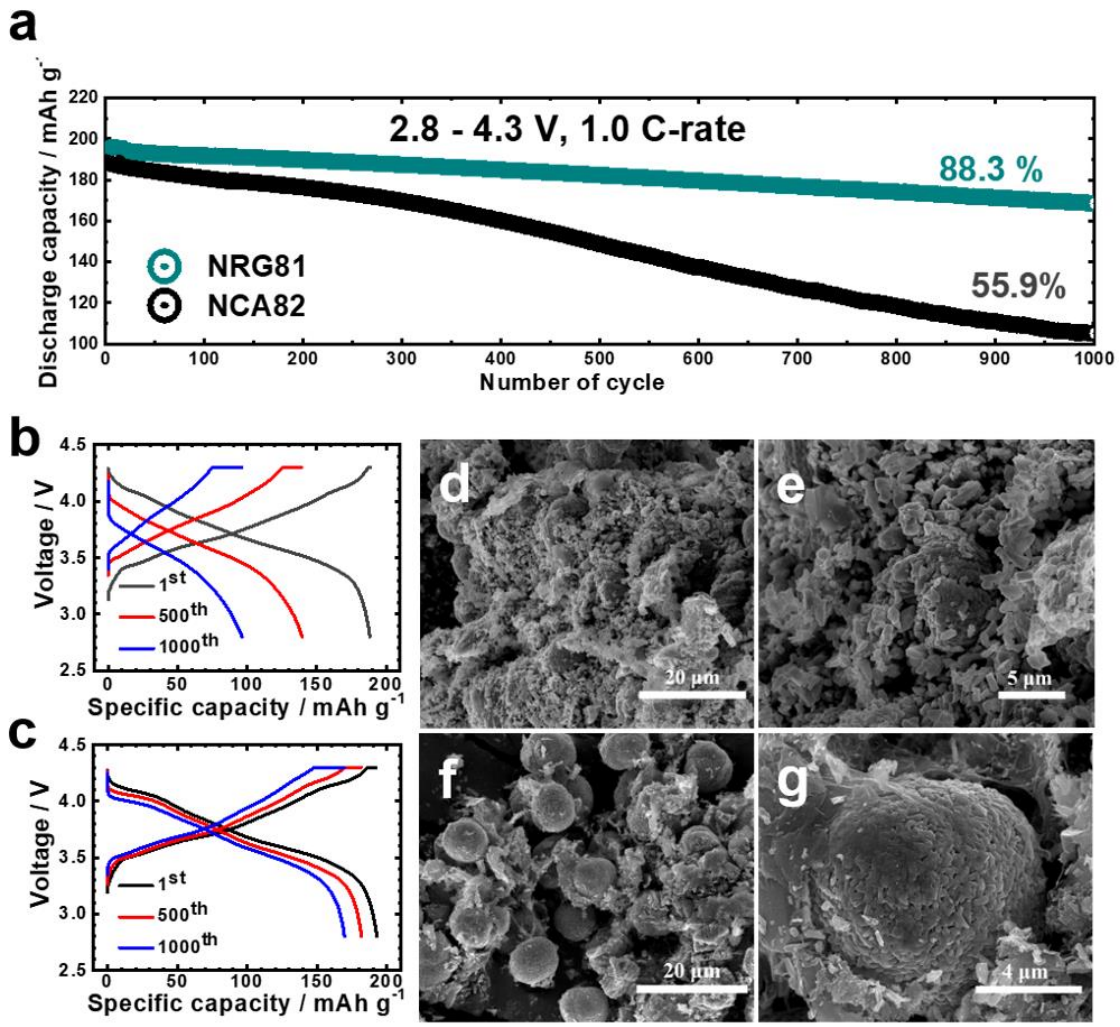

Figure 4.4. Comparison of long-term cycling (1000 cycles) performances of NRG81 vs. CC82 in pouch-type full-cells: (a) 1.0 C-rate cycling performance and corresponding (b) CC82 charge-discharge curves and (c) NRG81 charge-discharge curves. Post-mortem electrode particle SEM images of (d and e) CC82 and (f and g) NRG81.

4.3.4. Micro-structure Cohesion

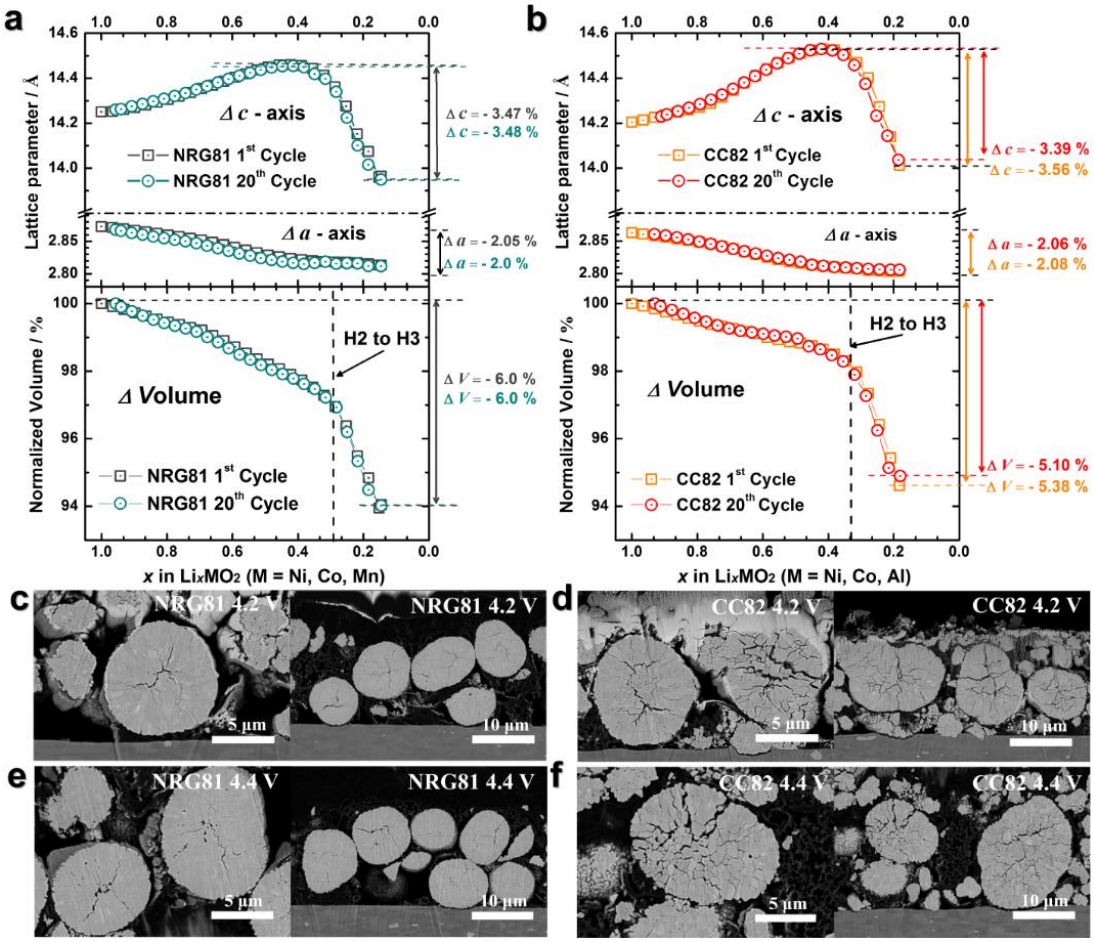

Figure 4.5. *In-situ* XRD Rietveld refined *a*- and *c*-axis lattice and volume parameters of (a) NRG81 and (b) CC82 from 2.8 – 4.4 V. Cross-sectioned SEM images of (c) NRG81 and (d) CC82 at 4.2 V 1st cycle charged state and (e) NRG81 and (f) CC82 at 4.4 V 1st charged state.

Previous reports by Sun *et al*. have referred to the H2 → H3 phase transformation and abrupt volume change,[16,67] accompanied by electrolyte penetration through interparticle cracks, as the major culprit of capacity fade in Ni-rich layered cathodes. To quantitatively ascertain the extent of the H2 → H3 phase transformation, *in-situ* XRD was taken on pouch-type half-cells (cathode: NRG81 and CC82, anode: lithium metal) during

their 1st and 20th charge-discharge at a constant current density of 18 mA g^{-1} up to 4.4 V. From the XRD contour plots, the (110) peak continuously shifts to higher angles, but the (003) peak shifts initially to lower angles and shifts back to higher angles by the end of charging for both NRG81 and CC82. The opposite is true in discharge. Reflecting the XRD peak shifts, the Rietveld refined *a*-axis lattice parameter values of NRG81 and CC82 contract continuously to result in similar parameter changes of Δa = - 2.05 % and Δa = - 2.08 %, respectively, during the 1st charge while the *c*-axis values increase to reach a maximum at ~ 4.0 V (Li_{NRG} = 0.422, Li_{CC} = 0.416) and dramatically decrease to result in Δc = - 3.47 % and Δc = - 3.56 % (Figure 4.5a and b). The resulting volume changes of NRG81 and CC82 during the 1st cycle are ΔV = - 6.0 % for the former and ΔV = - 5.38 % for the latter with significantly an accelerated ΔV occurring after introduction of the H2 → H3 phase transition. Note that the larger ΔV of NRG81 can be attributed to NRG81 extracting more lithium (Li_{NRG} = 0.145, Li_{CC} = 0.183), which in turn results in the nano-rod gradient material delivering the higher discharge capacity shown in Figure 4.3.

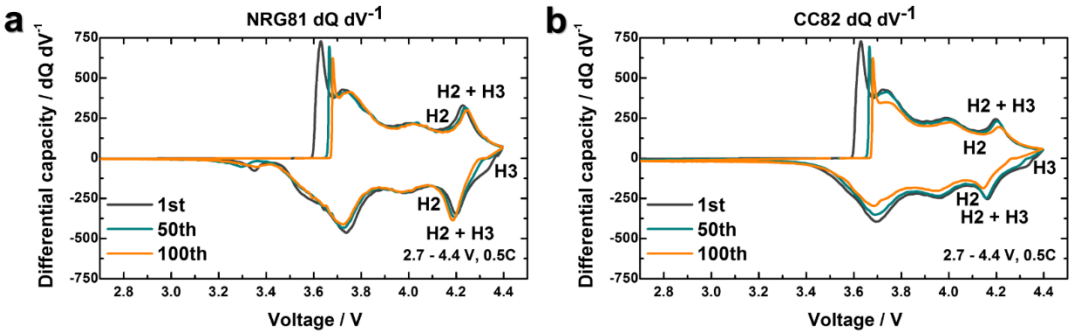

Figure 4.6. 1st, 50th, and 100th dQ dV^{-1} profiles of (a) NRG81 and (b) CC82. The H2 – H3 phase transition is labelled.

Indeed, the abrupt volume change of the H2 → H3 phase transition severely affects the cathode micro-structure. To delineate the impact of the volume change during the H2

→ H3 phase transformation on the cathode micro-structure, cathode particles at 1st cycle charged states of 4.2 V and 4.4 V were cut open with a cross-polisher and observed under SEM (Figure 4.5c – f). The two voltages were chosen because the former is the apex of the H2 → H3 transformation, as indicated by dQ dV^{-1} curves (Figure 4.6), and the latter is the cut-off voltage. As seen in the cross-section SEM images of Figure 4.5, cracks in the micro-structure occurred for both NRG81 and CC82, but whereas they are confined to the bulk in NRG81 with no noticeable differences between 4.2 V and 4.4 V charged NRG81 particles, the cracks propagated in CC82 with exacerbated crack propagation in the 4.4 V charged CC82 electrode. After multiple repeated lattice parameter/volume changes (20th cycle), NRG81 displayed the same parameter and volume changes but CC82 showed considerably decreased changes to Δa = -2.08 %, Δc = -3.39 %, and ΔV = -5.10 % compared to its original Δa = -2.08 %, Δc = -3.56 %, and ΔV = -5.38 % (Figure 4.5a and b). Note that the ~ 5 % irreversible loss of lithium (3.4 % for NRG81 and 7.0 % for CC82) can be ascribed to the surface transformation to cathode electrode interface (CEI) formation.[67,149] It appears that the NRG81 micro-structure, despite its larger ΔV than ΔV of CC82 resulting from more lithium extraction, is able to expand and contract reversibly (same 1st and 20th cycle ΔV) due to the presence of the radially arranged elongated nano-rods in the shell. The radially columnar orientation of the nano-rods allows them to act as buffers to mitigate the stress arising from the highly Ni-rich bulk during the H2 → H3 transition by uniformly dispersing mechanical stress to reduce stress accumulation. Furthermore, the compact packing of the nano-rods confines the cracks to the bulk and suppresses crack propagation from reaching the surface, thus obstructing electrolyte penetration into the reactive Ni-rich

core. Consequently, the H2 – H3 phase transition peak in the NRG81 dQ dV^{-1} profile (Figure 4.6a) appears reversibly with no significant peak diminishment from the 1st to 100th cycle. In contrast, the anisotropic lattice change by randomly oriented polygonal primary particles of CC82 results in irreversible micro-structure damage through stress accumulation and cracking along the grain boundaries and results in gradual weakening of the CC82 dQ dV^{-1} H2 – H3 phase transition peak as seen in Figure 4.6b. The culmination of such repeated anisotropic lattice change after 1000 cycles results in complete disintegration of CC82 secondary particles into individual primary particles, whereas the nano-rod structured NRG81 maintained its particle cohesion as seen in Figure 4.7.

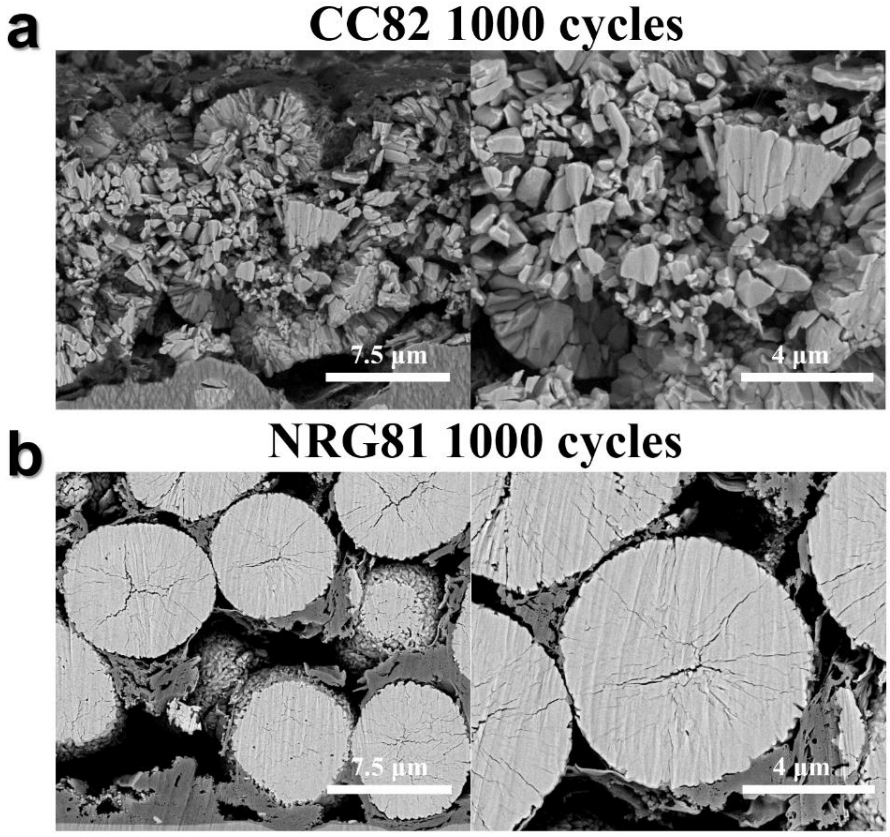

Figure 4.7. Cross-sectioned SEM images of discharged state (a) CC82 and (b) NRG81 after 1000 cycles.

4.3.5. Nano-structure Preservation

To further understand the structural integrity of the nano-rod gradient cathode material, a cross-sectioned particle sample was fabricated from the post-mortem NRG81 full-cell with a focused-ion beam (FIB) and TEM analysis was performed to verify the nano-structure preservation (Figure 4.8). In particular, microcracks in the bulk, which act as channels for electrolyte penetration, and the adjacent areas have been observed with high-resolution TEM (HR-TEM) to check for structural changes. Due to repeated (1000 times) strenuous anisotropic volume expansion/contraction, cracks had developed in the highly Ni-rich core. However, its propagation to the surface was suppressed by the radially elongated rod-shaped primary particles in the shell region. This is important because cracks reaching the surface act as channels for electrolyte infiltration into the highly reactive Ni-rich particle interior,[67] and exposure to infiltrated electrolyte results in rapid structure degradation. One such channel is shown in Figure 4.8b (circled in yellow in Figure 4.8a) and is ~ 3 nm wide. As electrolyte was prevented from passing through the microcrack, the layered-to-rocksalt (NiO) nano-structure phase transformation along the crack boundaries did not occur. Indeed, a selected area electron diffraction (SAED) image of the bulk particles adjacent to the cracks in the inset of Figure 4.8c reflects a distinct layered pattern. Furthermore, the zoomed in HR-TEM image of the circled region in Figure 4.8c, as shown in Figure 4.8d, revealed that the layered structure was well maintained and the Fourier transform images of three regions (Region I, II, and III) near the particle surface in Figure 4.8d clearly exhibit diffraction patterns matching the layered phase of the interior (Region IV). This preservation of the layered nano-structure in the bulk attests to the structural

stability of the NRG81 cathode as the suppression of the interparticle crack propagation by the surface nano-rod structure in the particle outer shell region protected the Ni-rich particle core from electrolyte exposure, thus preventing evolution of the electrically insulating rocksalt phase along the interparticle crack network. Figure 4.8e shows a typical surface structure of the NRG81 cathode after extensive cycling (1000 cycles). Inevitably, a NiO-like rocksalt surface layer developed due to exposure to electrolyte and this is often observed in cycled Ni-rich NCM cathodes and causes an increase in impedance; the slight voltage fade NRG81 experienced, as seen in Figure 4.4c, can also be attributed to electrolyte exposure. Still, even after 1000 cycles, the NiO-like surface layer is limited to 15 - 20 nm in thickness due to positioning of the more chemically stable Mn in the nano-rod particle exterior. In comparison, the CC82 cathode without the nano-rod structure of the NRG81 cathode sustained severe structural and chemical damage which eventually pulverized the cathode and exposed individual primary particles to electrolyte attack. Consequently, as seen in Figure 4.8f and g, whereas the charge transfer resistance (R_{ct}) of NRG81 increased from 29.55 Ω (as-prepared cell) to 133.83 Ω (after 1000 cycles cell), the R_{ct} of CC82 dramatically escalated from 26.6 Ω (as-prepared cell) to 1112.47 Ω (1000 cycles cell). As such, the nano-rod gradient $Li[Ni_{0.81}Co_{0.06}Mn_{0.13}]O_2$ circumvents the degradation mechanism[164] that plagues conventional constant concentration Ni-rich cathodes through its functional nano-rods and testifies to the successful engineering of the NRG81 cathode.

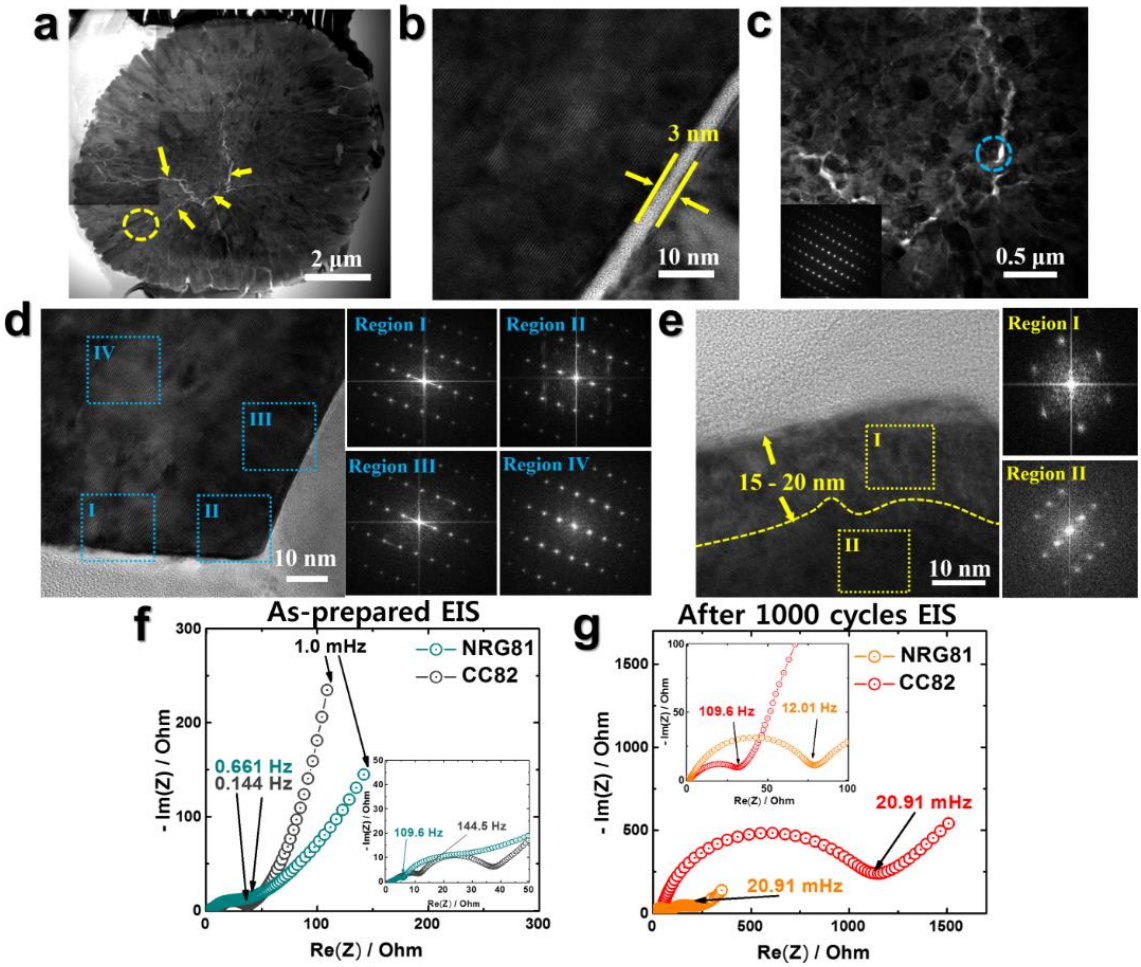

Figure 4.8. (a) Bright-field scanning TEM cross-sectional image of the cycled NRG81 cathode particle after 1000 cycles (yellow arrows indicate cracks in the macro-structure), (b) high-resolution TEM (HR-TEM) image of the circled region in (a) showing the width of a crack, (c) TEM image of the bulk and its corresponding SAED image, (d) particle bulk HR-TEM image of the circled region in (c) and Fourier transform images of the regions I, II, III, and IV, (e) HR-TEM image of particle surface and corresponding Fourier transform images of the regions I and II. EIS curves of (f) as-prepared NRG81 and CC82 and (g) after 1000 cycles.

4.3.6. Thermal Stability

Even under the strenuous conditions of a high-temperature lithium deficient state, where the cathode structure is susceptible to conversion to more stable phases, NRG81 exhibits better thermal micro-structure stability. Figure 4.9 shows a series of time-resolved XRD (TR-XRD) patterns of overcharged NRG81 $Li_{0.16}[Ni_{0.81}Co_{0.06}Mn_{0.13}]O_2$ and CC82 $Li_{0.16}[Ni_{0.82}Co_{0.14}Al_{0.04}]O_2$ measured from 50 °C to 600 °C in the absence of electrolyte. The phase transition from layered ($R\bar{3}m$) to M_3O_4-type (M = transition metal) disordered spinel ($Fd\bar{3}m$) started at 170 °C and 150 °C for NRG81 and CC82 (highlighted in cyan), respectively, as evidenced by a decrease in peak intensity of $(003)_R$ and completed at 200 °C and 180 °C with the merging of the $(108)_R$ and $(110)_R$ peaks.[73,74,165] Concurrently, the $(003)_R/(104)_R$ peak ratio significantly decreased, further suggesting transition metal migration. Note that due to the overcharged layered oxide state, the transition from layered to M_3O_4-type spinel occurred rapidly, showing direct transitions between the two phases without formation of a $LiMn_2O_4$-type spinel.[73,165] With further temperature increase, the spinel phase gradually changed irreversibly into the rocksalt phase ($Fm\bar{3}m$) as indicated by the $(311)_s$ peak intensity decrease. This second phase transition leads to more oxygen release than the first phase transition and is a serious safety concern for LIBs. Yang *et al.*[74] suggested *via in-situ* TEM that the phase transition from layered to spinel to rocksalt propagates gradually from particle exterior to interior and the presence of Mn on the surface suppresses transformation to the rocksalt structure. Likewise, while most of the spinel phase transformed into a rocksalt phase (highlighted in red) by 320 °C for CC82, the NRG81 rocksalt transformation occurred at the considerably delayed temperature of

390 °C due to its concentration graded nano-rods which concentrates Mn in the rod exterior.

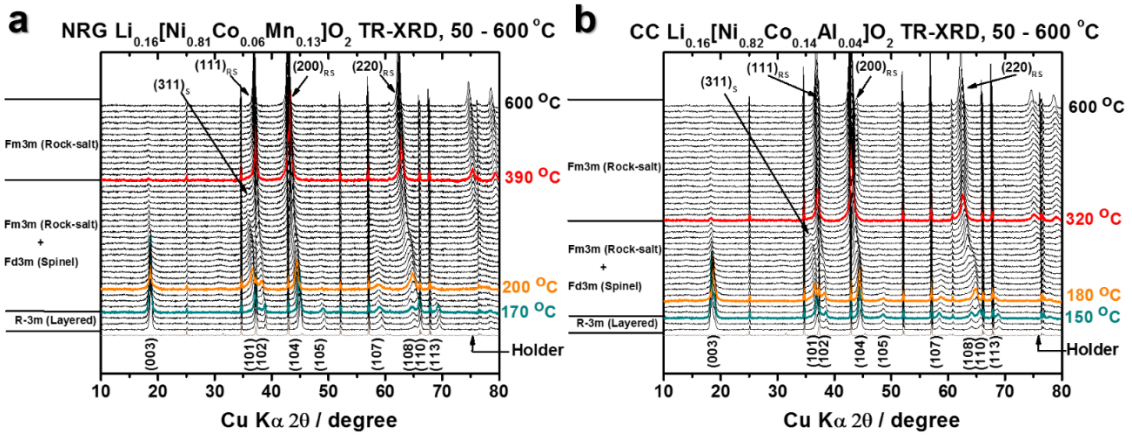

Figure 4.9. Time-resolved XRD patterns of overcharged (a) NRG81 $Li_{0.16}[Ni_{0.81}Co_{0.06}Mn_{0.13}]O_2$ and (b) CC82 $Li_{0.16}[Ni_{0.82}Co_{0.14}Al_{0.04}]O_2$ in the absence of electrolyte. Layered to spinel transition start and finish patterns are colored in cyan and orange, respectively, and spinel to rocksalt pattern is colored in red.

4.4. Summary

In conclusion, a specifically designed, layered cathode material was developed to address the need for a high energy density and cycling performance cathode. The NRG81 material has a highly Ni-rich core and graded columnar nano-rods that are arranged radially and delivers 225 mAh g^{-1} (~830 Wh kg^{-1}) with 91 % capacity retention (100 cycles) in half-cells and 88 % capacity retention (1000 cycles) in full-cells. The high energy density of the NRG81 cathode comes from its highly Ni-rich core, which in turn exacerbates volume change caused by the H2 → H3 phase transition. Fortunately, the radial nano-rods in the particle exterior act as buffers to dissipate the stress arising from the H2 → H3 phase transition and suppress the crack network from propagating to the surface to maintain

particle coherency. This prevents subsequent electrolyte infiltration *via* interparticle cracks and rocksalt impurity phase (NiO) transformation along the crack network as evidenced by HR-TEM image of the cathode particle cross-section. As such, the layered nano-structure in the high capacity but reactive Ni-rich core is preserved, allowing the nano-rod gradient cathode to continuously deliver high specific discharge capacities during long-term cycling.

Chapter 5. Capacity Degradation Mechanism and Cycling Stability Enhancement of AlF_3 Coated Nanorod Gradient $Na[Ni_{0.65}Co_{0.08}Mn_{0.27}]O_2$ Cathode for Sodium-ion Batteries*

5.1. Introduction

With the embracement of electrical energy as a significant energy source, lithium-ion batteries (LIBs) have become prominent as an energy storage device, expanding tremendously from portable electronic devices to larger devices such as vehicles and grid energy storage systems.[166,167] Indeed, the LIB market grew considerably between 1990 to 2013 to a total of $54 billion (U.S.) and is forecasted to accelerate, especially with the spread of electric vehicles.[168] Despite its tremendous expansion, there has been much concern over the possible exhaustion of lithium sources as it's predicted that lithium shortages could occur due to increased demand.[169,170] This is already reflected in lithium prices doubling over the last few years. Additionally, lithium sources are concentrated in only a few geographical locations, making it vulnerable to price fluctuations. Naturally, alternative energy storage sources have been sought after for some time.

Of the potential candidates, room-temperature sodium-ion batteries (SIBs) have received much attention. Sodium is the 6th most abundant element in the earth's crust, which makes it more cost-effective than lithium,[171] and SIB chemistry is like that of the

* **Sun, H.-H.**; Hwang, J.-Y.; Yoon, C. S.; Heller, A.; Mullins, C. B. Capacity Degradation Mechanism and Cycling Stability Enhancement of AlF_3 Coated Nanorod Gradient $Na[Ni_{0.65}Co_{0.08}Mn_{0.27}]O_2$ Cathode for Sodium-ion Batteries. *ACS Nano* **2018**, *12*, 12912 – 12922. Ho-Hyun Sun carried out the experimental work. Prof. Mullins and Prof. Heller supervised the project. All participated in the discussion and preparation of the manuscript.

well-established LIB, which facilitates SIB research.[172] Nonetheless, for SIBs to compete with LIBs, the former need to have comparable electrochemical performance to the latter. To achieve this, various SIB cathodes have been studied, including polyanion structures,[173,174] organic compounds,[175] and P2-type[176–180] and O3-type layered oxides.[181–188] Among the various candidate materials, the layered oxide compounds appear to be most attractive as a promising cathode for SIBs because of their high gravimetric energy density and cycling stability. Recently, P2-type layered oxide materials (Na_xMO_2, $x \approx 0.7$) have garnered much attention due to their high reversible capacities and fascinating crystal structure. But the initial sodium deficiency results in an atypical Coulombic efficiency (≧ 100 %) during the initial formation cycle and hampers full-cell fabrication, ultimately making them impractical.[189] On the other hand, O3-type layered oxides $NaMO_2$ (M: transition metals) possess the same crystal structure and chemistry as the prominent $LiCoO_2$[190] and can still be fabricated into practical full-cells. In particular, spherical co-precipitation synthesized layered O3-type $Na[Ni_xCo_yMn_{1-y}]O_2$ (Na-NCM) has been of interest because of its high tap density[180] and basis in the prominent layered $Li[Ni_xCo_yMn_{1-x-y}]O_2$ (Li-NCM) chemistry, making Na-NCM technology transfer relatively easy.

Based on previous works, increasing the Ni content in Na-NCM has shown to be crucial in fundamentally increasing its energy density in a similar way to Li-NCM chemistry.[185] This is a double-edged sword though as Na-NCM also suffers from accelerated capacity fade with increasing Ni content due to the high reactivity of Ni^{4+} with electrolyte, but with heightened intensity compared to Li-NCM and also at Ni-rich conditions of over 60 % Ni. Additionally, above 4.0 V, O3-type Na-NCM experiences

unwanted electrolyte side-reactions and structural instabilities, further contributing to capacity fade (additional comments on the voltage window are contained in the methods section).[185] In LIBs, a myriad of strategies have been explored to alleviate the detrimental effect of surface degradation on reversible capacity.[113,191–193] Similarly, coating with compounds such as $NaPO_3$, MgO, TiO_2, ZrO_2, and Al_2O_3[194–200] has been a successful strategy in SIBs. Unfortunately, there is a dearth of publications regarding SIB layered cathode surface modifications compared to LIB cathode surface modifications even though cathode surface modification is critical to SIB battery performance. Additionally, many of the processes used in LIB cathodes are not suitable for SIB cathodes as they employ solvents or require an additional calcination treatment which may expose the cathode to moisture or thermal stress.[172,200]

To bypass potentially irreversible damage to the cathode and resolve the reactivity of Ni-rich Na-NCMs, Sun *et al*. developed a dry ball-mill coating process using Al_2O_3, which reacts with electrolyte to form an AlF_3 protective layer, to successfully suppress surface degradation.[200] Another successful approach has been the design of a radially nano-columnar structured cathode with a transition metal concentration gradient to achieve minimized metal redox reactions on the surface for chemical stability.[201,202] Despite such successes, Ni-rich Na-NCM is still relatively unexplored in contrast to its lithium counterpart and a clear understanding of the capacity fading mechanism in Ni-rich Na-NCM is absent at the present. As such, for the development of a realistic SIB, both a high-performance Ni-rich Na-NCM cathode and understanding of the cathode degradation mechanism need to be realized.

In this study, a combination of radially nano-columnar composition gradient design and dry ball-mill coating was used for achieving a synergistically high capacity and stable cycling performance for a Ni-rich Na[$Ni_{0.65}Co_{0.08}Mn_{0.27}$]O2 cathode. The nano-rod gradient Na[$Ni_{0.65}Co_{0.08}Mn_{0.27}$]$O_2$ (NRG65) particle was comprised of a Ni-rich core for high capacity and Mn-rich surface for cycling stability, and presents superior electrochemical performance compared to constant concentration Na[$Ni_{0.65}Co_{0.08}Mn_{0.27}$]$O_2$. To further enhance cycling performance, surface stabilization of the NRG65 was achieved *via* a dry ball-mill coating process using aluminum fluoride (AlF_3) as the coating medium. This approach improves upon the previous Al_2O_3 coating[200] as it circumvents electrolyte side-reaction/decomposition with Al_2O_3 by applying the final AlF_3 product as a protection layer in a simple one-step process to delay active material dissolution. Additionally, AlF_3 is more stable than Al_2O_3 as it has a lower Gibbs free energy of formation[203] and is stable up to 4.5 V and fluorides are also considered to be more resistant to moisture in ambient air than oxides.[103] It is also a tried-and-true coating material in LIB cathodes.[100,193,203,204] As a result, AlF_3 coated NRG65 exhibits a high specific capacity and stable cycling performance in both half-cells and full cells. More importantly, through a systematic analysis of the cycled cathodes, this work highlights the capacity degradation mechanism of O3-type layered Ni-rich Na[$Ni_xCo_yMn_z$]O_2 from electrochemical and structural perspectives, with a focus on high-resolution TEM analysis. In the process, we hope to provide a step forward towards the future development of realistic high energy density SIBs.

5.2. Experimental

5.2.1. Synthesis of Nanorod Gradient $Na[Ni_{0.65}Co_{0.08}Mn_{0.27}]O_2$ Cathodes

For the synthesis of the NRG 65, the $[Ni_{0.65}Co_{0.08}Mn_{0.27}](OH)_2$ precursor was prepared as nano-rod primary particles *via* co-precipitation,[147,202] in which the chemical-composition gradient varied from the inner end to the outer end. $NiSO_4 \cdot 6H_2O$, $CoSO_4 \cdot 7H_2O$, and $MnSO_4 \cdot H_2O$ were used as starting materials for co-precipitation. Two tanks containing two different solutions were used to control the concentrations of the transition metals. An aqueous solution with Ni:Co:Mn ion molar ratio of 0.58:0.10:0.32 (Tank 2) was slowly pumped into a Ni-rich (molar ratio of Ni: Mn = 0.96: 0.04) stock solution (in Tank 1). At the initial stage of the co-precipitation process, Ni-rich aqueous solution (Tank 1) was fed first into the 17 L batch reactor filled with a certain amount of deionized water, NH4OH solution (aq), and NaOH solution (aq.). The solution from tank 1 was mixed continuously with the solution from tank 2 (Ni-deficient solution) and the homogeneously mixed solution was then fed into a batch reactor. Concurrently, a 4.0 mol L^{-1} aqueous NaOH solution and the desired amount of a NH_4OH chelating agent solution (aq.) were separately pumped into the reactor. After the composition of Tank 1 reached the desired surface composition, feeding from Tank 2 was stopped. The concentration of the solution (2 mol L^{-1} for the metal ions), pH (11), temperature (50 °C), and stirring speed of the mixture in the reactor (1000 rpm) were carefully controlled.

5.2.2. Synthesis of Constant Concentration $Na[Ni_{0.65}Co_{0.08}Mn_{0.27}]O_2$ Cathodes

A co-precipitation method was used to synthesize the constant concentration $[Ni_{0.65}Co_{0.08}Mn_{0.27}](OH)_2$ precursors.[147] A homogenously mixed solution of $NiSO_4 \cdot 6H_2O$,

$CoSO_4 \cdot H_2O$, and $MnSO_4 \cdot H_2O$ were supplied into a 17 L batch reactor under a N_2 atmosphere at a reaction temperature of 55 °C. The pH of the solution was kept at 11 and stirring rate was kept at 550 RPM. The resulting hydroxide precursors from the reactor were filtered, washed, and vacuum dried at 110 °C overnight. The final constant concentration $Na[Ni_{0.65}Co_{0.08}Mn_{0.27}]O_2$ cathode was fabricated by mixing the dried hydroxide precursor with NaOH in a 1:1 molar ratio and calcining at 650 ºC for 24 h under an oxygen environment and then quenching in vacuum.

5.2.3. Nano-sized AlF_3 Particle Synthesis

AlF_3 particles were synthesized as reported previously.[100] In a molar ratio of 1:7, $Al(NO_3)_3 \cdot 9H_2O$ (aq) and NH_4F (aq) was mixed together in a solution. The solution pH was adjusted to 10 and the solvent was evaporated. The obtained $(NH_4)_3AlF_6$ powders were heated at 400 °C for 5 hrs under N_2 conditions and the resulting powder was vacuum dried to obtain AlF_3 powders..

5.2.4. Dry Ball-mill Coating

To avoid cathode exposure to moisture, the dry ball-mill coating was performed in a dry room. The AlF_3 coated full-concentration gradient $Na[Ni_{0.65}Co_{0.08}Mn_{0.27}]O_2$ was obtained by placing bare $Na[Ni_{0.65}Co_{0.08}Mn_{0.27}]O_2$ and AlF_3 nanoparticles (Sigma Aldrich, USA) in a polypropylene bottle (Nalgene, USA) with zirconia balls and ball-milling using a ball-mill machine (As one, PM-001, Japan). Coating of the particles was carried out at 100 rpm for 12 h with 1 wt % AlF_3 nanoparticles.

5.2.5. Electrochemical Characterization

The resulting bare and AlF_3 coated sodium metal oxides were mixed with Super-P carbon and polyvinylidene fluoride (PVdF) in a 85:10:5 ratio in *N*-methyl-2-pyrrolidone and cast onto an aluminum foil to achieve active material loading of 2.5 – 3.0 mg cm^{-2} for half-cells and 5.5 – 6 mg cm^{-2} for full-cells. Afterwards, the cast electrodes were vacuum dried and roll-pressed. Half-cell electrodes were punched out from the electrodes and assembled in 2032 coin-type cells with sodium metal as an anode with 0.5 M $NaPF_6$ in propylene carbonate (PC) + fluoroethylene carbonate (FEC) 2 vol. % as electrolyte and cycled from 1.5 – 4.1 V *versus* Na^0/Na^+ at 0.5C. With Ni-rich O3-type cathodes, it is true that higher capacities could be achieved with an increased cut-off voltage. But due to unwanted side-reactions and structural instabilities, the O3-type cathodes are susceptible structural damage, which leads to rapid capacity fading. In the case of SIBs, these problems exacerbate as the stressful Monoclinic P'3 to Hexagonal P3'' phase transition occurring above 4.0 V (vs Na/Na^+) causes the reversibility of Na ions during charge-discharge to fall significantly. In a previous report,[20] reactive Ni^{4+} in high-Ni cathodes ($x \geq 60$ at%) at a highly charged state (upper cut-off potential of 4.1 V) have been reported to cause partial electrolyte decomposition, leading to substantially poorer capacity retention and rate capability compared to cathodes with low Ni content. Therefore, to achieve reasonable cycling performance along with high capacity, we have decided to cycle between the voltage range of 1.5 – 4.1 V. Note that 1 C = 150 mA g^{-1}. Pouch-type full-cells were fabricated with electrode dimensions of 3 by 5 cm^2 area of both bare and AlF_3 coated nano-rod gradient $Na[Ni_{0.65}Co_{0.08}Mn_{0.27}]O_2$ electrodes as the cathode and hard carbon as the

anode (active material : PVdF = 8 :2). The negative electrode to positive electrode (N/P) capacity ratio of the full-cells was 1.15:1 and the fabricated full-cells were cycled from 1.0 – 4.1 V up to 200 cycles at 1C and 25 ºC. Electrochemical impedance spectroscopy (EIS) was performed on after-cycled full-cells which were charged to 4.1 V with a potentiostat (Bio-Logic, VMP3) from 1 MHz to 1 mHz.

5.2.6. Analytical Techniques

The chemical composition of the prepared precursors and oxides were ascertained by inductively coupled plasma atomic emission spectroscopy (ICP-AES, OPIMA8300, PerkinElmer). Powder X-ray diffraction (XRD, Rigaku, Rint-2000) was performed with Cu Kα radiation from 2θ = 10º - 80º with a step size of 0.01ºand the lattice parameters were obtained from the XRD pattern by Rietveld refinement employing the Fullprof software package. Scanning electron microscopy (SEM, JSM-6340F, JEOL) was used to analyze particle before- and after-cycled morphology. Particle cross-sections were obtained with a focused-ion beam (FIB) and an electron probe microanalyzer (EPMA, JXA-8100, JEOL) was used to confirm successful concentration gradient profiles on precursor and sodiated oxides. Transmission electron microscopy (TEM, JEM2010, JEOL) and energy dispersive X-ray spectroscopy (EDX, JEM 20100F, JEOL) were carried out on the cross-sectioned samples. HF titration was performed with a 5-ml glass burette using a 0.02 N sodium hydroxide (NaOH) aqueous solution. The pH indicator was bromothymol blue (0.04 wt % in water), which appears yellow at pH less than 6 and blue at pH greater than 7. A polypropylene syringe and Erlenmeyer flask were used to prevent possible reaction of glass with HF acid. Titration was performed by placing 3 mL of crushed ice and 1 mL of water

in the polypropylene Erlenmeyer flask with a couple drops of bromothylmol blue. 0.2 mL of electrolyte was drawn from pristine electrolyte, cycled bare NRG65 pouch-cells, and cycled AlF_3-NRG65 pouch-cells and weighed and added to the Erlenmeyer flask. The flask was swirled and NaOH solution was added to the solution until the yellow colored solution turned to blue. If the color returned to yellow after 30 seconds, more NaOH drops were added. The weight of the empty syringe was taken to determine electrolyte weight and HF levels were calculated under the assumption that acids were pure HF.

5.3. Results and Discussions

5.3.1. Cathode Particle Morphology and Characterization

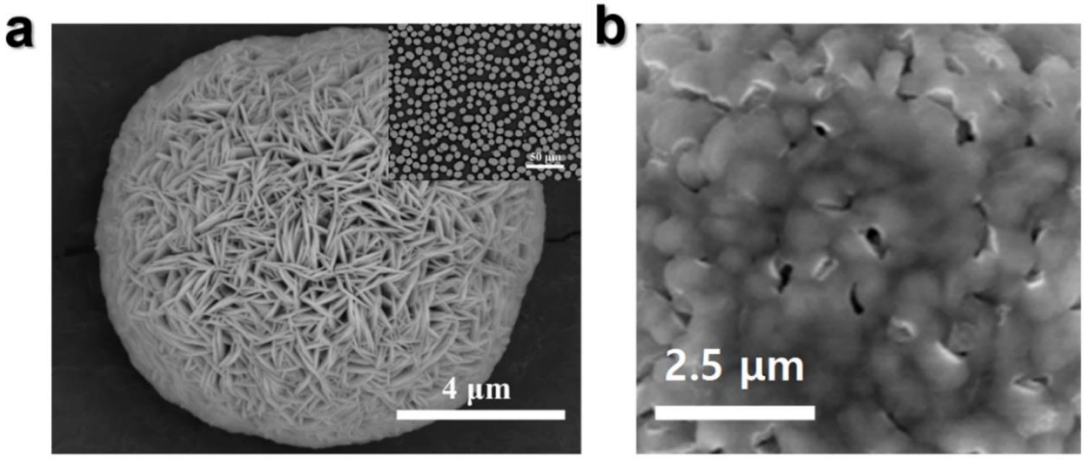

Figure 5.1. (a) Nano-rod gradient $[Ni_{0.65}Co_{0.08}Mn_{0.27}](OH)_2$ precursor particle SEM image and (b) close-up Nano-rod gradient $Na[Ni_{0.65}Co_{0.08}Mn_{0.27}]O_2$ particle SEM image.

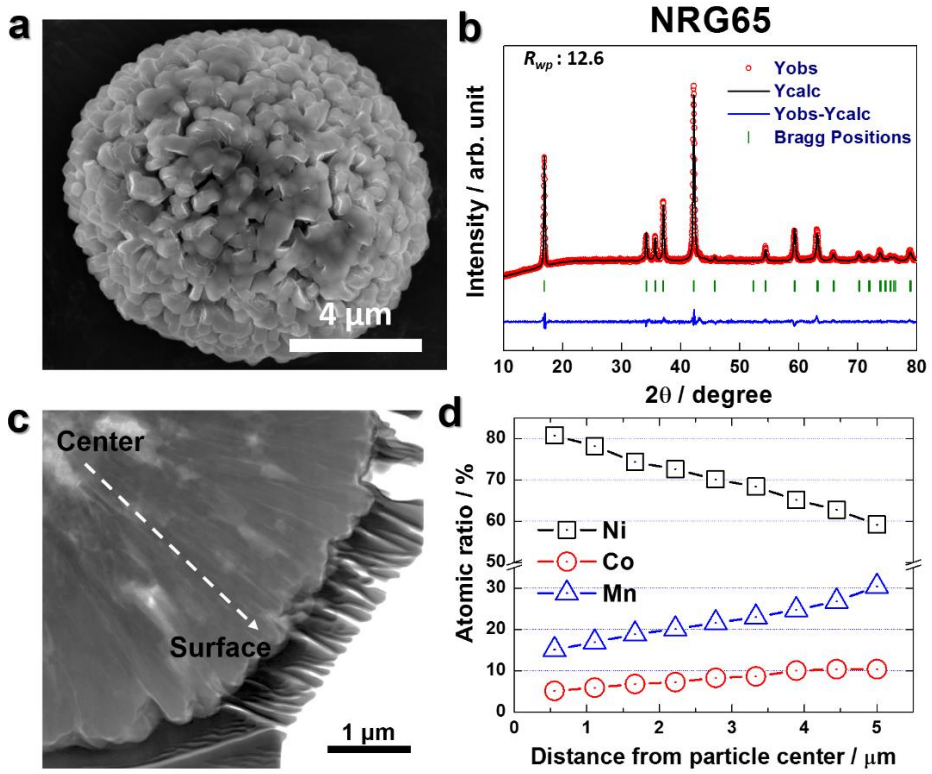

Figure 5.2. (a) SEM image, (b) Rietveld refined XRD pattern, (c) cross-sectioned TEM image, and (d) EPMA data of as-synthesized nano-rod gradient $Na[Ni_{0.65}Co_{0.08}Mn_{0.27}]O_2$.

A scanning electron microscopy (SEM) image of the $[Ni_{0.65}Co_{0.08}Mn_{0.27}](OH)_2$ precursor is shown in Figure 5.1a. Here we refer to "secondary particles" as the individual spherical cathode particles which have a uniform size distribution of 8 – 10 µm in diameter (tap density of ~ 2.00 g cc^{-1}) and are composed of smaller needle-like nano-scale structures in a radial configuration which we refer to as "primary particles." Thermally sodiated bare (no AlF_3 coating) nano-rod gradient $Na[Ni_{0.65}Co_{0.08}Mn_{0.27}]O_2$ (NRG65) particles retain their uniform spherical morphology but the primary particles became bulkier due to sintering (Figure 5.2a and 5.1b). The X-ray diffraction (XRD) pattern and Rietveld refinement of the oxide (Figure 1b) reveaed that the sodiated cathodes had a well-ordered

O3-phase with a $R\bar{3}m$ space group and lattice parameters of a = 2.945 (1) Å and c = 15.756 (2) Å ($\underline{R_{wp}}$ = 12.6).[181,205,206] The proposed NRG cathode design was based on the physiochemical feature shown previously by gradient materials:[116,119] The Ni-rich center delivers a high discharge capacity and the Mn-rich surface minimizes surface reactivity while the linear transition metal concentration variation throughout engenders columnar nano-rods to minimize anisotropic volume changes from composition differences. An electron probe micro-analyzer (EPMA) (Figure 5.2d) was used to study the transition metal compositions of the as-synthesized NRG65 to verify the presence of a concentration gradient from particle center to surface to ensure successful nano-rod gradient synthesis. The $Na[Ni_{0.65}Co_{0.08}Mn_{0.27}]O_2$ had transition metal concentrations of 81 at% Ni, 5 at% Co, and 14 at% Mn in the core and 59 at% Ni, 10 at% Co, and 31 at% Mn on the surface and composition gradients in-between.[122] Finally, a TEM image of a cross-sectioned nano-rod gradient oxide particle (Figure 5.2c) reveals that NRG65 was comprised of compactly packed nano-rods that spanned from the center to the surface, confirming that NRG65 was synthesized successfully.[201] Overall (volume averaged) transition metal compositions were determined by inductively coupled plasma atomic emission spectroscopy (ICP-AES).

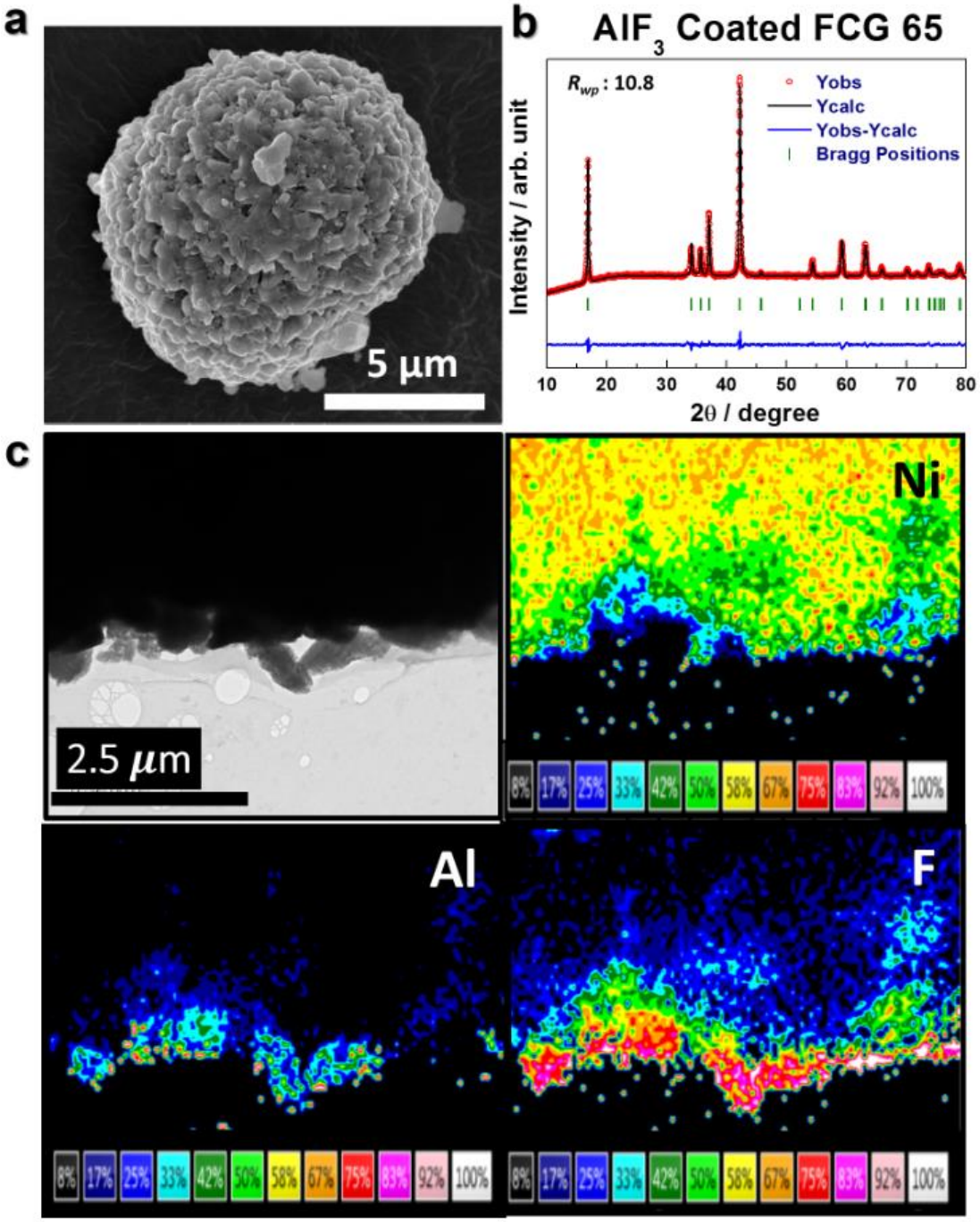

Figure 5.3. AlF_3 coated NRG65 (a) particle SEM image, (b) Rietveld refined XRD pattern, and (c) TEM-EDX quantitative elemental mapping of Ni, Al, and F concentrations near particle surface. Note that the colors indicate the concentration intensity of Ni, Al, and F as indicated by the concentration % shown at the bottom of each images.

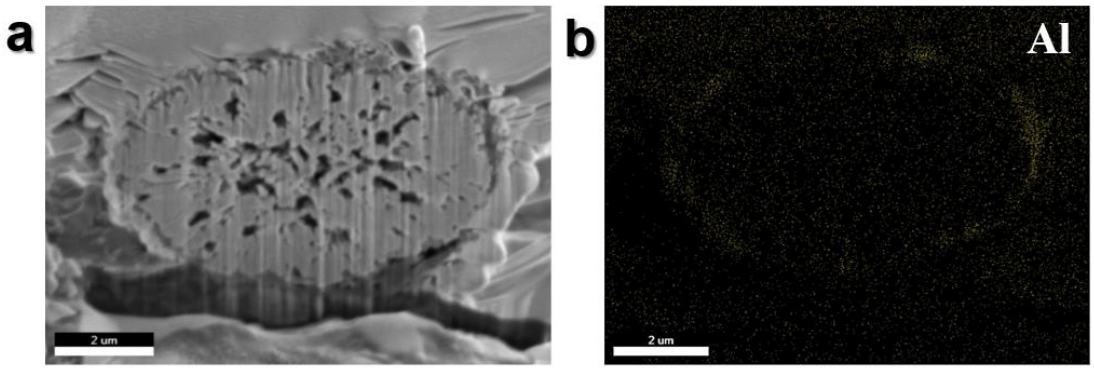

Figure 5.4. Nano-rod gradient $Na[Ni_{0.65}Co_{0.08}Mn_{0.27}]O_2$ particle cross-section (a) SEM image and (b) corresponding aluminum energy dispersive X-ray spectroscopy. Note that in the EDX Al mapping image of (b) is in the same position as in panel (a) and indicates the presence of Al in the coating on the particle. However, as the coating is 1 wt % AlF_3 coating, Al signals may appear to be faint and the reader should look very carefully.

AlF_3-coated nano-rod gradient $Na[Ni_{0.65}Co_{0.08}Mn_{0.27}]O_2$ (AlF_3-NRG65) particles were obtained *via* dry ball-mill coating with AlF_3 nano-particles as shown in Figure 5.3a. As the figure shows, the AlF_3 coating did not alter the spherical morphology of the original particle but the coating filled the pores that are present in bare NRG65 and roughened the particle surface. The XRD pattern of the coated oxide (Figure 5.3b) showed almost the same lattice parameters as bare particle (a = 2.943 (1) Å and c = 15.772 (2) Å R_{wp}= 10.8).[181,205,206] SEM-EDX of AlF_3-NRG65 particle cross-section as displayed in Figure 5.4 shows that Al signals were detected from the particle surface and that the coating was non-uniform with thicknesses varying from 50 nm thin to 300 nm thick. It should be noted that while a thick coating layer is not beneficial for some aspects regarding cathode performance, due to sodium-based oxide layers being so reactive with electrolyte and moisture, a 200 nm thick coating layer still efficaciously protects the O3-type layered

cathode from electrolyte attack and other coating works also have thicknesses of ~ 100 nm and show significantly improved performance.[200] Quantitative elemental mapping by energy dispersive X-ray spectroscopy (EDX) (Figure 5.3c) also revealed that the outer surface signals consisted of Al and F in an approximately 1:3 ratio, like the molar ratio of AlF_3. Additionally, Ni signals are stronger in the bulk than the surface, providing further evidence of the compositional gradient. As such, it was affirmed that the desired concentration gradient of Ni, Co, and Mn throughout the entire cathode particle was achieved with a nickel-rich core for high capacity and a manganese-rich surface for cycling stability in a columnar nano-rod structure[201] and that the coating was indeed AlF_3 for surface protection from acidic species such as HF.

5.3.2. Half-cell Electrochemical Performance

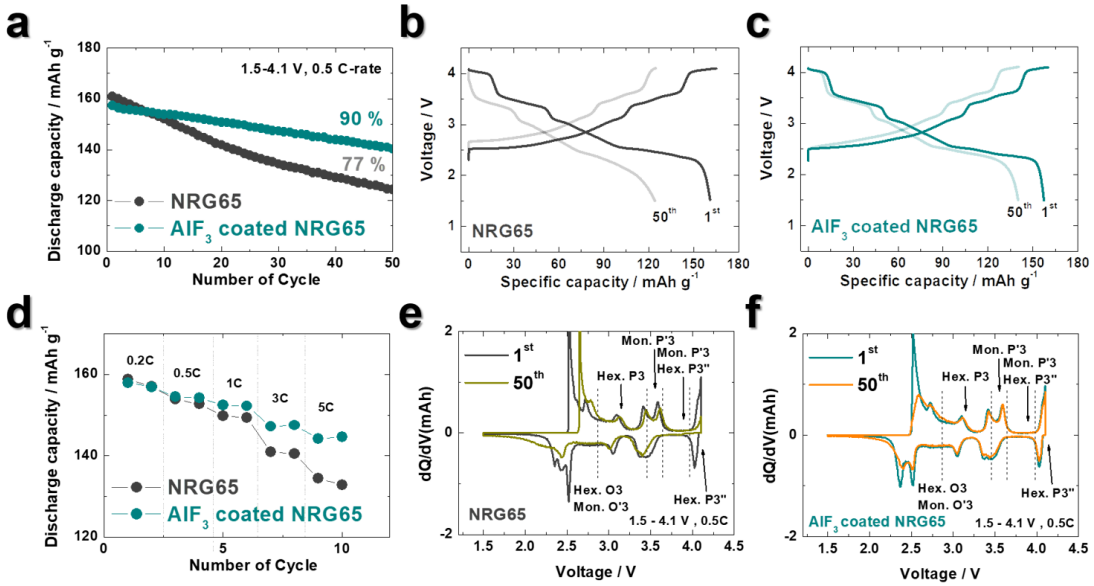

Figure 5.5. Comparison of electrochemical performances between bare NRG65 and AlF_3-NRG65 in half-cell: (a) cycling performance and corresponding charge-discharge curves at 1st and 50th of (b) bare NRG65 and (c) AlF_3 coated NRG65. (d) Rate capability. dQ dV^{-1} profiles of 1st and 50th (e) bare NRG65 and (f) AlF_3 coated NRG65.

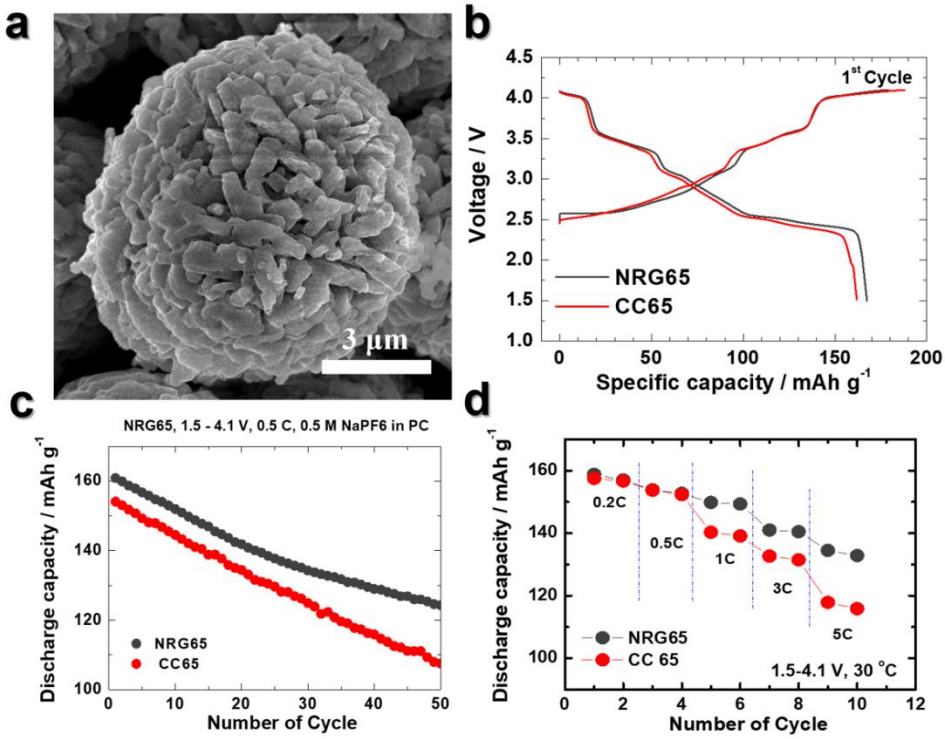

Figure 5.6. (a) SEM image of constant concentration $Na[Ni_{0.65}Co_{0.08}Mn_{0.27}]O_2$ and (b) 1st cycle charge-discharge curves and (c) cycle performance of constant concentration, and (d) rate capability performance of $Na[Ni_{0.65}Co_{0.08}Mn_{0.27}]O_2$ vs. bare nano-rod gradient $Na[Ni_{0.65}Co_{0.08}Mn_{0.27}]O_2$.

The effect of the synthesized nano-rod gradient $Na[Ni_{0.65}Co_{0.08}Mn_{0.27}]O_2$ particle is evident in its electrochemical performance (Figure 5.5a – d). For comparison, we synthesized a constant (uniform) concentration $Na[Ni_{0.65}Co_{0.08}Mn_{0.27}]O_2$ (CC65) particle, as shown in Figure 5.6a, and compared the electrochemical performances. When cycled from 1.5 to 4.1 V at 0.5 C (Figure 5.6b – d), the bare NRG65 cell exhibited much better electrochemical performance than that of CC65 of identical average chemical composition; NRG65 had a discharge capacity of 168 mAh g^{-1} and capacity retention of 77 % while CC65 had a discharge capacity of 161 mAh g^{-1} and capacity retention of 64 % with the

former outperforming the latter also in rate capability performance, especially at high C-rates above 1C.[201,202] It is worth noting that the CC65 charging curve dragged on above 4.0 V and its charging capacity was much higher than discharging capacity, pointing to undesired side-reactions caused by unstable Ni^{4+} on the surface, which is less prevalent in NRG65. Note that such reactions result in electrolyte decomposition and subsequent evolution of gaseous products such as CO_2. The superior performance of the nano-rod gradient cathode material is derived from its compositional variation which exploits the Ni^{3+}/Ni^{4+} redox reaction having a lower energy level than Ni^{2+}/Ni^{3+}, as suggested by Delmas *et al.*[207] In the nano-rod gradient oxide, the Ni-rich center is dominated by Ni^{3+}/Ni^{4+} redox reactions while the Mn-rich surface is dominated by Ni^{2+}/Ni^{3+} redox reactions, explaining why the NRG65 material simultaneously yields more capacity while achieving higher cycling stability compared to CC65 of identical average composition. Despite such merits, the capacity fade of the NRG65 material occurs too rapidly to be considered as a practical SIB cathode and needs improvement.

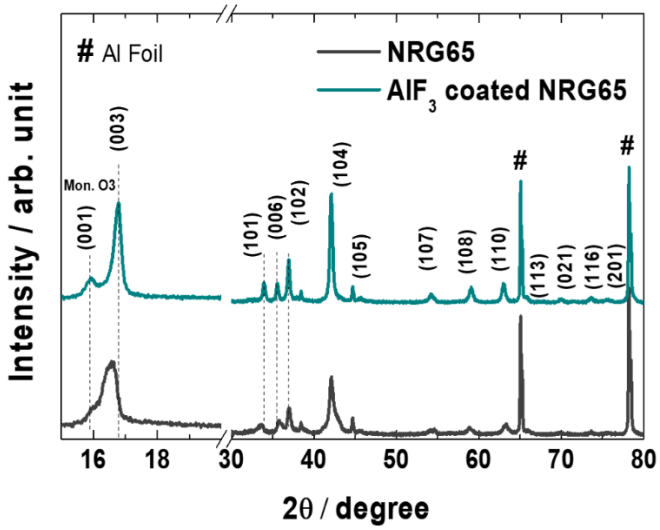

Figure 5.7. After-cycled half-cell XRD patterns of bare NRG65 and AlF_3 coated NRG65.

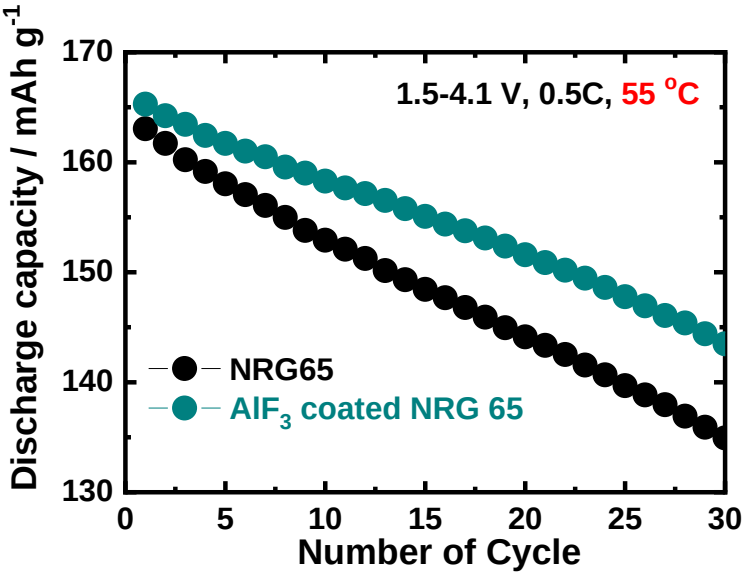

Figure 5.8. High temperature electrochemical cycling performance of bare NRG6 and AlF_3 coated NRG65.

In order to further improve the electrochemical performance, a coating of AlF_3 was applied to the NRG65 surface. With a layer of AlF_3, the AlF_3-NRG65 cell delivered a 161 mAh g^{-1} first-discharge capacity but retained 90 % of its initial discharge capacity (after 50 cycles), which was significantly higher than the bare NRG65 retention rate (Figure 5.5a). Moreover, both cells showed similar 1st charge-discharge voltage profiles, but the AlF_3-NRG65 cell better maintained a charge-discharge profile similar to its first as seen in Figure 5.5b and c; this is reflected in the 1st and 50th cycle dQ dV^{-1} curves of the two cells (Figure 5.5e and f) which exhibited transition redox peaks correlating to distinct phase transitions where AlF_3-NRG65 better maintained its redox peaks. In particular, the peak from 4.0 – 4.1 V, which indicates a Ni redox reaction,[180,185] disappeared by the 50th cycle in NRG65 whereas this peak remained unchanged in AlF_3-NRG65 due to the coating layer preventing surface degradation. Note that the arrows indicate the structural phases that are present at

the peaks and dash lines indicate the borders in-between. Likewise, after-cycled XRD patterns of bare NRG65 and AlF_3-NRG65 demonstrated that the AlF_3 treated material better preserved its structure as the former lost many of its original XRD peaks between 30 – 40º and possessed a broadened $(003)_{hex}$ peak which also shifted and merged with the monoclinic O3 (001) peak (Figure 5.7). On the other hand, even though the after-cycled AlF_3-NRG65 electrode showed a monoclinic O3 (001) peak corresponding to 10 % Na extraction,[187] it retained its original peaks with minimized peak broadening or weakening. At an elevated temperature of 55 °C (Figure 5.8), both bare and AlF_3 coated NRG65 showed increased discharge capacities of 163 mAh g^{-1} and 166 mAh g^{-1}, respectively, with the latter showing better capacity retention at the end of the 30th cycle. Not surprisingly, the AlF_3-NRG65 exhibited outstanding rate capability at the faster rates of 3C (450 mA g^{-1}) and 5C (750 mA g^{-1}), where it delivered high discharge capacities of 147 mAh g^{-1} (92.1 % of 0.2C) and 145 mAh g^{-1} (90.2 % of 0.2C), respectively. It should be noted that NRG65 still exhibited better rate capabilities than the CC (constant composition) materials reported previously[185] due to the elongated nano-rods providing for more rapid Na^+ transport through their entire volume.

5.3.3. Pouch-type Full-cell Electrochemical Performance

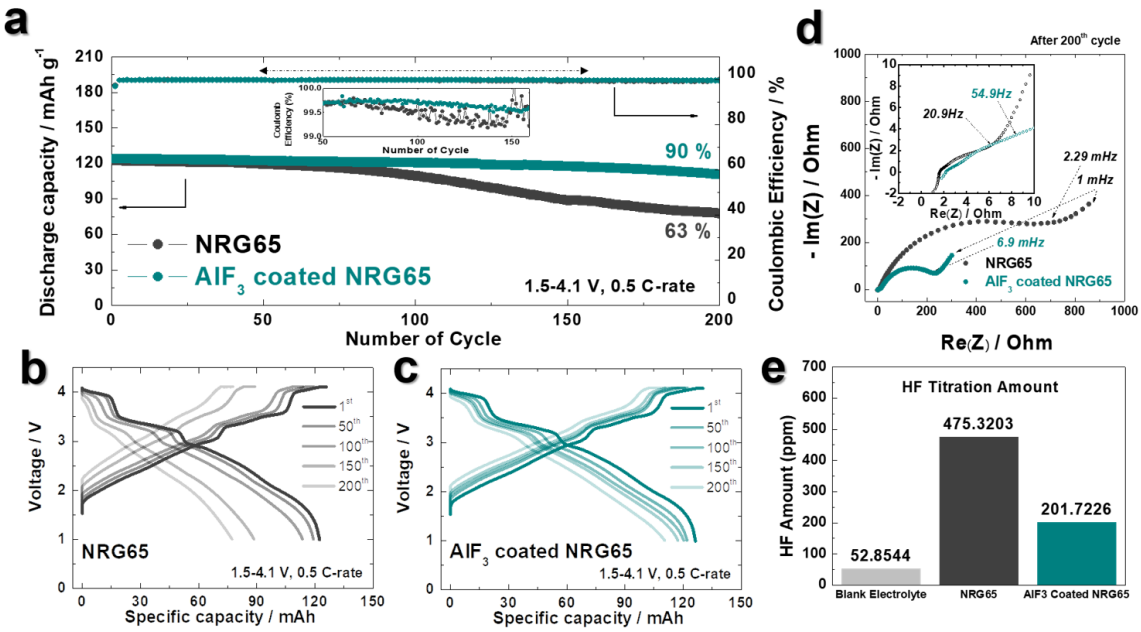

Figure 5.9. Comparison of electrochemical performances between bare NRG65 and AlF_3-NRG65 in full-cells: (a) cycling performance and efficiencies and corresponding charge-discharge curves from 1st to 200th cycle at 0.5 C-rate of (b) bare NRG65 and (c) AlF_3-NRG65. (d) Electrochemical impedance spectroscopy results at 200th cycle at 0.5 C-rate. (e) HF titration test result.

The impact of the AlF_3 surface coating treatment on the nano-rod gradient $Na[Ni_{0.65}Co_{0.08}Mn_{0.27}]O_2$ particles can be seen more clearly in practical pouch-type full-cells (cathodes: bare NRG65 and AlF_3-NRG65, anode: hard carbon) as seen in Figure 5.9. The bare NRG65 and AlF_3 coated NRG65 full-cells both delivered similar first-cycle discharge capacities of 130 mAh g^{-1} and 132 mAh g^{-1}. Nevertheless, due to the AlF_3 coating layer shielding the cathode from irreversible damage, the capacity retention of the AlF_3-NRG65 was 90 % at 0.5C after 200 cycles and possessed a stable Coulombic efficiency throughout cycling. In contrast, the bare NRG65 full-cell cycle stability and Coulombic

efficiency started to falter after the 50th cycle (as seen in the magnified inset of Figure 5.9a showing the Coulombic Efficiency) due to exposed active materials reacting with electrolyte and deteriorating to a capacity retention of 63 %. Correspondingly, the cell with the AlF_3 surface treated material better retained its charge-discharge character compared to the cell with untreated material which suffered from capacity and voltage fade with progressive cycles (Figure 5.9c and d). Nyquist plots of the electrochemical impedance (Figure 5.9b) corroborate said cell performance as by the 200th cycle, the charge-transfer (R_{ct}) resistance of the surface modified cell was 225.0 Ω, significantly lower than the 753.8 Ω of the bare cell. Additionally, an HF titration test revealed that the amount of HF (ppm) detected in the bare NRG65 electrode was more than twice that of the AlF_3-NRG65 electrode.

5.3.4. Post-mortem Particle Cross-sectional Analysis

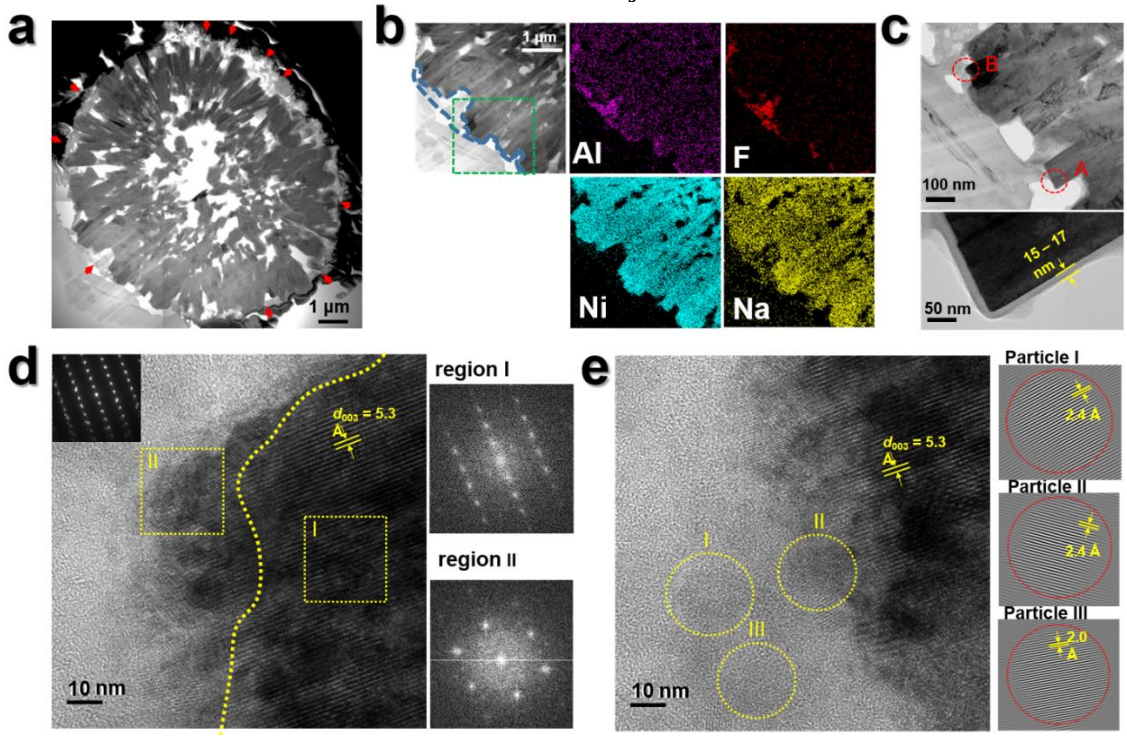

Figure 5.10. (a) bright-field scanning TEM cross-sectional image of the cycled AlF_3-NRG65 cathode particle after 200 cycles (red arrows indicate the AlF3 coating remaining intact after cycling), (b) EDS elemental mapping of the cycled AlF_3-NRG65 cathode particle, (c) bright-field TEM image of the cycled AlF_3-NRG65 cathode marked by green dashed box in Figure (b) (the figure below shows the magnified image of the area marked A), (d) high-resolution TEM image of the region marked B in (c) and Fourier transform images of the regions I and II, (e) high-resolution TEM image showing the crystalline secondary phases observed within the AlF3 coating layer and Fourier filtered images of the marked secondary phases.

To investigate the promising electrochemical performance of the AlF_3-NRG65 particles, cross-sectional TEM samples from the cycled electrodes of the full-cells were fabricated using a focused ion beam. The dark-field scanning TEM image of the cycled AlF_3-NRG65 particle in Figure 5.10 shows that the AlF_3 coating layer (marked by red

arrows) remained intact around the periphery of the secondary particle. The AlF_3 coating was as thick as 1 μm at some places even after 200 cycles. Judging by the before-cycling coating thickness estimated from the EDS mapping in Figure 5.3, the AlF_3 coating was hardly damaged and incurred no significant materials loss during cycling. The EDS mapping of Al, F, Ni, and Na in Figure 5.10b confirms the presence of the AlF_3 coating layer (marked by blue dashed lines) filling in the valley between the two protruding primary particles when the Ni and Al (or F) elemental maps are compared. In addition to Al, a strong Na signal was detected in the coating layer, suggesting that Na reacted with the AlF_3 to form new compounds in the coating that improved the cycling stability. Figure 5.10c shows a bright-field TEM image of the surface region of the cycled AlF_3-NRG65 cathode particle marked by a green dashed box of Figure 5.10b and the accompanying magnified image of area "A" indicates that the even the surfaces that appeared uncoated were encapsulated by a thin layer (~ 10 nm in thickness) such that the AlF_3 coating extended all the around the secondary particle and effectively protected the cathode surface. A high-resolution TEM image along the 100 zone axis of a primary particle (Figure 5.10d) of the area marked by B in Figure 5.10c affirmed retention of the original structure in the particle interior which was capped by a thin layer of NiO-like rocksalt structure. The thickness of the surface rocksalt layer was limited to 10 – 30 nm. Fourier-transform images of the regions I and II in the dotted red boxes clearly distinguishes the two distinct structures. The Fourier transform of the particle interior reproduced the SAED pattern shown in the inset of Figure 5.10d whereas some of the diffraction spots became extinct in the Fourier transform of the surface region due to the disordering of the cations in the

rocksalt structure. Despite a thin layer of partially collapsed structure at the very edge, the layered structure just inside the particle periphery and further in the interior is preserved, which explains the improved cycling stability and the superior rate of the AlF_3-NRG65 cathode. In addition to the surface rocksalt layer, isolated secondary crystalline phases were observed near the vicinity of the cycled cathode surface (Figure 5.10e). The crystalline phases in the surrounding AlF3 coating layer are marked in Figure 5.10e. The accompanying Fourier filtered images of the marked regions verify the presence of a crystalline phase and the estimated distances between the lattice fringes were 2.0 Å and 2.4 Å. Surveying the XRD database, possible compounds containing any combination of Na, Al, F, and O (and with strong peaks at 2.0 Å and/or 2.4 Å) are NaF ($Fm\bar{3}m$, a = 4.62 Å)[208] and $Na_5Al_3F_{14}$ ($P4/mnc$, a = 7.014 Å and c = 10.402 Å).[209] Since the EDS mapping revealed a significant presence of Na in the cycled coating layer, it is likely that AlF_3 reacted with Na to form such compounds. These compounds near the cathode surface may have stabilized the interface chemistry (protection from HF attack and prevention of Ni^{4+} oxidation) and lowered the interface charge transfer resistance by assisting Na^+ conductivity in a similar way that lithium containing compounds reduce ion resistance to improve electrochemical performance.[103,210,211]

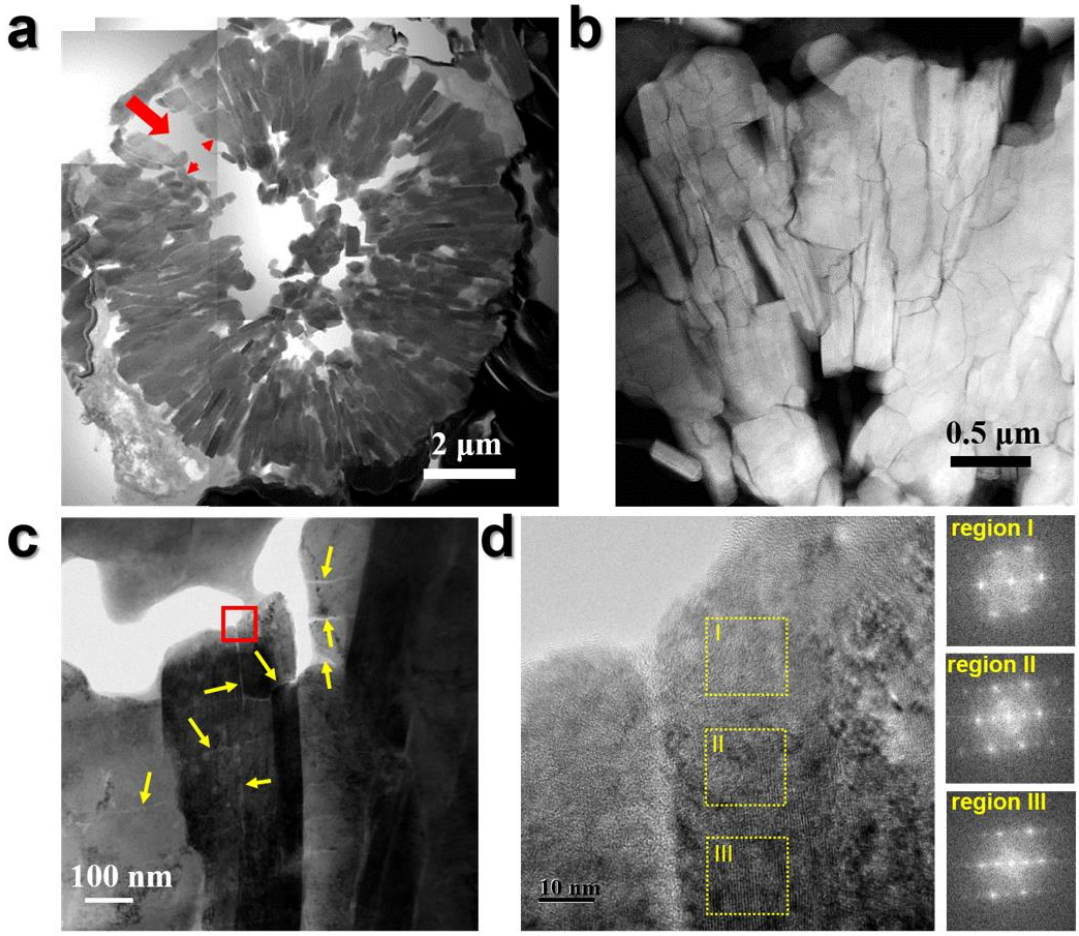

Figure 5.11. (a) bright-field scanning TEM cross-sectional image of the cycled bare NRG65 cathode particle after 200 cycles (red arrows indicate a major crack in the secondary particle that allows infiltration of the electrolyte into the particle interior), (b) dark-field scanning TEM image of the cycled bare NRG65 cathode, showing numerous intra-particle cracks, (c) bright-field TEM image of the cycled bare NRG65cathode with the yellow arrows indicating the intra-particle microcracks, (d) high-resolution TEM image of the red box marked region in (c) and Fourier transform images of regions I, II, and II demonstrating the extensive transition to the rocksalt structure at the surface of the cycled bare NRG65cathode.

As shown in Figure 5.11a, the cycled bare NRG65 cathode particle contained a large crack that nearly fractured the secondary particle due to stress from repeated Na

intercalation/de-intercalation and the opening created by the crack allowed the infiltration of electrolyte into the particle interior, accelerating the electrolyte attack of the exposed interior surfaces. The dark-field scanning TEM image in Figure 5.11b shows that individual primary particles in the cycled bare NRG65 cathode suffered from numerous intra-particle cracks. Hence, without the AlF_3 coating, the bare NRG65 cathode particles lost their mechanical integrity from the inter-granular fracture as well as from the structural undermining of the primary particles themselves. The bright-field TEM image in Figure 5.11c confirms the intra-particle fracture by revealing a network of numerous hairline microcracks nucleated within a primary particle as pointed out by yellow arrows. In addition to the observed hairline microcracks, the high-resolution TEM of the surface area of the primary particle in Figure 5.11d indicates that the phase transition to the rocksalt structure arising from the cation intermixing persisted well into the particle interior. The Fourier transform of region III which is approximately 100 nm away from the particle surface still contains strong diffraction peaks corresponding to the rocksalt structure on the background pattern of the layered structure. This contrasts sharply with the surface structure of the cycled AlF_3-NRG65 cathode in which the damaged rocksalt layer was confined to ~ 20 nm. The thick damaged surface layer and the observed loss of the mechanical integrity well explains the rapid capacity fade of the bare cathode and immensely large value for R_{ct} of the bare full-cell electrode. In this regard, the O3-type Ni-rich $NaNi_xCo_yMn_zO_2$ capacity fading mechanism is very much like that of the LIB layered $LiNi_xCo_yMn_zO_2$ in which the cathode structure breaks down from mechanical stress imposed by numerous phase transitions with the surface degrading from electrolyte side-

reactions followed by electrolyte penetration into the bulk and accelerated capacity fade.[16,67,122] However, SIB $NaNi_xCo_yMn_zO_2$ undergoes more phase transitions than LIB $LiNi_xCo_yMn_zO_2$ and the extent of damage is more severe than those of the LIB $LiNi_xCo_yMn_zO_2$ cathodes possibly due to the large ionic size of the Na.

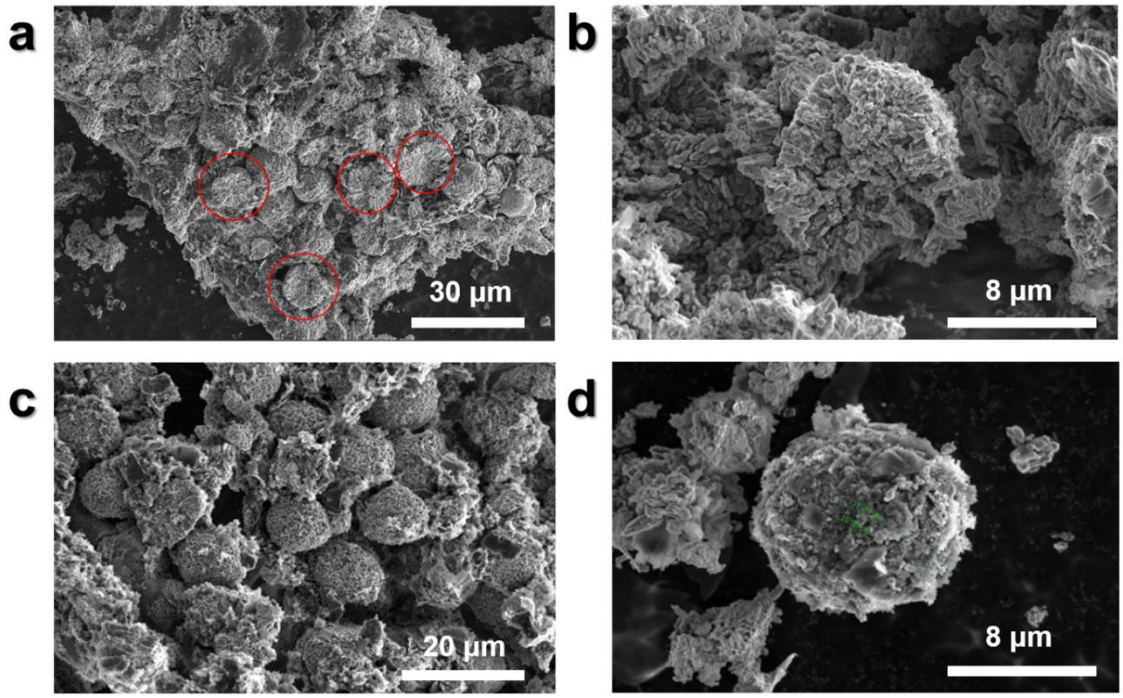

Figure 5.12. Post-mortem analysis: SEM images of the cycled (a, b) BARE NRG65 (red circles point out pulverized particles) and (c, d) AlF_3-NRG65 electrodes collected from the pouch-type full cells after 200 cycles.

Indeed, the SEM images of the post-mortem cycled full-cell electrodes reveal the efficacy of the AlF_3 coating at a macroscopic scale (Figure 5.12). The shattered particles are marked by red circles. Even though many of the after-cycled bare NRG65 particles remained intact due to the compact nanorods mechanically strengthening the structural integrity,[201,202] some of the particles still shattered (Figure 5.12a and b). As demonstrated *via* XRD patterns and TEM images above, electrolyte penetration *via* inter- and intra-

microcracks undermine bulk and surface structure and lead to cathode particle pulverization. Such pulverized active materials become disconnected from the wider electrical network and contribute to accelerated capacity fade. On the other hand, AlF_3-NRG65 particles displayed minimal damage to the overall particle morphology and remained intact as pointed out in Figure 5.12c and d due to the AlF_3 surface coating obstructing electrolyte penetration, which explains its stable electrochemical performance.

5.4. Summary

In summary, we propose an O3-type AlF_3 coated nano-rod gradient $Na[Ni_{0.65}Co_{0.08}Mn_{0.27}]O_2$ material as a high-performance cathode active component for SIBs. By combining the nano-rod gradient design with an AlF_3 coating, the O3-type AlF_3 coated nano-rod gradient $Na[Ni_{0.65}Co_{0.08}Mn_{0.27}]O_2$ cathode material delivers a high discharge capacity, (half-cell: 160 mAh g^{-1}, full-cell: 132 mAh g^{-1} at 0.1 C-rate), high capacity retention (half-cell: 89.2 %, full-cell 96.3 % at 0.5 C-rate), and promising rate capability. In addition, we explore the degradation mechanism of Ni-rich $Na[Ni_xCo_yMn_z]O_2$ cathode materials in SIBs. A systematic examination by electrochemical, structural, and optical methods of the post-mortem bare and AlF_3 coated nano-rod gradient $Na[Ni_{0.65}Co_{0.08}Mn_{0.27}]O_2$ cathodes clearly demonstrates that an AlF_3 nano-layer coating efficaciously shielded the particle bulk structure from electrolyte infiltration and limited structural degradation to a 4 – 5 nm thick region on the outer surface, preserving the interior layered structure, even at the particle periphery which is most vulnerable to Na removal. This leads to the preservation of overall particle cohesion

and promising electrochemical performance and we hope that this study will contribute to further development of Ni-rich O3-type $Na[Ni_xCo_yMn_z]O_2$.

Chapter 6. Summary

Structural and chemical design improved the performance of cells with Ni-rich cathodes and metallic lithium anodes. With the developed materials, a high energy density and stable prototype lithium metal battery, comprising a flower-petal grain cathode and an inorganic compound rich SEI stabilized metallic lithium anode was fabricated.

A multicomponent *in-situ* formed inorganic compound rich SEI layer stabilized the metallic lithium anode and suppressed dendrite growth. The mechanical robustness of the Li^+-permable SEI was also improved.

Concentration gradient Ni-rich cathodes, microstructure modified Ni-rich cathodes, single crystalline Ni-rich cathodes, and heterostructure Ni-rich cathodes address cathode degradation outperform coated and doped Ni-rich cathodes.

The best cathode is the nanorod concentration gradient cathode $Li[Ni_{0.81}CO_{0.06}Mn_{0.13}]O_2$ (NRG81). The NRG material has a high Ni core and consists of graded columnar nanorods that are arranged radially providing both high capacity and capacity retention. The nanorods in the particle exterior buffer the abrupt stress associated with the high-Ni core H2 – H3 phase transition, suppressing crack propagation and preserving particle integrity. Electrolyte infiltration into the reactive Ni-rich bulk is prevented and formation of the electrically insulating rock-salt nanostructure (NiO) along the cracks is avoided. This optimal cathode constitutes an engineering pre-prototype for a manufacturable and commercially implementable cathode of higher energy density.

Future works as a follow up on these studies could be focused on other cathode stabilization strategies discussed in Chapter 3 (microstructure modified cathodes, single

crystalline cathodes, and heterostructure cathodes) with a focus on 90 % or greater Ni content layered cathodes. Microstructure modified cathodes have a thin directionally-elongated grain morphology that is similar to gradient cathodes. Single crystalline cathodes are made of a single, large, grain and are resistant to crack formation. Heterostructure cathodes have two structurally different phases in the particle. These three strategies have not been extensively explored as the gradient cathodes and future works based on these cathodes will enlarge our understanding of lithium-ion battery cathodes. Furthermore, their coupling with the more traditional doping and surface modifications will improve the performance of lithium-ion batteries.

References

(1) Mizushima, K.; Jones, P. C.; Wiseman, P. J.; Goodenough, J. B. Li_xCoO_2 ($0 < x \leq$ l): A New Cathode Material for Batteries of High Energy Density. *Mat. Res. Bull* **1980**, *15*, 783–789.

(2) Whittingham, M. S.; Gamble, F. R. The Lithium Intercalates of the Transition Metal Dichalcogenides. *Mater. Res. Bull.* **1975**, *10*, 363–372.

(3) Yoshino, A. The Birth of the Lithium-Ion Battery. *Angew. Chemie - Int. Ed.* **2012**, *51*, 5798–5800.

(4) Tsiropoulos, I.; Tarvydas, D.; Lebedeva, N. *Li-Ion Batteries for Mobility and Stationary Storage Applications*, JRC Science for Policy Report, EU Commission, 2018.

(5) Avicenne Energy. *The Rechargeable Battery Market and Main Trends 2017 - 2025: 100 Pages Update*; 2018.

(6) Luntz, A. C.; Voss, J.; Reuter, K. Interfacial Challenges in Solid-State Li Ion Batteries. *J. Phys. Chem. Lett.* **2015**, *6*, 4599–4604.

(7) U.S. Department of Energy. *2015 Annual Progress Report for Energy Storage R&D*. **2016**, 11.

(8) MacNeil, D. D.; Hatchard, T. D.; Dahn, J. R. A Comparison Between the High Temperature Electrode/Electrolyte Reactions of Li_xCoO_2 and $Li_xMn_2O_4$. *J. Electrochem. Soc.* **2001**, *148*, A663.

(9) Amatucci, G.; Tarascon, J.-M. Optimization of Insertion Compounds Such as $LiMn_2O_4$ for Li-Ion Batteries. *J. Electrochem. Soc.* **2003**, *150*, L9.

(10) Zubi, G.; Dufo-López, R.; Carvalho, M.; Pasaoglu, G. The Lithium-Ion Battery: State of the Art and Future Perspectives. *Renew. Sustain. Energy Rev.* **2018**, *89*, 292–308.

(11) Nitta, N.; Wu, F.; Lee, J. T.; Yushin, G. Li-Ion Battery Materials: Present and Future. *Mater. Today* **2015**, *18*, 252–264.

(12) Gummow, R. J.; de Kock, A.; Thackeray, M. M. Improved Capacity Retention in Rechargeable 4 V Lithium/Lithium-Manganese Oxide (Spinel) Cells. *Solid State Ionics* **1994**, *69*, 59–67.

(13) Gummow, R.; Thackeray, M.; David, W.; Hull, S. Structure and Electrochemistry of Lithium Cobalt Oxide Synthesised at 400 ºC. *Mater. Res. Bull.* **1992**, *27*, 327–337.

(14) Myung, S. T.; Maglia, F.; Park, K. J.; Yoon, C. S.; Lamp, P.; Kim, S. J.; Sun, Y.-K. Nickel-Rich Layered Cathode Materials for Automotive Lithium-Ion Batteries: Achievements and Perspectives. *ACS Energy Lett.* **2017**, *2*, 196–223.

(15) Tang, W.; Kanoh, H.; Ooi, K. Preparation of Lithium Cobalt Oxide by LiCl-Flux Method for Lithium Rechargeable Batteries. *Electrochem. Solid-State Lett.* **1998**, *1*, 145–146.

(16) Yoon, C. S.; Jun, D.-W.; Myung, S.-T.; Sun, Y.-K. Structural Stability of $LiNiO_2$ Cycled above 4.2 V. *ACS Energy Lett.* **2017**, *2*, 1150–1155.

(17) Pillot, C. *The Rechargeable Battery Market and Main Trends 2016-2025*; 2018.

(18) Sun, Y.-K. High-Capacity Layered Cathodes for Next-Generation Electric Vehicles. *ACS Energy Lett.* **2019**, *4*, 1042–1044.

(19) Shi, H.; Barker, J.; Saïdi, M. Y.; Koksbang, R.; Morris, L. Graphite Structure and Lithium Intercalation. *J. Power Sources* **1997**, *68*, 291–295.

(20) Cheng, X. B.; Zhang, R.; Zhao, C. Z.; Wei, F.; Zhang, J. G.; Zhang, Q. A Review of Solid Electrolyte Interphases on Lithium Metal Anode. *Adv. Sci.* **2015**, *3*, 1–20.

(21) Kim, H.; Gong, Y. J.; Yoo, J.; Kim, Y. S. Highly Stable Lithium Metal Battery with an Applied Three-Dimensional Mesh Structure Interlayer. *J. Mater. Chem. A* **2018**, *6*, 15540–15545.

(22) Xu, W.; Wang, J.; Ding, F.; Chen, X.; Nasybulin, E.; Zhang, Y.; Zhang, J. G. Lithium Metal Anodes for Rechargeable Batteries. *Energy Environ. Sci.* **2014**, *7*, 513–537.

(23) Dahn, J.; Ehrlich, G. M. *Linden's Handbook of Batteries*, 4th ed.; Reddy, T. B., Linden, D., Eds.; McGraw Hill Professional, Access Engineering: New York, 2011.

(24) Ji, L.; Lin, Z.; Alcoutlabi, M.; Zhang, X. Recent Developments in Nanostructured Anode Materials for Rechargeable Lithium-Ion Batteries. *Energy Environ. Sci.* **2011**, *4*, 2682–2689.

(25) Miao, R.; Yang, J.; Xu, Z.; Wang, J.; Nuli, Y.; Sun, L. A New Ether-Based Electrolyte for Dendrite-Free Lithium-Metal Based Rechargeable Batteries. *Sci. Rep.* **2016**, *6*, 2–10.

(26) Sun, H.-H.; Dolocan, A.; Weeks, J. A.; Rodriguez, R.; Heller, A.; Mullins, C. B. In Situ Formation of a Multicomponent Inorganic-Rich SEI Layer Provides a Fast Charging and High Specific Energy Li-Metal Battery. *J. Mater. Chem. A* **2019**, *7*, 17782–17789.

(27) Sun, H. H.; Ryu, H.-H.; Kim, U.-H.; Weeks, J. A.; Heller, A.; Sun, Y.-K.; Mullins, C. B. Beyond Doping and Coating: Prospective Strategies for Stable High-Capacity Layered Ni-Rich Cathodes. *ACS Energy Lett.* **2020**, *5*, 1136–1146.

(28) Sun, H. H.; Weeks, J. A.; Heller, A.; Mullins, C. B. Nanorod Gradient Cathode: Preventing Electrolyte Penetration into Cathode Particles. *ACS Appl. Energy Mater.* **2019**, *2*, 6002–6011.

(29) Sun, H.-H.; Hwang, J. Y.; Yoon, C. S.; Heller, A.; Mullins, C. B. Capacity Degradation Mechanism and Cycling Stability Enhancement of AlF_3-Coated Nanorod Gradient $Na[Ni_{0.65}Co_{0.08}Mn_{0.27}]O_2$ Cathode for Sodium-Ion Batteries. *ACS Nano* **2018**, *12*, 12912–12922.

(30) Tarascon, J. M.; Armand, M. Issues and Challenges Facing Rechargeable Lithium Batteries. *Nature* **2001**, *414*, 359–367.

(31) Winter, M.; Barnett, B.; Xu, K. Before Li Ion Batteries. *Chem. Rev.* **2018**, *118*, 11433–11456.

(32) Palacín, M. R. Recent Advances in Rechargeable Battery Materials: A Chemist's Perspective. *Chem. Soc. Rev.* **2009**, *38*, 2565–2575.

(33) Goodenough, J. B.; Kim, Y. Challenges for Rechargeable Li Batteries. *Chem. Mater.* **2010**, *22*, 587–603.

(34) Tung, S. O.; Ho, S.; Yang, M.; Zhang, R.; Kotov, N. A. A Dendrite-Suppressing Composite Ion Conductor from Aramid Nanofibres. *Nat. Commun.* **2015**, *6*, 1–7.

(35) Yang, C. P.; Yin, Y. X.; Zhang, S. F.; Li, N. W.; Guo, Y. G. Accommodating Lithium into 3D Current Collectors with a Submicron Skeleton towards Long-Life Lithium Metal Anodes. *Nat. Commun.* **2015**, *6*, 8058.

(36) Cheng, X. B.; Zhang, Q. Dendrite-Free Lithium Metal Anodes: Stable Solid Electrolyte Interphases for High-Efficiency Batteries. *J. Mater. Chem. A* **2015**, *3*, 7207–7209.

(37) Zheng, J.; Engelhard, M. H.; Mei, D.; Jiao, S.; Polzin, B. J.; Zhang, J. G.; Xu, W. Electrolyte Additive Enabled Fast Charging and Stable Cycling Lithium Metal Batteries. *Nat. Energy* **2017**, *2*, 17012.

(38) Park, S. J.; Hwang, J. Y.; Yoon, C. S.; Jung, H. G.; Sun, Y.-K. Stabilization of Lithium-Metal Batteries Based on the in Situ Formation of a Stable Solid Electrolyte Interphase Layer. *ACS Appl. Mater. Interfaces* **2018**, *10*, 17985–17993.

(39) Yu, L.; Chen, S.; Lee, H.; Zhang, L.; Engelhard, M. H.; Li, Q.; Jiao, S.; Liu, J.; Xu, W.; Zhang, J. G. A Localized High-Concentration Electrolyte with Optimized Solvents and Lithium Difluoro(Oxalate)Borate Additive for Stable Lithium Metal Batteries. *ACS Energy Lett.* **2018**, *3*, 2059–2067.

(40) Suo, L.; Xue, W.; Gobet, M.; Greenbaum, S. G.; Wang, C.; Chen, Y.; Yang, W.; Li, Y.; Li, J. Fluorine-Donating Electrolytes Enable Highly Reversible 5-V-Class Li Metal Batteries. *Proc. Natl. Acad. Sci. U. S. A.* **2018**, *6*, 1156–1161.

(41) Park, K.; Goodenough, J. B. Dendrite-Suppressed Lithium Plating from a Liquid Electrolyte via Wetting of Li_3N. *Adv. Energy Mater.* **2017**, *7*, 1–7.

(42) Liu, Y.; Lin, D.; Yuen, P. Y.; Liu, K.; Xie, J.; Dauskardt, R. H.; Cui, Y. An Artificial Solid Electrolyte Interphase with High Li-Ion Conductivity, Mechanical Strength, and Flexibility for Stable Lithium Metal Anodes. *Adv. Mater.* **2017**, *29*, 1–8.

(43) Li, G.; Gao, Y.; He, X.; Huang, Q.; Chen, S.; Kim, S. H.; Wang, D. Organosulfide-Plasticized Solid-Electrolyte Interphase Layer Enables Stable Lithium Metal Anodes for Long-Cycle Lithium-Sulfur Batteries. *Nat. Commun.* **2017**, *8*, 850.

(44) Wan, G.; Guo, F.; Li, H.; Cao, Y.; Ai, X.; Qian, J.; Li, Y.; Yang, H. Suppression of Dendritic Lithium Growth by in Situ Formation of a Chemically Stable and Mechanically Strong Solid Electrolyte Interphase. *ACS Appl. Mater. Interfaces* **2018**, *10*, 593–601.

(45) Wang, X.; Zhang, M.; Alvarado, J.; Wang, S.; Sina, M.; Lu, B.; Bouwer, J.; Xu, W.; Xiao, J.; Zhang, J. G.; et al. New Insights on the Structure of Electrochemically Deposited Lithium Metal and Its Solid Electrolyte Interphases via Cryogenic TEM. *Nano Lett.* **2017**, *17*, 7606–7612.

(46) Shi, S.; Qi, Y.; Li, H.; Hector, L. G. Defect Thermodynamics and Diffusion Mechanisms in Li_2CO_3 and Implications for the Solid Electrolyte Interphase in Li-Ion Batteries. *J. Phys. Chem. C* **2013**, *117*, 8579–8593.

(47) Li, X.; Zheng, J.; Engelhard, M. H.; Mei, D.; Li, Q.; Jiao, S.; Liu, N.; Zhao, W.; Zhang, J. G.; Xu, W. Effects of Imide-Orthoborate Dual-Salt Mixtures in Organic Carbonate Electrolytes on the Stability of Lithium Metal Batteries. *ACS Appl. Mater. Interfaces* **2018**, *10*, 2469–2479.

(48) Xia, L.; Lee, S.; Jiang, Y.; Xia, Y.; Chen, G. Z.; Liu, Z. Fluorinated Electrolytes for Li-Ion Batteries: The Lithium Difluoro(Oxalato)Borate Additive for Stabilizing the Solid Electrolyte Interphase. *ACS Omega* **2017**, *2*, 8741–8750.

(49) Balkanski, M.; Wallis, R. F.; Deppe, J.; Massot, M. Dynamical Properties of Fast-Ion-Conducting Borate Glasses. *Mater. Sci. Eng. B* **1992**, *12*, 281–298.

(50) Schedlbauer, T.; Krüger, S.; Schmitz, R.; Schmitz, R. W.; Schreiner, C.; Gores, H. J.; Passerini, S.; Winter, M. Lithium Difluoro(Oxalato)Borate: A Promising Salt for Lithium Metal Based Secondary Batteries? *Electrochim. Acta* **2013**, *92*, 102–107.

(51) Sacci, R. L.; Black, J. M.; Balke, N.; Dudney, N. J.; More, K. L.; Unocic, R. R. Nanoscale Imaging of Fundamental Li Battery Chemistry: Solid-Electrolyte Interphase Formation and Preferential Growth of Lithium Metal Nanoclusters. *Nano Lett.* **2015**, *15*, 2011–2018.

(52) Peled, E.; Golodnitsky, D. *Lithium-Ion Batteries: Solid-Electrolyte Interphase*, Imperial College, London, 2004; p 1.

(53) Xu, C.; Xiang, W.; Wu, Z.; Xu, Y.; Li, Y.; Wang, Y.; Xiao, Y.; Guo, X.; Zhong, B. Highly Stabilized Ni-Rich Cathode Material with Mo Induced Epitaxially Grown

Nanostructured Hybrid Surface for High-Performance Lithium-Ion Batteries. *ACS Appl. Mater. Interfaces* **2019**, *11*, 16629–16638.

(54) Hwang, J. Y.; Park, S. J.; Yoon, C. S.; Sun, Y.-K. Customizing a Li-Metal Battery That Survives Practical Operating Conditions for Electric Vehicle Applications. *Energy Environ. Sci.* **2019**, *12*, 2174–2184.

(55) Steiger, J.; Richter, G.; Wenk, M.; Kramer, D.; Mönig, R. Comparison of the Growth of Lithium Filaments and Dendrites under Different Conditions. *Electrochem. commun.* **2015**, *50*, 11–14.

(56) Bai, P.; Li, J.; Brushett, F. R.; Bazant, M. Z. Transition of Lithium Growth Mechanisms in Liquid Electrolytes. *Energy Environ. Sci.* **2016**, *9*, 3221–3229.

(57) Appetecchi, G. B.; Croce, F.; Scrosati, B. High-Performance Electrolyte Membranes for Plastic Lithium Batteries. *J. Power Sources* **1997**, *66*, 77–82.

(58) Li, F.; Gong, Y.; Jia, G.; Wang, Q.; Peng, Z.; Fan, W.; Bai, B. A Novel Dual-Salts of LiTFSI and LiODFB in $LiFePO_4$-Based Batteries for Suppressing Aluminum Corrosion and Improving Cycling Stability. *J. Power Sources* **2015**, *295*, 47–54.

(59) Leys, J.; Rajesh, R. N.; Menon, P. C.; Glorieux, C.; Longuemart, S.; Nockemann, P.; Pellens, M.; Binnemans, K. Influence of the Anion on the Electrical Conductivity and Glass Formation of 1-Butyl-3-Methylimidazolium Ionic Liquids. *J. Chem. Phys.* **2010**, *133*, 1–10.

(60) Aravindan, V.; Gnanaraj, J.; Madhavi, S.; Liu, H. K. Lithium-Ion Conducting Electrolyte Salts for Lithium Batteries. *Chem. - A Eur. J.* **2011**, *17*, 14326–14346.

(61) Chou, H.; Ismach, A.; Ghosh, R.; Ruoff, R. S.; Dolocan, A. Erratum: Revealing the Planar Chemistry of Two-Dimensional Heterostructures at the Atomic Level. *Nat. Commun.* **2015**, *6*, 9229.

(62) Griffin, M. P.; Gearba, R.; Stevenson, K. J.; Vanden Bout, D. A.; Dolocan, A. Revealing the Chemistry and Morphology of Buried Donor/Acceptor Interfaces in Organic Photovoltaics. *J. Phys. Chem. Lett.* **2017**, *8*, 2764–2773.

(63) Huggins, R. A. Recent Results on Lithium Ion Conductors. *Electrochim. Acta* **1977**, *22*, 773–781.

(64) Park, S. H.; Park, K. S.; Sun Kook, Y.; Nahm, K. S.; Lee, Y. S.; Yoshio, M. Structural and Electrochemical Characterization of Lithium Excess and Al-Doped Nickel Oxides Synthesized by the Sol-Gel Method. *Electrochim. Acta* **2001**, *46*, 1215–1222.

(65) Yoon, C. S.; Park, K. J.; Kim, U. H.; Kang, K. H.; Ryu, H. H.; Sun, Y.-K. High-Energy Ni-Rich $Li[Ni_xCo_yMn_{1-x-y}]O_2$ Cathodes via Compositional Partitioning for Next-Generation Electric Vehicles. *Chem. Mater.* **2017**, *29*, 10436–10445.

(66) Nam, G. W.; Park, N.-Y.; Park, K.-J.; Yang, J.; Liu, J.; Yoon, C. S.; Sun, Y.-K. Capacity Fading of Ni-Rich NCA Cathodes: Effect of Microcracking Extent. *ACS Energy Lett.* **2019**, *4*, 2995–3001.

(67) Ryu, H. H.; Park, K. J.; Yoon, C. S.; Sun, Y.-K. Capacity Fading of Ni-Rich $Li[Ni_xCo_yMn_{1-x-y}]O_2$ ($0.6 \leq x \leq 0.95$) Cathodes for High-Energy-Density Lithium-Ion Batteries: Bulk or Surface Degradation? *Chem. Mater.* **2018**, *30*, 1155–1163.

(68) Noh, H. J.; Youn, S.; Yoon, C. S.; Sun, Y.-K. Comparison of the Structural and Electrochemical Properties of Layered $Li[Ni_xCo_yMn_z]O_2$ (x = 1/3, 0.5, 0.6, 0.7, 0.8 and 0.85) Cathode Material for Lithium-Ion Batteries. *J. Power Sources* **2013**, *233*, 121–130.

(69) Bianchini, M.; Roca-Ayats, M.; Hartmann, P.; Brezesinski, T.; Janek, J. There and Back Again—The Journey of $LiNiO_2$ as a Cathode Active Material. *Angew. Chemie - Int. Ed.* **2019**, *58*, 10434–10458.

(70) Watanabe, S.; Hosokawa, T.; Morigaki, K.; Kinoshita, M.; Nakura, K. Prevention of the Micro Cracks Generation in $LiNiCoAlO_2$ Cathode by the Restriction of DOD. *ECS Transanctions* **2012**, *41*, 65–74.

(71) Watanabe, S.; Kinoshita, M.; Hosokawa, T.; Morigaki, K.; Nakura, K. Capacity Fading of $LiAl_yNi_{1-x-y}Co_xO_2$ Cathode for Lithium-Ion Batteries during Accelerated Calendar and Cycle Life Tests (Effect of Depth of Discharge in Charge-Discharge Cycling on the Suppression of the Micro-Crack Generation of $LiAl_yNi_{1-x-y}Co_xO_2$ Particle. *J. Power Sources* **2014**, *260*, 50–56.

(72) Watanabe, S.; Kinoshita, M.; Hosokawa, T.; Morigaki, K.; Nakura, K. Capacity Fade of $LiAl_yNi_{1-x-y}Co_xO_2$ Cathode for Lithium-Ion Batteries during Accelerated Calendar and Cycle Life Tests (Surface Analysis of $LiAl_yNi_{1-x-y}Co_xO_2$ Cathode after Cycle Tests in Restricted Depth of Discharge Ranges). *J. Power Sources* **2014**, *258*, 210–217.

(73) Wu, L.; Nam, K.-W.; Wang, X.; Zhou, Y.; Zheng, J.-C.; Yang, X.-Q.; Zhu, Y. Structural Origin of Overcharge-Induced Thermal Instability of Ni-Containing Layered-Cathodes for High-Energy-Density Lithium Batteries. *Chem. Mater.* **2011**, *23*, 3953–3960.

(74) Nam, K.-W.; Bak, S.-M.; Hu, E.; Yu, X.; Zhou, Y.; Wang, X.; Wu, L.; Zhu, Y.; Chung, K.-Y.; Yang, X.-Q. Combining In Situ Synchrotron X-Ray Diffraction and Absorption Techniques with Transmission Electron Microscopy to Study the Origin of Thermal Instability in Overcharged Cathode Materials for Lithium-Ion Batteries. *Adv. Funct. Mater.* **2013**, *23*, 1047–1063.

(75) Martha, S. K.; Markevich, E.; Burgel, V.; Salitra, G.; Zinigrad, E.; Markovsky, B.; Sclar, H.; Pramovich, Z.; Heik, O.; Aurbach, D.; et al. A Short Review on Surface

Chemical Aspects of Li Batteries: A Key for a Good Performance. *J. Power Sources* **2009**, *189*, 288–296.

(76) Itou, Y.; Ukyo, Y. Performance of $LiNiCoO_2$ Materials for Advanced Lithium-Ion Batteries. *J. Power Sources* **2005**, *146*, 39–44.

(77) Kondrakov, A. O.; Schmidt, A.; Xu, J.; Geßwein, H.; Mönig, R.; Hartmann, P.; Sommer, H.; Brezesinski, T.; Janek, J. Anisotropic Lattice Strain and Mechanical Degradation of High- and Low-Nickel NCM Cathode Materials for Li-Ion Batteries. *J. Phys. Chem. C* **2017**, *121*, 3286–3294.

(78) Li, W.; Reimers, J. N.; Dahn, J. R. In Situ X-Ray Diffraction and Electrochemical Studies of $Li_{1-x}NiO_2$. *Solid State Ionics* **1993**, *67*, 123–130.

(79) Arai, H.; Okada, S.; Ohtsuka, H.; Ichimura, M.; Yamaki, J. Characterization and Cathode Performance of $Li_{1-x}Ni_{1+x}O_2$ Prepared with the Excess Lithium Method. *Solid State Ionics* **1995**, *80*, 261–269.

(80) Delmas, C.; Croguennec, L. Layered Li(Ni, M) O Systems as the Cathode Material in Lithium-Ion Batteries. **2002**, *August*, 608–612.

(81) Park, K. J.; Hwang, J. Y.; Ryu, H. H.; Maglia, F.; Kim, S. J.; Lamp, P.; Yoon, C. S.; Sun, Y.-K. Degradation Mechanism of Ni-Enriched NCA Cathode for Lithium Batteries: Are Microcracks Really Critical? *ACS Energy Lett.* **2019**, *4*, 1394–1400.

(82) Ryu, H. H.; Park, G. T.; Yoon, C. S.; Sun, Y.-K. Microstructural Degradation of Ni-Rich $Li[Ni_xCo_yMn_{1-x-y}]O_2$ Cathodes During Accelerated Calendar Aging. *Small* **2018**, *14*, 1–8.

(83) Pender, J. P.; Jha, G.; Youn, D. H.; Ziegler, J. M.; Andoni, I.; Choi, E. J.; Heller, A.; Dunn, B. S.; Weiss, P. S.; Penner, R. M. Electrode Degradation in Metal-Ion Batteries. *ACS Nano* **2020**, *14*, 1243.

(84) Chen, M.; Zhao, E.; Chen, D.; Wu, M.; Han, S.; Huang, Q.; Yang, L.; Xiao, X.; Hu, Z. Decreasing Li/Ni Disorder and Improving the Electrochemical Performances of Ni-Rich $LiNi_{0.8}Co_{0.1}Mn_{0.1}O_2$ by Ca Doping. *Inorg. Chem.* **2017**, *56*, 8355–8362.

(85) Woo, S. W.; Myung, S. T.; Bang, H.; Kim, D. W.; Sun, Y.-K. Improvement of Electrochemical and Thermal Properties of $Li[Ni_{0.8}Co_{0.1}Mn_{0.1}]O_2$ Positive Electrode Materials by Multiple Metal (Al, Mg) Substitution. *Electrochim. Acta* **2009**, *54*, 3851–3856.

(86) Kim, U.-H.; Myung, S.-T.; Yoon, C. S.; Sun, Y.-K. Extending the Battery Life Using an Al-Doped $Li[Ni_{0.76}Co_{0.09}Mn_{0.15}]O_2$ Cathode with Concentration Gradients for Lithium Ion Batteries. *ACS Energy Lett.* **2017**, *2*, 1848–1854.

(87) Kim, U. H.; Kuo, L. Y.; Kaghazchi, P.; Yoon, C. S.; Sun, Y.-K. Quaternary Layered Ni-Rich NCMA Cathode for Lithium-Ion Batteries. *ACS Energy Lett.* **2019**, *4*, 576–582.

(88) Li, Y. C.; Xiang, W.; Wu, Z. G.; Xu, C. L.; Xu, Y. Di; Xiao, Y.; Yang, Z. G.; Wu, C. J.; Lv, G. P.; Guo, X. D. Construction of Homogeneously Al^{3+} Doped Ni Rich Ni-Co-Mn Cathode with High Stable Cycling Performance and Storage Stability via Scalable Continuous Precipitation. *Electrochim. Acta* **2018**, *291*, 84–94.

(89) Liu, D.; Liu, S.; Zhang, C.; You, L.; Huang, T.; Yu, A. Revealing the Effect of Ti Doping on Significantly Enhancing Cyclic Performance at a High Cutoff Voltage for Ni-Rich $LiNi_{0.8}Co_{0.15}Al_{0.05}O_2$ Cathode. *ACS Sustain. Chem. Eng.* **2019**, *7*, 10661–10669.

(90) Sun, H.; Cao, Z.; Wang, T.; Lin, R.; Li, Y.; Liu, X.; Zhang, L.; Lin, F.; Huang, Y.; Luo, W. Enabling High Rate Performance of Ni-Rich Layered Oxide Cathode by Uniform Titanium Doping. *Mater. Today Energy* **2019**, *13*, 145–151.

(91) Yoon, C. S.; Kim, U. H.; Park, G. T.; Kim, S. J.; Kim, K. H.; Kim, J.; Sun, Y.-K. Self-Passivation of a $LiNiO_2$ Cathode for a Lithium-Ion Battery through Zr Doping. *ACS Energy Lett.* **2018**, *3*, 1634–1639.

(92) Susai, F. A.; Kovacheva, D.; Chakraborty, A.; Kravchuk, T.; Ravikumar, R.; Talianker, M.; Grinblat, J.; Burstein, L.; Kauffmann, Y.; Major, D. T.; et al. Improving Performance of $LiNi_{0.8}Co_{0.1}Mn_{0.1}O_2$ Cathode Materials for Lithium-Ion Batteries by Doping with Molybdenum-Ions: Theoretical and Experimental Studies. *ACS Appl. Energy Mater.* **2019**, *2*, 4521–4534.

(93) Ryu, H. H.; Park, G. T.; Yoon, C. S.; Sun, Y.-K. Suppressing Detrimental Phase Transitions via Tungsten Doping of $LiNiO_2$ Cathode for Next-Generation Lithium-Ion Batteries. *J. Mater. Chem. A* **2019**, *7*, 18580–18588.

(94) Xin, F.; Zhou, H.; Chen, X.; Zuba, M.; Chernova, N.; Zhou, G.; Whittingham, M. S. Li-Nb-O Coating/Substitution Enhances the Electrochemical Performance of the $LiNi_{0.8}Mn_{0.1}Co_{0.1}O_2$ (NMC 811) Cathode. *ACS Appl. Mater. Interfaces* **2019**, *11*, 34889–34894.

(95) Huang, Y.; Liu, X.; Yu, R.; Cao, S.; Pei, Y.; Luo, Z.; Zhao, Q.; Chang, B.; Wang, Y.; Wang, X. Tellurium Surface Doping to Enhance the Structural Stability and Electrochemical Performance of Layered Ni-Rich Cathodes. *ACS Appl. Mater. Interfaces* **2019**, *11*, 40022–40033.

(96) Binder, J. O.; Culver, S. P.; Pinedo, R.; Weber, D. A.; Friedrich, M. S.; Gries, K. I.; Volz, K.; Zeier, W. G.; Janek, J. Investigation of Fluorine and Nitrogen as Anionic Dopants in Nickel-Rich Cathode Materials for Lithium-Ion Batteries. *ACS Appl. Mater. Interfaces* **2018**, *10*, 44452–44462.

(97) Chen, Y.; Zhang, Y.; Chen, B.; Wang, Z.; Lu, C. An Approach to Application for $LiNi_{0.6}Co_{0.2}Mn_{0.2}O_2$ Cathode Material at High Cutoff Voltage by TiO_2 Coating. *J. Power Sources* **2014**, *256*, 20–27.

(98) Neudeck, S.; Strauss, F.; Garcia, G.; Wolf, H.; Janek, J.; Hartmann, P.; Brezesinski, T. Room Temperature, Liquid-Phase Al_2O_3 Surface Coating Approach for Ni-Rich Layered Oxide Cathode Material. *Chem. Commun.* **2019**, *55*, 2174–2177.

(99) Cho, W.; Kim, S. M.; Song, J. H.; Yim, T.; Woo, S. G.; Lee, K. W.; Kim, J. S.; Kim, Y. J. Improved Electrochemical and Thermal Properties of Nickel Rich $LiNi_{0.6}Co_{0.2}Mn_{0.2}O_2$ Cathode Materials by SiO_2 Coating. *J. Power Sources* **2015**, *282*, 45–50.

(100) Lee, S. H.; Yoon, C. S.; Amine, K.; Sun, Y.-K. Improvement of Long-Term Cycling Performance of $Li[Ni_{0.8}Co_{0.15}Al_{0.05}]O_2$ by AlF_3 Coating. *J. Power Sources* **2013**, *234*, 201–207.

(101) Xie, J.; Sendek, A. D.; Cubuk, E. D.; Zhang, X.; Lu, Z.; Gong, Y.; Wu, T.; Shi, F.; Liu, W.; Reed, E. J.; et al. Atomic Layer Deposition of Stable $LiAlF_4$ Lithium Ion Conductive Interfacial Layer for Stable Cathode Cycling. *ACS Nano* **2017**, *11*, 7019–7027.

(102) Woo, S.-U.; Yoon, C. S.; Amine, K.; Belharouak, I.; Sun, Y.-K. Significant Improvement of Electrochemical Performance of AlF_3-Coated $Li[Ni_{0.8}Co_{0.1}Mn_{0.1}]O_2$ Cathode Materials. *J. Electrochem. Soc.* **2007**, *154*, A1005.

(103) Xie, J.; Sendek, A. D.; Cubuk, E. D.; Zhang, X.; Lu, Z.; Gong, Y.; Wu, T.; Shi, F.; Liu, W.; Reed, E. J.; et al. Atomic Layer Deposition of Stable $LiAlF_4$ Lithium Ion Conductive Interfacial Layer for Stable Cathode Cycling. *ACS Nano* **2017**, *11*, 7019–7027.

(104) Lee, S. W.; Kim, M. S.; Jeong, J. H.; Kim, D. H.; Chung, K. Y.; Roh, K. C.; Kim, K. B. Li_3PO_4 Surface Coating on Ni-Rich $LiNi_{0.6}Co_{0.2}Mn_{0.2}O_2$ by a Citric Acid Assisted Sol-Gel Method: Improved Thermal Stability and High-Voltage Performance. *J. Power Sources* **2017**, *360*, 206–214.

(105) Son, I. H.; Park, J. H.; Park, S.; Park, K.; Han, S.; Shin, J.; Doo, S. G.; Hwang, Y.; Chang, H.; Choi, J. W. Graphene Balls for Lithium Rechargeable Batteries with Fast Charging and High Volumetric Energy Densities. *Nat. Commun.* **2017**, *8*, 1–10.

(106) Huang, Y.; Jin, F. M.; Chen, F. J.; Chen, L. Improved Cycle Stability and High-Rate Capability of Li_3VO_4-Coated $Li[Ni_{0.5}Co_{0.2}Mn_{0.3}]O_2$ Cathode Material under Different Voltages. *J. Power Sources* **2014**, *256*, 1–7.

(107) Hu, W.; Zhang, C.; Jiang, H.; Zheng, M.; Wu, Q. H.; Dong, Q. Improving the Electrochemistry Performance of Layer $LiNi_{0.5}Co_{0.2}Mn_{0.3}O_2$ Material at 4.5 V Cutoff Potential Using Lithium Metaborate. *Electrochim. Acta* **2017**, *243*, 105–111.

(108) Wang, J.; Yu, Y.; Li, B.; Fu, T.; Xie, D.; Cai, J.; Zhao, J. Improving the Electrochemical Properties of $LiNi_{0.5}Co_{0.2}Mn_{0.3}O_2$ at 4.6 v Cutoff Potential by Surface Coating with Li_2TiO_3 for Lithium-Ion Batteries. *Phys. Chem. Chem. Phys.* **2015**, *17*, 32033–32043.

(109) Ju, S. H.; Kang, I. S.; Lee, Y. S.; Shin, W. K.; Kim, S.; Shin, K.; Kim, D. W. Improvement of the Cycling Performance of $LiNi_{0.6}Co_{0.2}Mn_{0.2}O_2$ Cathode Active Materials by a Dual-Conductive Polymer Coating. *ACS Appl. Mater. Interfaces* **2014**, *6*, 2546–2552.

(110) Cao, Y.; Qi, X.; Hu, K.; Wang, Y.; Gan, Z.; Li, Y.; Hu, G.; Peng, Z.; Du, K. Conductive Polymers Encapsulation to Enhance Electrochemical Performance of Ni-Rich Cathode Materials for Li-Ion Batteries. *ACS Appl. Mater. Interfaces* **2018**, *10*, 18270–18280.

(111) Chen, S.; He, T.; Su, Y.; Lu, Y.; Bao, L.; Chen, L.; Zhang, Q.; Wang, J.; Chen, R.; Wu, F. Ni-Rich L $LiNi_{0.8}Co_{0.1}Mn_{0.1}O_2$ Oxide Coated by Dual-Conductive Layers as High Performance Cathode Material for Lithium-Ion Batteries. *ACS Appl. Mater. Interfaces* **2017**, *9*, 29732–29743.

(112) Liu, K.; Zhang, Q.; Dai, S.; Li, W.; Liu, X.; Ding, F.; Zhang, J. Synergistic Effect of F- Doping and LiF Coating on Improving the High-Voltage Cycling Stability and Rate Capacity of L $LiNi_{0.5}Co_{0.2}Mn_{0.3}O_2$ Cathode Materials for Lithium-Ion Batteries. *ACS Appl. Mater. Interfaces* **2018**, *10*, 34153–34162.

(113) Chen, Z.; Qin, Y.; Amine, K.; Sun, Y.-K. Role of Surface Coating on Cathode Materials for Lithium-Ion Batteries. *J. Mater. Chem.* **2010**, *20*, 7606–7612.

(114) Myung, S. T.; Amine, K.; Sun, Y.-K. Surface Modification of Cathode Materials from Nano-to Microscale for Rechargeable Lithium-Ion Batteries. *J. Mater. Chem.* **2010**, *20*, 7074–7095.

(115) Kim, U. H.; Ryu, H. H.; Kim, J. H.; Mücke, R.; Kaghazchi, P.; Yoon, C. S.; Sun, Y.-K. Microstructure-Controlled Ni-Rich Cathode Material by Microscale Compositional Partition for Next-Generation Electric Vehicles. *Adv. Energy Mater.* **2019**, *9*, 1–11.

(116) Sun, Y.-K.; Myung, S. T.; Park, B. C.; Prakash, J.; Belharouak, I.; Amine, K. High-Energy Cathode Material for Long-Life and Safe Lithium Batteries. *Nat. Mater.* **2009**, *8*, 320–324.

(117) Sun, Y.-K.; Kim, D. H.; Yoon, C. S.; Myung, S. T.; Prakash, J.; Amine, K. A Novel Cathode Material with a Concentration Gradient for High-Energy and Safe Lithium-Ion Batteries. *Adv. Funct. Mater.* **2010**, *20*, 485–491.

(118) Jun, D. W.; Yoon, C. S.; Kim, U. H.; Sun, Y.-K. High-Energy Density Core-Shell Structured $Li[Ni_{0.95}Co_{0.025}Mn_{0.025}]O_2$ Cathode for Lithium-Ion Batteries. *Chem. Mater.* **2017**, *29*, 5048–5052.

(119) Sun, Y.-K.; Chen, Z.; Noh, H. J.; Lee, D. J.; Jung, H. G.; Ren, Y.; Wang, S.; Yoon, C. S.; Myung, S. T.; Amine, K. Nanostructured High-Energy Cathode Materials for Advanced Lithium Batteries. *Nat. Mater.* **2012**, *11*, 942–947.

(120) Noh, H. J.; Myung, S. T.; Jung, H. G.; Yashiro, H.; Amine, K.; Sun, Y.-K. Formation of a Continuous Solid-Solution Particle and Its Application to Rechargeable Lithium Batteries. *Adv. Funct. Mater.* **2013**, *23*, 1028–1036.

(121) Ju, J. W.; Lee, E. J.; Yoon, C. S.; Myung, S. T.; Sun, Y.-K. Optimization of Layered Cathode Material with Full Concentration Gradient for Lithium-Ion Batteries. *J. Phys. Chem. C* **2014**, *118*, 175–182.

(122) Kim, U. H.; Lee, E. J.; Yoon, C. S.; Myung, S. T.; Sun, Y.-K. Compositionally Graded Cathode Material with Long-Term Cycling Stability for Electric Vehicles Application. *Adv. Energy Mater.* **2016**, *6*, 1–8.

(123) Xu, X.; Xiang, L.; Wang, L.; Jian, J.; Du, C.; He, X.; Huo, H.; Cheng, X.; Yin, G. Progressive Concentration Gradient Nickel-Rich Oxide Cathode Material for High-Energy and Long-Life Lithium-Ion Batteries. *J. Mater. Chem. A* **2019**, *7*, 7728–7735.

(124) Hou, P.; Zhang, H.; Zi, Z.; Zhang, L.; Xu, X. Core-Shell and Concentration-Gradient Cathodes Prepared via Co-Precipitation Reaction for Advanced Lithium-Ion Batteries. *J. Mater. Chem. A* **2017**, *5*, 4254–4279.

(125) Lee, E. J.; Chen, Z.; Noh, H. J.; Nam, S. C.; Kang, S.; Kim, D. H.; Amine, K.; Sun, Y.-K. Development of Microstrain in Aged Lithium Transition Metal Oxides. *Nano Lett.* **2014**, *14*, 4873–4880.

(126) Lim, B. B.; Yoon, S. J.; Park, K. J.; Yoon, C. S.; Kim, S. J.; Lee, J. J.; Sun, Y.-K. Advanced Concentration Gradient Cathode Material with Two-Slope for High-Energy and Safe Lithium Batteries. *Adv. Funct. Mater.* **2015**, *25*, 4673–4680.

(127) Park, K. J.; Lim, B. B.; Choi, M. H.; Jung, H. G.; Sun, Y.-K.; Haro, M.; Vicente, N.; Bisquert, J.; Garcia-Belmonte, G. A High-Capacity $Li[Ni_{0.8}Co_{0.06}Mn_{0.14}]O_2$ Positive Electrode with a Dual Concentration Gradient for next-Generation Lithium-Ion Batteries. *J. Mater. Chem. A* **2015**, *3*, 22183–22190.

(128) Lim, B. B.; Myung, S. T.; Yoon, C. S.; Sun, Y.-K. Comparative Study of Ni-Rich Layered Cathodes for Rechargeable Lithium Batteries: $Li[Ni_{0.85}Co_{0.11}Al_{0.04}]O_2$ and $Li[Ni_{0.84}Co_{0.06}Mn_{0.09}Al_{0.01}]O2$ with Two-Step Full Concentration Gradients. *ACS Energy Lett.* **2016**, *1*, 283–289.

(129) Lee, J. H.; Yoon, C. S.; Hwang, J.-Y.; Kim, S.-J.; Maglia, F.; Lamp, P.; Myung, S.-T.; Sun, Y.-K. High-Energy-Density Lithium-Ion Battery Using a Carbon-Nanotube–Si Composite Anode and a Compositionally Graded $Li[Ni_{0.85}Co_{0.05}Mn_{0.10}]O_2$ Cathode. *Energy Environ. Sci.* **2016**, *9*, 2152–2158.

(130) Kim, U. H.; Kim, J. H.; Hwang, J. Y.; Ryu, H. H.; Yoon, C. S.; Sun, Y.-K. Compositionally and Structurally Redesigned High-Energy Ni-Rich Layered Cathode for next-Generation Lithium Batteries. *Mater. Today* **2019**, *23*, 26–36.

(131) Yoon, C. S.; Kim, S. J.; Kim, U. H.; Park, K. J.; Ryu, H. H.; Kim, H. S.; Sun, Y.-K. Microstructure Evolution of Concentration Gradient $Li[Ni_{0.75}Co_{0.10}Mn_{0.15}]O_2$ Cathode for Lithium-Ion Batteries. *Adv. Funct. Mater.* **2018**, *28*, 1–7.

(132) Park, K.-J.; Jung, H.-G.; Kuo, L.-Y.; Kaghazchi, P.; Yoon, C. S.; Sun, Y.-K. Improved Cycling Stability of $Li[Ni_{0.90}Co_{0.05}Mn_{0.05}]O_2$ Through Microstructure Modification by Boron Doping for Li-Ion Batteries. *Adv. Energy Mater.* **2018**, *8*, 1801202.

(133) Yang, X.; Tang, Y.; Shang, G.; Wu, J.; Lai, Y.; Li, J.; Qu, Y.; Zhang, Z. Enhanced Cyclability and High-Rate Capability of $LiNi_{0.88}Co_{0.095}Mn_{0.025}O_2$ Cathodes by Homogeneous Al^{3+} Doping. *ACS Appl. Mater. Interfaces* **2019**, *11*, 32015–32024.

(134) Ryu, H. H.; Park, K. J.; Yoon, D. R.; Aishova, A.; Yoon, C. S.; Sun, Y.-K. $Li[Ni_{0.9}Co_{0.09}W_{0.01}]O_2$: A New Type of Layered Oxide Cathode with High Cycling Stability. *Adv. Energy Mater.* **2019**, *9*, 1902698.

(135) Kim, H.; Lee, E. J.; Sun, Y.-K. Recent Advances in the Si-Based Nanocomposite Materials as High Capacity Anode Materials for Lithium Ion Batteries. *Mater. Today* **2014**, *17*, 285–297.

(136) Weber, R.; Fell, C. R.; Dahn, J. R.; Hy, S. Operando X-Ray Diffraction Study of Polycrystalline and Single-Crystal $Li_xNi_{0.5}Mn_{0.3}Co_{0.2}O_2$. *J. Electrochem. Soc.* **2017**, *164*, A2992–A2999.

(137) Li, H.; Li, J.; Zaker, N.; Zhang, N.; Botton, G. A.; Dahn, J. R. Synthesis of Single Crystal $LiNi_{0.88}Co_{0.09}Al_{0.03}O_2$ with a Two-Step Lithiation Method. *J. Electrochem. Soc.* **2019**, *166*, A1956–A1963.

(138) Cho, Y.; Lee, S.; Lee, Y.; Hong, T.; Cho, J. Spinel-Layered Core-Shell Cathode Materials for Li-Ion Batteries. *Adv. Energy Mater.* **2011**, *1*, 821–828.

(139) Kim, U. H.; Jun, D. W.; Park, K. J.; Zhang, Q.; Kaghazchi, P.; Aurbach, D.; Major, D. T.; Goobes, G.; Dixit, M.; Leifer, N.; et al. Pushing the Limit of Layered Transition Metal Oxide Cathodes for High-Energy Density Rechargeable Li Ion Batteries. *Energy Environ. Sci.* **2018**, *11*, 1271–1279.

(140) Park, G. T.; Ryu, H. H.; Park, N. Y.; Yoon, C. S.; Sun, Y.-K. Tungsten Doping for Stabilization of $Li[Ni_{0.90}Co_{0.05}Mn_{0.05}]O_2$ Cathode for Li-Ion Battery at High Voltage. *J. Power Sources* **2019**, *442*, 227242.

(141) Yoon, C. S.; Choi, M. J.; Jun, D. W.; Zhang, Q.; Kaghazchi, P.; Kim, K. H.; Sun, Y.-K. Cation Ordering of Zr-Doped $LiNiO_2$ Cathode for Lithium-Ion Batteries. *Chem. Mater.* **2018**, *30*, 1808–1814.

(142) Yang, S. F.; Zavalij, P. Y.; Whittingham, M. S. Hydrothermal Synthesis of Lithium Iron Phosphate Cathodes. *Electrochem. commun.* **2001**, *3*, 505–508.

(143) Kim, J. H.; Myung, S. T.; Yoon, C. S.; Kang, S. G.; Sun, Y.-K. Comparative Study of $LiNi_{0.5}Mn_{1.5}O_4$ and $LiNi_{0.5}Mn_{1.5}O_4$ Cathodes Having Two Crystallographic Structures: Fd3m and P4332. *Chem. Mater.* **2004**, *16*, 906–914.

(144) Lin, J.; Lim, J. M.; Youn, D. H.; Kawashima, K.; Kim, J. H.; Liu, Y.; Guo, H.; Henkelman, G.; Heller, A.; Mullins, C. B. Self-Assembled Cu-Sn-S Nanotubes with High (De)Lithiation Performance. *ACS Nano* **2017**, *11*, 10347–10356.

(145) Abel, P. R.; Chockla, A. M.; Lin, Y. M.; Holmberg, V. C.; Harris, J. T.; Korgel, B. A.; Heller, A.; Mullins, C. B. Nanostructured $Si_{(1-x)}Ge_x$ for Tunable Thin Film Lithium-Ion Battery Anodes. *ACS Nano* **2013**, *7*, 2249–2257.

(146) Youn, D. H.; Stauffer, S. K.; Xiao, P.; Park, H.; Nam, Y.; Dolocan, A.; Henkelman, G.; Heller, A.; Mullins, C. B. Simple Synthesis of Nanocrystalline Tin Sulfide/N-Doped Reduced Graphene Oxide Composites as Lithium Ion Battery Anodes. *ACS Nano* **2016**, *10*, 10778–10788.

(147) Lee, M. H.; Kang, Y. J.; Myung, S. T.; Sun, Y.-K. Synthetic Optimization of $Li[Ni_{1/3}Co_{1/3}Mn_{1/3}]O_2$ via Co-Precipitation. *Electrochim. Acta* **2004**, *50*, 939–948.

(148) Sun, H.-H.; Choi, W.; Lee, J. K.; Oh, I. H.; Jung, H. G. Control of Electrochemical Properties of Nickel-Rich Layered Cathode Materials for Lithium Ion Batteries by Variation of the Manganese to Cobalt Ratio. *J. Power Sources* **2015**, *275*, 877–883.

(149) Liu, H.; Wolf, M.; Karki, K.; Yu, Y. S.; Stach, E. A.; Cabana, J.; Chapman, K. W.; Chupas, P. J. Intergranular Cracking as a Major Cause of Long-Term Capacity Fading of Layered Cathodes. *Nano Lett.* **2017**, *17*, 3452–3457.

(150) Zheng, S.; Huang, R.; Makimura, Y.; Ukyo, Y.; Fisher, C. A. J.; Hirayama, T.; Ikuhara, Y. Microstructural Changes in $LiNi_{0.8}Co_{0.15}Al_{0.05}O_2$ Positive Electrode Material during the First Cycle. *J. Electrochem. Soc.* **2011**, *158*, A357.

(151) Ohzuku, T. Electrochemistry and Structural Chemistry of $LiNiO_2$ (R3m) for 4 Volt Secondary Lithium Cells. *J. Electrochem. Soc.* **1993**, *140*, 1862.

(152) Miller, D. J.; Proff, C.; Wen, J. G.; Abraham, D. P.; Bareño, J. Observation of Microstructural Evolution in Li Battery Cathode Oxide Particles by in Situ Electron Microscopy. *Adv. Energy Mater.* **2013**, *3*, 1098–1103.

(153) Reimers, J. N.; Rossen, E.; Jones, C. D.; Dahn, J. R. Structure and Electrochemistry of $Li_xFe_yNi_{1-y}O_2$. *Solid State Ionics* **1993**, *61*, 335–344.

(154) Pouillerie, C.; Croguennec, L.; Delmas, C. $Li_xNi_{1-y}Mg_yO_2$ (y = 0.05, 0.10) System: Structural Modifications Observed upon Cycling. *Solid State Ionics* **2000**, *132*, 15–29.

(155) Subramanian, V.; Fey, G. T. K. Preparation and Characterization of $LiNi_{0.7}Co_{0.2}Ti_{0.05}M_{0.05}O_2$ (M=Mg, Al and Zn) Systems as Cathode Materials for Lithium Batteries. *Solid State Ionics* **2002**, *148*, 351–358.

(156) Wilcox, J.; Patoux, S.; Doeff, M. Structure and Electrochemistry of LiNi[Sub 1⁄3]Co[Sub 1⁄3−y]M[Sub y]Mn[Sub 1⁄3]O[Sub 2] (M=Ti, Al, Fe) Positive Electrode Materials. *J. Electrochem. Soc.* **2009**, *156* (3), A192.

(157) Chen, Z.; Dahn, J. R. Reducing Carbon in $LiFePO_4$/C Composite Electrodes to Maximize Specific Energy, Volumetric Energy, and Tap Density. *J. Electrochem. Soc.* **2002**, *149*, A1184.

(158) Myung, S. T.; Izumi, K.; Komaba, S.; Sun, Y.-K.; Yashiro, H.; Kumagai, N. Role of Alumina Coating on Li-Ni-Co-Mn-O Particles as Positive Electrode Material for Lithium-Ion Batteries. *Chem. Mater.* **2005**, *17*, 3695–3704.

(159) Jang, S. B.; Kang, S. H.; Amine, K.; Bae, Y. C.; Sun, Y.-K. Synthesis and Improved Electrochemical Performance of Al $(OH)_3$-Coated $Li[Ni_{1/3}Mn_{1/3}Co_{1/3}]O_2$ Cathode Materials at Elevated Temperature. *Electrochim. Acta* **2005**, *50*, 4168–4173.

(160) Sun, Y.-K.; Han, J. M.; Myung, S. T.; Lee, S. W.; Amine, K. Significant Improvement of High Voltage Cycling Behavior AlF_3-Coated $LiCoO_2$cathode. *Electrochem. commun.* **2006**, *8*, 821–826.

(161) Takamatsu, D.; Mori, S.; Orikasa, Y.; Nakatsutsumi, T.; Koyama, Y.; Tanida, H.; Arai, H.; Uchimoto, Y.; Ogumi, Z. Effects of ZrO_2 Coating on $LiCoO_2$ Thin-Film Electrode Studied by In Situ X-Ray Absorption Spectroscopy. *J. Electrochem. Soc.* **2013**, *160*, A3054–A3060.

(162) EcoPro http://www.ecopro.co.kr/eng (accessed Nov 11, 2018).

(163) Sun, Y.-K.; Myung, S.-T.; Kim, M.-H.; Prakash, J.; Amine, K. Synthesis and Characterization of $Li[(Ni_{0.8}Co_{0.1}Mn_{0.1})_{0.8}(Ni_{0.5}Mn_{0.5})_{0.2}]O_2$ with the Microscale Core−Shell Structure as the Positive Electrode Material . *J. Am. Chem. Soc.* **2005**, *127*, 13411–13418.

(164) Ryu, H. H.; Park, K. J.; Yoon, C. S.; Sun, Y.-K. Capacity Fading of Ni-Rich $Li[Ni_xCo_yMn_{1-x-y}]O_2$ ($0.6 \leq x \leq 0.95$) Cathodes for High-Energy-Density Lithium-Ion Batteries: Bulk or Surface Degradation? *Chem. Mater.* **2018**, *30*, 1155–1163.

(165) Bak, S.; Hu, E.; Zhou, Y.; Yu, X.; Senanayake, S. D.; Cho, S.; Kim, K.; Chung, K. Y.; Yang, X.; Nam, K. Structural Changes and Thermal Stability of Charged LiNi. *Appl. Mater. Interfaces* **2014**, *6*, 22594–22601.

(166) Scrosati, B.; Hassoun, J.; Sun, Y.-K. Lithium-Ion Batteries. A Look into the Future. *Energy Environ. Sci.* **2011**, *4*, 3287.

(167) Etacheri, V.; Marom, R.; Elazari, R.; Salitra, G.; Aurbach, D. Challenges in the Development of Advanced Li-Ion Batteries: A Review. *Energy Environ. Sci.* **2011**, *4*, 3243–3262.

(168) Palacín, M. R.; De Guibert, A. Batteries: Why Do Batteries Fail? *Science (80-.).* **2016**, *351*, 1253292.

(169) Forster, J.; Rutherford, T. F. A Lithium Shortage: Are Electric Vehicles Under Threat? **2011**, No. May.
(170) Perkel, J. M. The Trouble with Lithium Implications of Future PHEV Production for Lithium Demand. *Nature* **2015**, *521*, 111–112.
(171) Slater, M. D.; Kim, D.; Lee, E.; Johnson, C. S. Sodium-Ion Batteries. *Adv. Funct. Mater.* **2013**, *23*, 947–958.
(172) Hwang, J.-Y.; Myung, S.-T.; Sun, Y.-K. Sodium-Ion Batteries: Present and Future. *Chem. Soc. Rev.* **2017**, *46*, 3529–3614.
(173) Oh, S. M.; Myung, S. T.; Hassoun, J.; Scrosati, B.; Sun, Y.-K. Reversible $NaFePO_4$ Electrode for Sodium Secondary Batteries. *Electrochem. Commun.* **2012**, *22*, 149–152.
(174) Chihara, K.; Kitajou, A.; Gocheva, I. D.; Okada, S.; Yamaki, J. I. Cathode Properties of $Na_3M_2(PO_4)_2F_3$ [M = Ti, Fe, V] for Sodium-Ion Batteries. *J. Power Sources* **2013**, *227*, 80–85.
(175) Ratnakumar, B. V.; Di Stefano, S.; Williams, R. M.; Nagasubramanian, G.; Bankston, C. P. Organic Cathode Materials in Sodium Batteries. *J. Appl. Electrochem.* **1990**, *20*, 357–364.
(176) Yabuuchi, N.; Kajiyama, M.; Iwatate, J.; Nishikawa, H.; Hitomi, S.; Okuyama, R.; Usui, R.; Yamada, Y.; Komaba, S. P2-Type $Na_x[Fe_{1/2}Mn_{1/2}]O_2$ made from Earth-Abundant Elements for Rechargeable NaÂ Batteries. *Nat. Mater.* **2012**, *11*, 512–517.
(177) Berthelot, R.; Carlier, D.; Delmas, C. Electrochemical Investigation of the P2–Na_xCoO_2 Phase Diagram. *Nat. Mater.* **2011**, *10*, 74–80.
(178) Buchholz, D.; Chagas, L. G.; Winter, M.; Passerini, S. P2-Type Layered $Na_{0.45}Ni_{0.22}Co_{0.11}Mn_{0.66}O_2$ as Intercalation Host Material for Lithium and Sodium Batteries. *Electrochim. Acta* **2013**, *110*, 208–213.
(179) D'Arienzo, M.; Ruffo, R.; Scotti, R.; Morazzoni, F.; Mari, C. M.; Polizzi, S. Layered $Na_{0.71}CoO_2$: A Powerful Candidate for Viable and High Performance Na-Batteries. *Phys. Chem. Chem. Phys.* **2012**, *14*, 5945–5952.
(180) Yu, T.-Y.; Hwang, J.-Y.; Aurbach, D.; Sun, Y.-K. Microsphere $Na_{0.65}[Ni_{0.17}Co_{0.11}Mn_{0.72}]O_2$ Cathode Material for High-Performance Sodium-Ion Batteries. *ACS Appl. Mater. Interfaces* **2017**, *2*, 44534–44541.
(181) Yabuuchi, N.; Yano, M.; Yoshida, H.; Kuze, S.; Komaba, S. Synthesis and Electrode Performance of O3-Type $NaFeO_2$-$NaNi_{1/2}Mn_{1/2}O_2$ Solid Solution for Rechargeable Sodium Batteries. *J. Electrochem. Soc.* **2013**, *160*, A3131–A3137.
(182) Xia, X.; Dahn, J. R. $NaCrO_2$ Is a Fundamentally Safe Positive Electrode Material for Sodium-Ion Batteries with Liquid Electrolytes. *Electrochem. Solid-State Lett.* **2012**, *15*, A1 - A4.

(183) Oh, S. M.; Myung, S. T.; Jang, M. W.; Scrosati, B.; Hassoun, J.; Sun, Y.-K. An Advanced Sodium-Ion Rechargeable Battery Based on a Tin-Carbon Anode and a Layered Oxide Framework Cathode. *Phys. Chem. Chem. Phys.* **2013**, *15*, 3827–3833.

(184) Oh, S.-M.; Myung, S.-T.; Yoon, C. S.; Lu, J.; Hassoun, J.; Scrosati, B.; Amine, K.; Sun, Y.-K. Advanced $Na[Ni_{0.25}Fe_{0.5}Mn_{0.25}]O_2$/C–$Fe_3O_4$ Sodium-Ion Batteries Using EMS Electrolyte for Energy Storage. *Nano Lett.* **2014**, *14*, 1620–1626.

(185) Hwang, J.-Y.; Yoon, C. S.; Belharouak, I.; Sun, Y.-K. A Comprehensive Study of the Role of Transition Metals in O3-Type Layered $Na[Ni_xCo_yMn_z]O_2$ (x = 1/3, 0.5, 0.6, and 0.8) Cathodes for Sodium-Ion Batteries. *J. Mater. Chem. A* **2016**, *4*, 17952–17959.

(186) Guo, S.; Yu, H.; Liu, P.; Ren, Y.; Zhang, T.; Chen, M.; Ishida, M.; Zhou, H. High-Performance Symmetric Sodium-Ion Batteries Using a New, Bipolar O3-Type Material, $Na_{0.8}Ni_{0.4}Ti_{0.6}O_2$. *Energy Environ. Sci.* **2015**, *8*, 1237–1244.

(187) Komaba, S.; Yabuuchi, N.; Nakayama, T.; Ogata, A.; Ishikawa, T.; Nakai, I. Study on the Reversible Electrode Reaction of $Na_{1-x}Ni_{0.5}Mn_{0.5}O_2$ for a Rechargeable Sodium-Ion Battery. *Inorg. Chem.* **2012**, *51*, 6211–6220.

(188) Bo, S. H.; Li, X.; Toumar, A. J.; Ceder, G. Layered-to-Rock-Salt Transformation in Desodiated Na_xCrO_2 (x = 0.4). *Chem. Mater.* **2016**, *28*, 1419–1429.

(189) Yabuuchi, N.; Kubota, K.; Dahbi, M.; Komaba, S. Research Development on Sodium-Ion Batteries. *Chem. Rev.* **2014**, *114*, 11636–11682.

(190) Yabuuchi, N.; Kawamoto, Y.; Hara, R.; Ishigaki, T.; Hoshikawa, A.; Yonemura, M.; Kamiyama, T.; Komaba, S. A Comparative Study of $LiCoO_2$ Polymorphs: Structural and Electrochemical Characterization of O2-, O3-, and O4-Type Phases. *Inorg. Chem.* **2013**, *52*, 9131–9142.

(191) Liu, L.; Wang, Z.; Li, H.; Chen, L.; Huang, X. Al_2O_3-Coated $LiCoO_2$ as Cathode Material for Lithium Ion Batteries. *Solid State Ionics* **2002**, *152–153*, 341–346.

(192) Appapillai, A. T.; Mansour, A. N.; Cho, J.; Shao-Horn, Y. Microstructure of $LiCoO_2$ with and without "$AlPO_4$" Nanoparticle Coating: Combined STEM and XPS Studies. *Chem. Mater.* **2007**, *19*, 5748–5757.

(193) Sun, Y.-K.; Yoon, C. S.; Myung, S.-T.; Belharouak, I.; Amine, K. Role of AlF_3 Coating on LiCoO2 Particles during Cycling to Cutoff Voltage above 4.5 V. *J. Electrochem. Soc.* **2009**, *156*, A1005.

(194) Jo, J. H.; Choi, J. U.; Konarov, A.; Yashiro, H.; Yuan, S.; Shi, L.; Sun, Y.-K.; Myung, S. T. Sodium-Ion Batteries: Building Effective Layered Cathode Materials with Long-Term Cycling by Modifying the Surface via Sodium Phosphate. *Adv. Funct. Mater.* **2018**, *28*, 1–11.

(195) Yang, S. J.; Kang, J. H.; Jung, H.; Kim, T.; Park, C. R. Simultaneous MgO Coating and Mg Doping of $Na[Ni_{0.5}Mn_{0.5}]O_2$ Cathode: Facile and Customizable Approach to High-Voltage Sodium-Ion Batteries. *J. Mater. Chem. A* **2013**, *1*, 9427–9432.

(196) Ramasamy, H. V.; Kaliyappan, K.; Thangavel, R.; Aravindan, V.; Kang, K.; Kim, D. U.; Park, Y.; Sun, X.; Lee, Y. S. Cu-Doped P2-$Na_{0.5}Ni_{0.33}Mn_{0.67}O_2$ Encapsulated with MgO as a Novel High Voltage Cathode with Enhanced Na-Storage Properties. *J. Mater. Chem. A* **2017**, *5*, 8408–8415.

(197) Kaliyappan, K.; Liu, J.; Xiao, B.; Lushington, A.; Li, R.; Sham, T.-K.; Sun, X. Enhanced Performance of P2-$Na_{0.66}(Mn_{0.54}Co_{0.13}Ni_{0.13})O_2$ Cathode for Sodium-Ion Batteries by Ultrathin Metal Oxide Coatings via Atomic Layer Deposition. *Adv. Funct. Mater.* **2017**, *27*, 1701870.

(198) Kaliyappan, K.; Liu, J.; Lushington, A.; Li, R.; Sun, X. Highly Stable $Na_{2/3}(Mn_{0.54}Ni_{0.13}Co_{0.13})O_2$ Cathode Modified by Atomic Layer Deposition for Sodium-Ion Batteries. *ChemSusChem* **2015**, *8*, 2537–2543.

(199) Liu, Y.; Fang, X.; Zhang, A.; Shen, C.; Liu, Q.; Enaya, H. A.; Zhou, C. Layered P2-$Na_{2/3}[Ni_{1/3}Mn_{2/3}]O_2$ as High-Voltage Cathode for Sodium-Ion Batteries: The Capacity Decay Mechanism and Al_2O_3 surface Modification. *Nano Energy* **2016**, *27*, 27–34.

(200) Hwang, J. Y.; Myung, S. T.; Choi, J. U.; Yoon, C. S.; Yashiro, H.; Sun, Y.-K. Resolving the Degradation Pathways of the O3-Type Layered Oxide Cathode Surface through the Nano-Scale Aluminum Oxide Coating for High-Energy Density Sodium-Ion Batteries. *J. Mater. Chem. A* **2017**, *5*, 23671–23680.

(201) Hwang, J. Y.; Myung, S. T.; Yoon, C. S.; Kim, S. S.; Aurbach, D.; Sun, Y.-K. Novel Cathode Materials for Na-Ion Batteries Composed of Spoke-Like Nanorods of $Na[Ni_{0.61}Co_{0.12}Mn_{0.27}]O_2$ Assembled in Spherical Secondary Particles. *Adv. Funct. Mater.* **2016**, *26*, 8083–8093.

(202) Hwang, J. Y.; Oh, S. M.; Myung, S. T.; Chung, K. Y.; Belharouak, I.; Sun, Y.-K. Radially Aligned Hierarchical Columnar Structure as a Cathode Material for High Energy Density Sodium-Ion Batteries. *Nat. Commun.* **2015**, *6*, 1–9.

(203) Sun, Y.-K.; Lee, M. J.; Yoon, C. S.; Hassoun, J.; Amine, K.; Scrosati, B. The Role of AlF_3 Coatings in Improving Electrochemical Cycling of Li-Enriched Nickel-Manganese Oxide Electrodes for Li-Ion Batteries. *Adv. Mater.* **2012**, *24*, 1192–1196.

(204) Zheng, J.; Gu, M.; Xiao, J.; Polzin, B. J.; Yan, P.; Chen, X.; Wang, C.; Zhang, J. G. Functioning Mechanism of AlF_3 Coating on the Li- and Mn-Rich Cathode Materials. *Chem. Mater.* **2014**, *26*, 6320–6327.

(205) Rodríguez-Carvajal, J. FULLPROF: A Program for Rietveld Refinement and Pattern Matching Analysis. *Abstr. Satell. Meet. Powder Diffr. XV Congr. IUCr*, **1990**, 127.
(206) Delmas, C.; Fouassier, C.; Hagenmuller, P. Structural Classification and Properties of the Layered Oxides. *Phys. B+C* **1980**, *99* (1–4), 81–85.
(207) Delmas, C.; Saadoune, I. Electrochemical and Physical Properties of the $Li_xNi_{1-y}Co_yO_2$ Phases. *Solid State Ionics* **1992**, *53–56*, 370–375.
(208) Vijayakumar, R.; Shivaramu; Rajasekaran, L.; Ramamurthy, N.; Ford, M. J. Compton Profile of Polycrystalline Sodium Chloride and Sodium Fluoride. *Nucl. Instruments Methods Phys. Res. Sect. B Beam Interact. with Mater. Atoms* **2005**, *234*, 185–193.
(209) Jacoboni, C.; Leble, A.; Rousseau, J. J. De´termination Pre´cise de La Structure de La Chiolite $Na_5Al_3F_{14}$ Ete´tude Par R.P.E. de $Na_5Al_3F_{14}:Cr^{3+}$. *J. Solid State Chem.* **1981**, *36*, 297–304.
(210) Kozen, A. C.; Pearse, A. J.; Lin, C.-F.; Noked, M.; Rubloff, G. W. Atomic Layer Deposition of the Solid Electrolyte LiPON. *Chem. Mater.* **2015**, *27*, 5324–5331.
(211) Cao, H.; Xia, B.; Zhang, Y.; Xu, N. $LiAlO_2$-Coated $LiCoO_2$ as Cathode Material for Lithium Ion Batteries. *Solid State Ionics* **2005**, *176*, 911–914.

Vita

Ho Hyun Sun was born in Seoul, Republic of Korea. He obtained his B.S. in Chemical Engineering from Northwestern University in 2015. He then joined the University of Texas at Austin in 2015. He joined the Mullins group in 2017 to pursue his Ph.D. degree in Chemical engineering. His Ph.D. research focused on the development of stable highly Ni-rich cathodes and metallic lithium anodes for viable high energy density Li-ion batteries.

Email address: hhsun448@gmail.com

This dissertation was typed by the author.